IMPERIAL COLLEGE LONDON

Estimating the reliability of guided wave SHM systems through modelling

by

Panpan Xu

A thesis submitted to Imperial College London for the degree of
Doctor of Philosophy

Department of Mechanical Engineering
Imperial College London
London SW7 2AZ

May 2025

Declaration of originality

The content of this thesis is my own research work, which was completed with the supervision of Dr Peter Huthwaite, Professor Michael Lowe, Dr Robin Jones, and Dr Georgios Sarris. Wherever other work was used I clearly acknowledged, and provided references.

Panpan Xu

05/05/2025

Copyright

“All models are wrong, but some are useful.”

— George Box

Abstract

Guided wave structural health monitoring (SHM) presents a promising, cost-effective, and efficient modality for evaluating pipeline integrity. To support its widespread industrial adoption, quantitative reliability estimation in realistic environments is essential. This thesis develops a framework for estimating the reliability of guided wave SHM systems through realistic finite element (FE) modelling, with a strong focus on practical applications.

Accurate model-based reliability estimation requires high-fidelity simulation of real-world conditions, including instrumentation installation, initial pipe conditions, and environmental influences. A methodology is first presented for analysing key features of real guided wave signals, particularly random and coherent noise, based on laboratory data. The formation and composition of coherent noise are studied in detail, with attention to transducer performance imbalance.

A numerical framework is proposed to generate realistic guided wave signals that incorporate both coherent and random noise. This is validated through simulation and experiments, effectively capturing noise characteristics at both individual and statistical levels. The framework also supports the simulation of defect signals, enabling more accurate Probability of Detection (POD) analysis. Additionally, by modelling transducer imbalance, it facilitates noise reduction in experimental signals and improves the signal-to-noise ratio (SNR).

A digital twin-based reliability estimation framework is then proposed to provide timely, system-specific reliability assessments over the SHM system's lifecycle. It constructs a digital twin based on in-situ measurements and estimates key simulation parameters affected by environmental temperature and structural conditions. Compared to traditional model-assisted reliability methods in Non-Destructive Evaluation (NDE), this approach offers a more accurate and dynamic performance assessment, supporting better-informed maintenance and inspection decisions.

Lastly, the influence of geometric imperfections on guided wave signals is investigated. The effects of pipe wall thickness variations on wave behaviour are quantified through high-fidelity modelling, enhancing the integration of initial pipe conditions into digital twins and improving reliability estimation.

Acknowledgements

I would like to express my deepest gratitude to my supervisor, Dr Peter Huthwaite, for his constant mentorship, encouragement, and invaluable insights throughout my PhD study, fostering not only my knowledge but also my growth as an independent researcher. My appreciation extends to my co-supervisors, Prof Michael Lowe, Dr Robin Jones, and Dr Georgios Sarris, for their invaluable guidance and support in my research work. This work would not have been possible without their patience and dedication.

Furthermore, I would like to thank Dr Frederic Cegla and Dr Bo Lan for their commitment to creating an inspiring and collaborative research environment in the Non-Destructive Evaluation group. Special thanks go to Prof Peter Cawley for his valuable feedback on my paper and Mr Antonio De Sanctis for his assistance with my experiments. Sincere gratitude is due to Nina Hancock for her administrative support.

I am truly grateful for all the scientific and technical support received from Guided Ultrasonics Ltd. I especially want to acknowledge Dr Thomas Vogt and Dr Stefano Mariani for sharing their profound knowledge and engaging in insightful discussions on guided waves. Thanks also go to other colleagues at GUL for warmly welcoming me as part of the team.

My heartfelt appreciation goes to all my colleagues in the NDE group, past and present, for their help, companionship, and invaluable friendship at Imperial. In particular, I would like to mention Dr Ming Huang, Dr Yifeng Zhang, Dr Jaime Parra Raad, Dr Filip Szlaszynski, Dr Pouyan Khalili, Aaron Chung-Jukko, Jennifer Jobling, Wei Yi Yeoh, Melody Png, André Lello, Evripides Georgiades, Connor Challinor, Laurence Clarkson, Liam Corette, Yuankai Ren, Yifei Yang, Antonio Brozicevic, Elias Rabbat, Alexandru Nichita, and Paddy Caskey.

I would also like to acknowledge the sponsorship from the Horizon 2020 Marie Skłodowska-Curie Actions Innovative Training Network and all support received from the GW4SHM project, for introducing me to the SHM community with dedicated researchers and organising various training events and secondments.

Finally, I would like to express my profound gratitude to my parents, my father Jinwei Xu and my mother Sanni Liang, for their unconditional love and endless encouragement throughout the years.

Contents

List of Figures

List of Tables

Nomenclature

S'_{T01}	T(0,1) signal contaminated by noise
$*$	Complex conjugate
α	Auxiliary variable, $\alpha^2 = \frac{\omega^2}{C_l^2} - k^2$
α_1	Auxiliary variable, $\alpha_1 = \lvert\alpha\rvert$
β	Stretch factor
β_0	Intercept of the linear regression in POD analysis
β_1	Slope of the linear regression in POD analysis
$\cdot$	Multiplication in the frequency domain
Δc	Wave velocity change
Δx	Uniform mesh sizes in axial direction
Δy	Uniform mesh sizes in circumferential direction
$\Delta\theta$	Phase shift
η	Mean value
γ_1	Skewness
γ_2	Kurtosis

$\hat{\beta}_0$	Estimate of β_0
$\hat{\beta}_1$	Estimate of β_1
$\hat{\tau}$	Estimate of τ
$\hat{a}$	Signal response in POD analysis
$\hat{a}_0$	Detection Threshold in POD analysis
$\hat{a}_i$	Corresponding signal response with a flaw size of a_i
ι	Time transformation factor
λ_x	Correlation length in the pipe axial direction
λ_y	Correlation length in the pipe circumferential direction
$\mathbf{H}$	Equivoluminal vector in Helmholtz decomposition
$\mathbf{k}$	Wavenumber
$\mathbf{R}$	Position vector
$\mathbf{r}$	Position of one measurement point
$\mathbf{u}$	Displacement field
μ, λ	Lamé constants
Ω	Transformed angular frequency
ω	Angular frequency
ϕ	Compressional scalar potential in Helmholtz decomposition
Φ_{norm}	Cumulative density function of a standard normal distribution
ψ	The wave motion through the thickness of the pipe wall
ρ	Density

σ	Standard deviation
σ_v	Standard deviation of the uncorrelated 2D random thickness variation map
$\sigma_{\beta_0 \tau}$	Covariance between β_0 and τ
$\sigma_{\beta_1 \tau}$	Covariance between β_1 and τ
σ_n	RMS of the random noise
σ_{rr}, $\sigma_{r\theta}$, σ_{rz}	Stress components
σ_s	RMS of the signal
τ	Standard deviation of the Random component ε_i
$\mathbf{C}$, $\mathbf{C}_{8\times 8}$	Coefficient matrix in solving axial flexural wave modes
$\mathbf{D}$	Coefficient matrix in solving circumferential SH waves
$\mathrm{AMP}_{\mathrm{T(0,1)}}$	The amplitude of the T(0,1) wavepacket reflected from the pipe end
$\mathrm{RMS}_{\mathrm{CoherentNoise}}$	The RMS value of coherent noise
θ	Circumferential direction in the cylindrical coordinate
υ	Diffusion coefficient in the degradation model
ε_i	Random component of the linear regression in POD analysis
ϱ	Drift coefficient in the degradation model
ς	Auxiliary variable, $\varsigma^2 = \frac{\omega^2}{C_s^2} - k^2$
ς_1	Auxiliary variable, $\varsigma_1 = \lvert\varsigma\rvert$
ϑ	Stabilisation factor in deconvolution using Wiener filter

ξ	Standard deviation
$\Xi_1(r)$	Field varies in radial coordinate
$\Xi_2(\theta)$	Field varies in circumferential coordinate
$\Xi_3(z)$	Field varies in axial coordinate
a_{50}	The flaw size where the POD is 50%
$a_{90/95}$	The flaw size at which the system has 90% POD with 95% confidence
a_i	Flaw size in POD analysis
A_q $(q = 1, 2, 3, 4)$, B_q $(q = 1, 2, 3, 4)$	Coefficients of Bessel functions
$B(t^{\iota})$	Standard Brownian motion
b	An integer to compensate for phase ambiguity in phase wrapping
C	Correlation function
c	Wave velocity
c_0	Phase wave velocity at the baseline temperature
c_1	Phase wave velocity at the current temperature
C_{ij}	Elements of $\mathbf{C}$
c_l	Longitudinal wave velocity
c_p	Linear phase velocity of a circumferential wave mode
c_s	Shear wave velocity
$D(t)$	Degradation level of a transducer
d	Wave propagation distance
$E[\cdot]$	Expectation operator

e	Euler's number
$F(\Omega)$	Correction factor in temperature compensation
f	Coefficient in ϕ
$f^{'}$	First order derivative of f
$f^{''}$	Second order derivative of f
f_c	Central frequency of the excitation signal
f_{low}	Lower frequency band of a bandpass filter
f_{upper}	Upper frequency band of a bandpass filter
h	Thickness variation function
h_1	Auxiliary variable, $2h_1 = ih_r - h_\theta$
$h_1^{'}$	First order derivative of h_1
$h_1^{''}$	Second order derivative of h_1
h_2	Auxiliary variable, $2h_2 = ih_r + h_\theta$
$h_2^{'}$	First order derivative of h_2
$h_2^{''}$	Second order derivative of h_2
h_3	Auxiliary variable, $h_3 = h_z$
$h_3^{'}$	First order derivative of h_3
$h_3^{''}$	Second order derivative of h_3
h_θ	Coefficient in H_θ
h_r	Coefficient in H_r
h_z	Coefficient in H_z

I	Extents of the kernel in axial (x) direction
J	Extents of the kernel in circumferential (y) direction
J_n, Y_n	nth order Bessel functions
J_p, Y_p	pth order Bessel functions
K	A shift factor in in the degradation model
k	Wavenumber component in the axial direction
k_l	Wavenumber of longitudinal bulk waves
k_s	Wavenumber of shear bulk waves
M	Number of the signals for averaging
m	Counter number of axial wave modes
N	The number of elements in a transducer ring
n	Circumferential order of axial wave modes
P	Probability
p	Angular wavenumber
p_{norm}	Probability density function of a normal distribution
pdf	Probability density function
Q	Coefficient in stabilisation factor ϑ
r	Radial direction in the cylindrical coordinate
R^2	Coefficient of determination in linear regression
r_1	Inner radius
r_2	Outer radius

$S'_{1,1}$	Experimental pulse-echo signal from transducer No. 1
$S'_{1,35}$	Experimental signal emitted from transducer No. 1 and received by transducer No. 35
S'_1	Signal from transducer No. 1 contaminated by noise captured with CSM arrangement
$S'_{\mathrm{N}ij}$	Random noise signal in the signal S'_{ij}
$S'_{\mathrm{N}j}$	Random noise signal in the signal S'_j
S'_{ij}	Signal S_{ij} contaminated by noise
S'_i	Signal from transducer i contaminated by noise captured with CSM arrangement
S'_{jj}	Experimental pulse-echo signal from transducer j
S'_j	Signal from transducer j contaminated by noise captured with CSM arrangement
S^c_{ij}	Compensated signal emitted from transducer i and received by transducer j
$S_0(\omega)$	Excitation signal in the frequency domain
S_{T01}	Ideal T(0,1) signal
S_{ij}	Ideal signal emitted from transducer i and received by transducer j
S_j	Ideal signal from transducer j captured with CSM arrangement
t	Time
T^R_{Rj}	Relative transfer function of transducer j acting as a receiver
T^R_{Tj}	Relative transfer function of transducer j acting as a transmitter

T_{Rj}	Transfer function of transducer j acting as a receiver
T_{Ti}	Transfer function of transducer i acting as a transmitter
$U_1^c(\Omega)$	Current signal with temperature compensation
$U_1^s(\Omega)$	Current signal with stretch factor applied
$U_0(\omega)$	Baseline signal in the frequency domain
$U_1(\omega)$	Current signal in the frequency domain
u_{baseline}	Current signal in the time domain
u_{current}	Current signal in the time domain
u_{defect}	Defect signal in the time domain
u_θ	Circumferential component of the displacement field
u_r	Radial component of the displacement field
u_z	Axial component of the displacement field
v	2D random thickness variation map
w_{ij}	Moving window
X	Data point in statistical analysis
x	Pipe axial direction mapped in Cartesian coordinates
y	Pipe circumferential direction mapped in Cartesian coordinates
z	Axial direction in the cylindrical coordinate
H_θ	Circumferential component of the equivoluminal vector in Helmholtz decomposition

H_r	Radial component of the equivoluminal vector in Helmholtz decomposition
H_z	Axial component of the equivoluminal vector in Helmholtz decomposition
F(n,m)	Axial flexural modes
L(0,m)	Axial longitudinal modes
T(0,m)	Axial torsional modes

List of Acronym

SHM Structural Health Monitoring

POD Probability of Detection

PFA Probability of False Alarm

NDE Non-Destructive Evaluation

MAPOD Model-Assisted Probability of Detection

FE Finite Element

GAN Generative Adversarial Network

ODEs Ordinary Differential Equations

GUL Guided Ultrasonics Ltd.

SH Shear Horizontal

RMS Root Mean Square

SNR Signal-to-Noise Ratio

PDF Probability Density Function

PSD Power Spectral Density

CSM Common Source Method

FMC Full Matrix Capture

ToF Time of Flight

EOCs Environmental and Operational Conditions

SVD Singular Value Decomposition

ICA Independent Component Analysis

NP-TS Non-Parametric Time Series

PCA Principal Component Analysis

VAE Variational Autoencoder

GAN Generative Adversarial Network

OLS Ordinary Least-Squares

DAC Distance Amplitude Correction

ASTM American Society for Testing and Materials

CSC Cross-Sectional Change

SE Standard Error

API American Petroleum Institute

CNC Computer Numerical Control

BSS Baseline Signal Stretch

LSTC Location Specific Temperature Compensation

LaD Length at Detection

MSE Mean Square Error

RF Radio Frequency

gPIMS	Permanently Installed Guided Wave Monitoring
ROC	Receiver Operating Characteristic
EMAT	Electromagnetic Acoustic Transducer

List of Publications

[P1] P. Xu, R. Jones, and P. Huthwaite. Efficient Generation of Realistic Guided Wave Signals for Reliability Estimation. *Structural Health Monitoring*, 2025. https://doi.org/10.1177/14759217241302469

[P2] P. Xu, G. Sarris, R. Jones, and P. Huthwaite. A Digital Twin-Based Reliability Estimation Framework for Guided Wave Pipe Monitoring with Temperature Variations. *Mechanical Systems and Signal Processing*, accepted, 2025. Available at: http://dx.doi.org/10.2139/ssrn.5114350

[P3] Rasgado-Moreno, C.O., Xu, P., Rist, M. and Ratassepp, M., 2025. Optimising full waveform inversion with inhomogeneous transducers: Parameters and considerations for successful implementation. *NDT & E International*, 149, 103265. https://doi.org/10.1016/j.ndteint.2024.103265

Chapter 1

Introduction

1.1 Motivation

Ultrasonic inspection has broad impact in industry as it is a safe and reliable modality for subsurface inspection. It is estimated that ultrasonic inspection accounts for approximately 28% of the global Non-Destructive Evaluation (NDE) market in 2024 [1], with a market size projected to reach USD 1.6 billion by 2029 [2], driven by demand in industries such as aerospace, oil and gas, automotive, and power generation. In the oil and gas sector, ultrasonic techniques are extensively used both in manufacturing and in-service pipeline inspections, particularly for detecting surface and subsurface defects such as corrosion, cracks, and wall thinning [3–5]. In the aerospace industry, ultrasonic inspection is also widely employed to assess the integrity of composite structures, including fuselages and wing-boxes [6–8]. Advanced ultrasonic techniques such as phased arrays and guided waves are increasingly integrated into structural integrity management strategies and inspection protocols to support safe and cost-effective maintenance operations.

Within ultrasonic inspection, ultrasonic guided wave testing is a highly appealing NDE method, particularly for inspecting large structures, owing to its ability to inspect significant portions of a structure from a single transducer location. This is particularly true within the oil and gas industry where its application for the inspection of pipelines has been well established [9–14]. Recent advancements in permanently installed transducers have made it increasingly attractive to transition from periodic NDE inspections to automated Structural Health Monitoring (SHM), which promises enhanced reliability and a reduction in the operational costs typically associated with regular inspections [15–18]. In addition, fully automating the monitoring can significantly reduce the operational risks for personnel and operators.

Despite the progress made in advancing guided wave Structural Health Monitoring (SHM) from laboratory experimentation to practical industrial applications [19], the assessment of reliability remains a critical step before its widespread deployment in industry [20–22]. Therefore, this thesis aims to develop a framework for the reliability estimation of guided wave SHM systems, with a focus on practical applications in pipeline monitoring.

Conventional reliability estimation methods, such as Probability of Detection (POD) analysis [23], rely on a statistically significant number of experimental trials, which involve manufacturing representative samples with various flaw sizes and measuring them under realistic conditions. The challenge lies in the expense and time intensity of experimental approaches to establish reliability estimates. In response to this challenge, the concept of Model-Assisted Probability of Detection (MAPOD) was introduced [24, 25], aiming to substitute empirical experiments with physics-based theoretical or numerical models for reliability estimation, thereby effectively reducing the cost and time associated with sample fabrication and experimentation. Since its introduction, the MAPOD method has garnered considerable attention and has been extensively explored in the realms of NDE [26, 27] and

SHM [28, 29].

One of the key factors influencing the accuracy of model-assisted reliability estimation lies in the fidelity of the model-generated data, which refers to how closely the simulated signals replicate real experimental measurements. High-fidelity data is essential, since it has the potential of capturing the complexities of guided wave signals observed in laboratory or field conditions. While various modelling tools offer cost-efficiency in generating data with varying configurations compared to experimental campaigns, most current models primarily simulate the fundamental physics of wave propagation under idealised conditions, and fail to account for the actual measurement environment and its associated uncertainties.

In this thesis, the Finite Element (FE) method is employed to address the challenge of accurately producing data as close as possible to those real guided wave signals, since it fully captures all critical aspects of wave physics and is able to be configured for arbitrarily complex geometries. Advances in computational software mean that the extensive time needed for such simulations has been reduced significantly [30]. The challenges in generating realistic signals that resemble real measurements involve several practical aspects, particularly in the context of guided wave pipe monitoring.

In practical scenarios, real measurements are invariably affected by a range of uncertainties, such as system noise and instrumentation-related errors [31]. These factors contribute to the inherent noisiness of real guided wave signals. Accurately replicating such noise in simulation signals necessitates a careful characterisation of noise sources and features, followed by their precise modelling in the simulation.

In addition, guided wave monitoring systems installed in the field are subject to various environmental factors, such as temperature variations [16, 32], humidity [33], and the presence of external noise sources [34]. These factors have complex interactions with guided wave signals and also contribute to gradual system degradation, which causes the behaviour of the system to change over time. Currently, the challenge remains in faithfully incorporating environmental conditions into the simulation and depicting their influence over time. Researchers have made some efforts to reflect the environmental effects on generated guided wave signals. For instance, Liu et al. [35] proposed a hybrid data generation framework, which superposes artificial damage signals with a set of baselines collected on an undamaged structure, under different environmental conditions. However, it is challenging and expensive to collect baselines that cover a wide range of measurement conditions and uncertainties through experiments, and the degradation of the monitoring system over time is not taken into account.

Furthermore, real-world pipelines generally have unavoidable geometrical imperfections, such as wall thickness variations [36]. However, there is little understanding of how these initial geometric imperfections contribute to the noisiness of real guided wave signals. Consequently, assumptions of nominal geometry are often made, which deviate from real practical cases and affect the fidelity of simulation-generated data.

1.2 Thesis outline

This thesis presents a feasible solution for estimating the detection reliability of guided wave SHM systems, defined in terms of their probability of detecting defects with a specified level of confidence, by developing highly realistic numerical models. It introduces a methodology for analysing coherent and random noise features of real guided wave signals, upon which a numerical framework for generating realistic guided wave signals is built. For the reliability estimation of SHM systems, a digital twin-based framework is proposed and demonstrated to provide timely performance evaluations for SHM systems specific to environmental conditions throughout their entire lifecycle. To demonstrate the approach, this thesis focuses on pipelines, which represent one of the most common and industrially relevant applications of guided wave SHM, without loss of generality. Additionally, the contribution of initial geometric imperfections in pipes to the noisiness of guided wave signals is investigated, aiming to understand the necessity of modelling these imperfections in realistic numerical simulations.

Following a brief introduction to the motivation of this thesis in Chapter 1, Chapter 2 reviews the theory of guided waves propagating in a pipe, providing a theoretical understanding of guided wave signals. It then explains and demonstrates how to analyse the noise features of real guided wave signals based on representative experimental data collection and what contributes to these noise features. This understanding forms the foundation for modelling noise features in realistic simulations.

Chapter 3 describes a numerical framework for generating realistic guided wave signals, incorporating both random and coherent noise induced by transducer performance imbalance. The validity of this framework is tested on both numerical data and experimental data collected in a laboratory environment. The realistic synthetic data generated by the proposed framework is used to estimate the inspection range of a guided wave testing system on a pipe, illustrating its advantages over common industrial practices and traditional ideal simulations. The methodology for estimating transducer performance is explored for coherent noise reduction in guided wave signals.

In Chapter 4, a digital twin-based framework is proposed as a practical solution for estimating the reliability of SHM systems in real-world conditions. The chapter introduces a method for creating a digital twin model that mirrors real-time measurement conditions using in-situ measurements. This method is validated with experimental signals with temperature variations collected through both laboratory instruments and commercial transducer rings. To evaluate the digital twin model's performance in reliability estimation, POD analysis is conducted using data generated by the digital twin model and compared with data from the established superposition method. Finally, the chapter demonstrates how the framework provides timely reliability estimations throughout the system's lifecycle, highlighting its advantages over traditional model-assisted reliability estimation methods commonly used in the NDE field.

Chapter 5 investigates the influence of initial geometric imperfections in pipes, specifically focusing on the coherent noise features of guided wave signals. This chapter examines wall thickness variation patterns based on the pipes used throughout this thesis. It then investigates the impact of wall thickness variations within industry-specified tolerances using FE simulations, revealing the underlying mechanisms influencing wave excitation and propagation.

The concluding remarks of this thesis are summarised in Chapter 6, along with a discussion of the main findings and perspectives for future work.

Chapter 2

Real-world characteristics of guided wave signals: noise

2.1 Introduction

High-fidelity model-based data generation for reliability estimation requires a good understanding of the complexity of real guided wave signals. One notable characteristic of these signals is the presence of noise, which can be broadly categorised into coherent noise and random noise. Coherent noise refers to structured signal components that are consistently present across repeated measurements under the same conditions, often resulting from system responses, wave reflections, or mode conversions that are not associated with defects. In contrast, random noise represents unstructured and unpredictable variations in the signal, typically introduced by electronic noise, environmental fluctuations, or measurement uncertainties. The performance of a guided wave SHM system is strongly influenced by its ability to distinguish true defect signals from these noise sources. Therefore, faithfully capturing both types of noise in model-based data is essential for accurate model-based reliability estimation. A clear understanding of their respective characteristics is a prerequisite for developing effective noise modelling strategies.

Random noise can originate from various sources, including electronic noise in the measurement system and environmental noise. It is typically characterised based on the statistical analysis of random noise signals. Coherent noise generally arises from physical wave phenomena, such as scattering from rough surfaces, mode conversions, and the presence of other guided wave modes in the structure. Determining the formation of coherent noise is typically more challenging. In this chapter, a methodology to analyse the sources and characteristics of noise is presented based on real guided wave signals, with demonstration focused on pipe structures as they represent a common and practical application of guided wave SHM.

Both the interpretation of guided wave signals and the analysis of the coherent noise require a good understanding of the wave theory behind them. Therefore, prior to the analysis of noise features, this chapter briefly discusses the theory related to wave propagation in pipes. The wave theories related to axial guided waves and circumferential guided waves are summarised, and the wave modes are analysed based on dispersion curves. Furthermore, the methodology for analysing noise is proposed based on experimental noise collection. The analysis of noise features in guided wave signals from the SHM system used in this thesis is presented using the proposed method.

2.2 Guided waves in pipes

In an unbounded, infinite, isotropic, elastic medium, waves can propagate as bulk shear or longitudinal waves. In a bounded medium such as pipes, different modes of guided waves can propagate due to a superposition of the bulk waves within the boundaries. Depending on the direction of wave propagation, these guided waves in a pipe can be categorised as axial guided waves and circumferential guided waves. The theory describing the wave propagation behaviours and the characteristics of different wave modes are discussed here.

2.2.1 Axial guided waves

2.2.1.1 Guided wave theories

The theory of wave propagation in pipes, or hollow cylinders, is thoroughly documented across a multitude of studies [37, 38] and is extensively covered in several textbooks [39, 40]. The theory related to this work is briefly presented here for understanding the coherent noise arising from imperfect wave excitation conditions in practice.

The analysis of axial guided waves in a pipe is presented here, and is based on Rose's derivation [39]. The behaviour of waves can be described by solving the governing wave equations with appropriate boundary conditions corresponding to a hollow cylindrical pipe.

For an elastic isotropic pipe, Navier's equation of motion in terms of the displacement field $\mathbf{u}$ is written as follows

$$\mu \nabla^2 \mathbf{u} + (\lambda + \mu) \nabla \nabla \cdot \mathbf{u} = \rho \frac{\partial^2 \mathbf{u}}{\partial t^2}, \tag{2.1}$$

where μ and λ are the Lamé constants, ρ is the density, and t indicates time.

According to the Helmholtz decomposition for isotropic media, the displacement $\mathbf{u}$ can be decomposed as the sum of a compressional scalar potential ϕ

and an equivoluminal potential vector $\mathbf{H}$:

$$\mathbf{u} = \nabla\phi + \nabla \times \mathbf{H}, \tag{2.2}$$

with a gauge invariance condition that ensures the uniqueness of the decomposition. Here we choose to make the equivoluminal vector potential $\mathbf{H}$ a zero-divergence vector, that is,

$$\nabla \cdot \mathbf{H} = 0, \tag{2.3}$$

which is applicable for an infinity-long pipe without any sources or sinks within the region.

Substituting Eq. (2.2) into Eq. (2.1) leads to two independent wave equations:

$$\begin{aligned} \nabla^2\phi &= \frac{1}{c_l^2}\frac{\partial^2\phi}{\partial t^2} \\ \nabla^2\mathbf{H} &= \frac{1}{c_s^2}\frac{\partial^2\mathbf{H}}{\partial t^2}, \end{aligned} \tag{2.4}$$

where

$$c_l = \sqrt{\frac{\lambda + 2\mu}{\rho}}, \;\; c_s = \sqrt{\frac{\mu}{\rho}}, \tag{2.5}$$

which correspond to the longitudinal wave velocity and shear wave velocity, respectively.

For describing waves propagating in a pipe, cylindrical coordinates are appropriate. A schematic of the pipe geometry and the definition of cylindrical coordinates are shown in Figure 2.1. z represents the axial direction, r is the radial direction, and θ is the circumferential direction. r_1 and r_2 are the inner radius and outer radius of the pipe, respectively.

The solution of the Helmholtz Eq. (2.4) is separable, hence it can be split

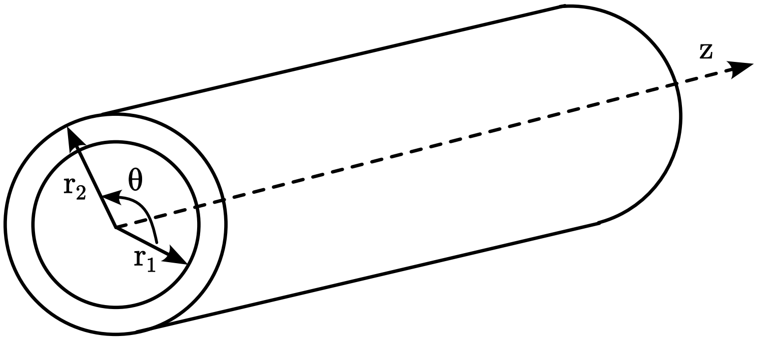

Figure 2.1: Schematic of a pipe and the cylindrical coordinate system. z represents the axial direction, r is the radial direction, and θ is the circumferential direction. r_1 and r_2 are the inner radius and outer radius of the pipe, respectively.

into the product of functions of each spatial dimension. For harmonic wave propagation, the solution can be expressed as

$$\phi, \mathbf{H} = \Xi_1(r)\Xi_2(\theta)\Xi_3(z)e^{i(\mathbf{k}\cdot\mathbf{R}-\omega t)}, \tag{2.6}$$

where $\mathbf{k}$ is the wavenumber, $\mathbf{R}$ is the position vector, ω is the angular frequency, and i is the imaginary unit. $\Xi_1(r)$, $\Xi_2(\theta)$, and $\Xi_3(z)$ describe how the field varies in each coordinate.

For waves propagating in the axial direction, assuming that the displacement field does not vary in the circumferential or axial direction, the compressional scalar potential ϕ and the equivoluminal vector $\mathbf{H}$ can be expressed as

$$\begin{aligned} \phi &= f(r)e^{in\theta}e^{i(kz-\omega t)} \\ H_r &= h_r(r)e^{in\theta}e^{i(kz-\omega t)} \\ H_\theta &= h_\theta(r)e^{in\theta}e^{i(kz-\omega t)} \\ H_z &= h_z(r)e^{in\theta}e^{i(kz-\omega t)}, \end{aligned} \tag{2.7}$$

where n is the circumferential order, which must be an integer to ensure the continuity of motion in the circumferential direction of a pipe, k is the wavenumber component in the axial direction.

Substituting Eq. (2.7) into Eq. (2.4) yields a series of second-order Ordinary Differential Equations (ODEs) as follows

$$\begin{aligned} r^2f^{''}+rf^{'}+\left[(\frac{\omega^2}{c_l^2}-k^2)r^2-n^2\right]f=0 \\ r^2h_1^{''}+rh_1^{'}+\left[(\frac{\omega^2}{c_s^2}-k^2)r^2-(n^2+1)\right]h_1=0 \\ r^2h_2^{''}+rh_2^{'}+\left[(\frac{\omega^2}{c_s^2}-k^2)r^2-(n^2-1)\right]h_2=0 \\ r^2h_3^{''}+rh_3^{'}+\left[(\frac{\omega^2}{c_s^2}-k^2)r^2-n^2\right]h_3=0, \end{aligned} \tag{2.8}$$

where

$$\begin{aligned} &2h_1=ih_r-h_\theta,\ \ 2h_2=ih_r+h_\theta,\ \ h_3=h_z \\ &\alpha^2=\frac{\omega^2}{c_l^2}-k^2, \qquad \varsigma^2=\frac{\omega^2}{c_s^2}-k^2 \\ &\alpha_1=|\alpha|, \qquad\qquad\ \varsigma_1=|\varsigma|, \end{aligned} \tag{2.9}$$

for the simplification of the solutions.

The equations in (2.8) have the form of Bessel's differential equations and can be solved by selecting appropriate Bessel functions. More details on the choice of Bessel functions can be found in [41]. The solutions of Eq. (2.8) have the following form:

$$\begin{aligned} h_1&=A_1Z_{n+1}(\varsigma_1r)+B_1W_{n+1}(\varsigma_1r) \\ h_2&=A_2Z_{n-1}(\varsigma_1r)+B_2W_{n-1}(\varsigma_1r) \\ h_3&=A_3J_n(\varsigma_1r)+B_3Y_n(\varsigma_1r) \\ f&=A_4J_n(\alpha_1r)+B_4Y_n(\alpha_1r), \end{aligned} \tag{2.10}$$

where J_n and Y_n are the nth order Bessel functions, the detailed expressions of which can be found in [39], and A_q $(q = 1, 2, 3, 4)$ and B_q $(q = 1, 2, 3, 4)$ are the unknown coefficients to be determined.

According to Eq. (2.2), the three displacement components in the r, θ, and z directions can be expressed in terms of f, h_1, h_2, and h_3. Based on Hooke's Law and strain-displacement relations, the stress field can be derived with an expression in terms of f, h_1, h_2, and h_3 as well. The detailed expressions for the displacement field and stress field won't be listed here, as they can be found in [41].

For a traction-free pipe with infinite length, the boundary conditions on the inner $(r = r_1)$ and outer $(r = r_2)$ surfaces are given as follows:

$$\sigma_{rr} = \sigma_{r\theta} = \sigma_{rz} = 0, \quad r = r_1 \quad \text{and} \quad r = r_2. \tag{2.11}$$

In combination with the gauge invariance condition in Eq. (2.3) on the inner and outer surfaces of the pipe, an eigenvalue equation with eight unknown variables can be obtained:

$$\mathbf{C}\begin{bmatrix} A_4 \\ B_4 \\ \vdots \\ B_3 \end{bmatrix} = \begin{bmatrix} C_{11} & C_{12} & \dots & C_{18} \\ C_{21} & C_{22} & \dots & C_{28} \\ \vdots & \vdots & \ddots & \vdots \\ C_{81} & C_{82} & \dots & C_{88} \end{bmatrix} \begin{bmatrix} A_4 \\ B_4 \\ \vdots \\ B_3 \end{bmatrix} = \begin{bmatrix} 0 \\ 0 \\ \vdots \\ 0 \end{bmatrix}, \tag{2.12}$$

where the detailed expression of the elements in the coefficient matrix $\mathbf{C}_{8\times 8}$ can be found in [39]. This equation is called the characteristic equation and it describes the behaviours of axial guided waves in a pipe. A dispersion curve shows how the phase velocity or group velocity of a wave mode varies with frequency, and is fundamental for understanding wave propagation characteristics in a structure. The dispersion curves of the axial wave modes can be obtained by numerically solving the eigenvalues of this characteristic equation, and the corresponding eigenvectors describe the mode shape of each wave mode. In this thesis, a general-purpose software tool, DISPERSE [42], developed by Lowe and Pavlakovic at Imperial College London, is used for the calculation of dispersion curves.

The axial guided waves in a pipe can be grouped into longitudinal mode, torsional mode, and flexural mode, according to the particle motion direction of each wave mode. Both the longitudinal mode and torsional mode have axisymmetric wave motions, and the circumferential order n of these modes is zero. The longitudinal modes have predominant particle motions in the axial direction, while the torsional modes have particle motions primarily in the circumferential direction. The flexural modes have non-axisymmetric wave motions that include components in all three directions. Following the notation defined by Silk and Bainton [43], longitudinal modes are denoted as L(0,m), torsional modes are denoted as T(0,m), and flexural modes are denoted as F(n,m). In these notations, n is the circumferential order of a wave mode, which describes the number of wavelengths around the pipe circumference, and m is a counter number that roughly reflects the wave motions through the wall thickness of a pipe.

Figure 2.2 shows the phase velocity dispersion curves and the group velocity dispersion curves of an 8-inch Schedule 80 steel pipe, which is one of the pipes used in the experiments in this thesis. Here, “Schedule 80” refers to a standardised designation indicating the pipe’s wall thickness, as defined by the ASME/ANSI B36.10 specification [44]. In Figure 2.2a, only lower-order wave modes are presented for a clear view, while higher-order wave modes exist within the frequency range that is typically used for guided wave testing (below 150 kHz) [45]. The dispersion curves show the possible wave modes that may propagate in a pipe, however, the exact wave modes propagating in a pipe depend on certain excitation conditions.

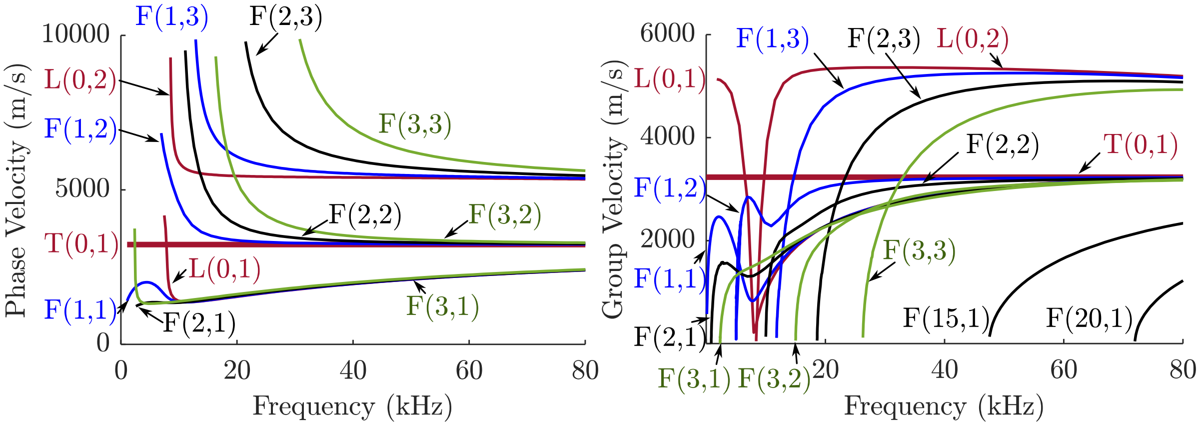

(a) (b)

Figure 2.2: Dispersion curves of axial guided waves for an 8-inch Schedule 80 steel pipe, which is one of the pipes used in the experiments in this thesis . (a) Phase velocity dispersion curves, (b) group velocity dispersion curves.

2.2.1.2 Guided wave testing based on T(0,1) mode

The fundamental torsional mode, T(0,1), is the most common axial guided wave mode used for defect detection in pipes for several reasons. The T(0,1) wave mode is included in Figure 2.2 (highlighted in bold line). Its constant wave velocity across the whole frequency range, which means that it is non-dispersive, enables it to propagate for a longer distance with minimal energy spread, therefore covering a larger inspection area compared to other dispersive modes. Furthermore, for pipes surrounded by low-viscosity fluids, such as water, the T(0,1) wave mode does not leak to the surrounding fluid due to its shear behaviour having no matching motion in the fluid and therefore removing the possibility of transmission. Additionally, the frequency range commonly employed for pipe inspection is within a lower kilohertz regime [45], which is generally below the cutoff frequency of the second-order torsional mode, T(0,2). In the context of the pipe examined in this study, the T(0,2) mode cutoff frequency is approximately 140 kHz. Therefore, excitation of pure T(0,1) is easier since there are no similar modes below the cutoff frequency. By contrast, exciting the L(0,2) mode requires careful consideration because the L(0,1) mode also exists below the cutoff frequency, which is why more recent commercial application of guided wave testing has moved from L(0,2) to T(0,1). Moreover, the T(0,1) wave mode has nearly uniform wave motion through the thickness of the pipe wall, as shown in Figure 2.3, which gives it similar sensitivity to defects on both the inner and outer surfaces.

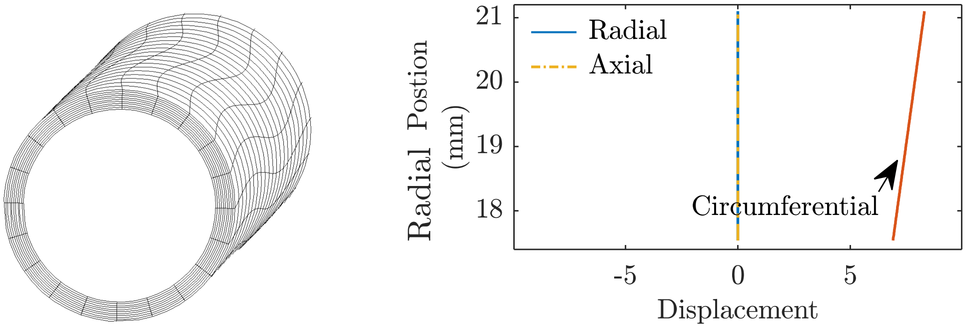

(a) (b)

Figure 2.3: T(0,1) mode shape. (a) Torsional mode motion, (b) T(0,1) mode shape, which describes the three displacement components through the thickness of the pipe wall. T(0,1) mode has no axial or radial displacement component, and the circumferential displacement is nearly uniform through the thickness of the pipe wall. The displacement is shown on an arbitrary scale.

Careful excitation of a wave mode is necessary for reliably interpreting guided wave signals for pipe monitoring. The pure excitation of a specific wave mode has been discussed in detail in [41]. A pure mode can be excited by applying a displacement profile that properly matches the mode shape of a wave mode, owing to the nature of mode orthogonality. A higher-order flexural mode usually has a more complex mode shape, making it difficult to precisely control the mode excitation and requiring a prohibitively complex transducer configuration. This is also why only lower-order wave modes, such as T(0,1) and L(0,2), are used for guided wave testing in practice.

In theory, a pure T(0,1) mode can be excited by applying a uniform circumferential displacement throughout the entire cross-section of a pipe. However, in practical scenarios, this wave mode is typically excited by a series of shear-force transducers, uniformly spaced around the pipe circumference to apply circumferential forces. To successfully excite the T(0,1) wave mode, two key criteria must be met. First, the distance between transducers — referred to as the transducer element pitch — should not exceed half the wavelength of the targeted wave. Adhering to this spacing is essential for the constructive interference of the waves emitted by each transducer, which leads to the formation of coherent T(0,1) plane waves while preventing the emergence of grating lobes [46, 47]. Second, to effectively suppress flexural modes, the number of transducers positioned around the pipe's circumference must be greater than the highest order of flexural modes anticipated within the selected frequency range. For instance, in an 8-inch Schedule 80 steel pipe examined at 50 kHz, the highest order of flexural mode that may occur up to a frequency of 80 kHz is the 20th order, as depicted in Figure 2.2b, and the half-wavelength of the T(0,1) mode is approximately 32 mm. Consequently, a minimum of 22 equidistant transducers must encircle the pipe to satisfy the spatial sampling and flexural mode suppression requirements in this case, thereby ensuring pure excitation of the T(0,1) mode.

The excitation of a pure T(0,1) mode relies on a series of ideal assumptions, such as perfect alignment of the transducers around the pipe circumference, uniform performance of all transducers, and flawless finishing of the pipe surface. In practice, imperfections always exist, which may lead to coherent noise.

Figure 2.4 illustrates a typical guided wave signal acquired and processed by a commercial guided wave monitoring system from Guided Ultrasonics Ltd. (GUL). The T(0,1) guided wave signal is displayed on a logarithmic scale. Alongside the reflections from the pipe weld features, discernible noise

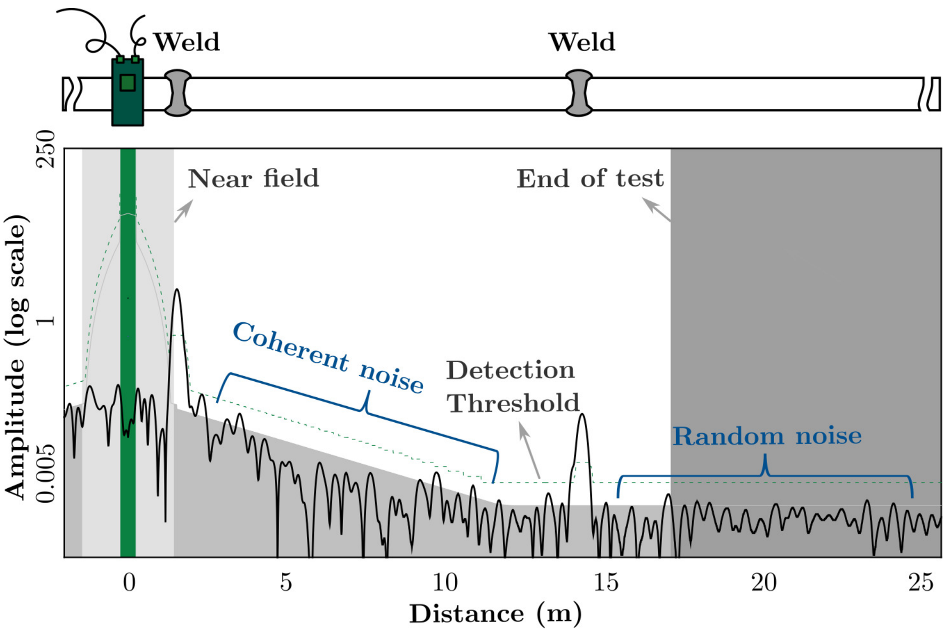

Figure 2.4: A typical guided wave signal (on the logarithmic scale) acquired by GUL on a pipe with two weld features.

is also present.

As mentioned before, the noise within a guided wave signal consists of both random noise and coherent noise. Random noise originates from electrical interference in the measurement system or environmental vibrations and exhibits stochastic randomness. It maintains a consistent amplitude with respect to distance from the transducer ring. Coherent noise, on the other hand, exhibits diminishing amplitude with wave propagation distance, manifesting as a linear decay on the logarithmic scale due to damping and beam spread effects.

Coherent noise results from physical wave behaviours, including the excitation of unwanted axial flexural modes and imperfect cancellation of circumferential waves. Therefore, the theory of circumferential guided waves in a pipe will be summarised in the next section for a better understanding of coherent noise.

2.2.2 Circumferential guided waves

While circumferential guided waves in pipes are less discussed compared to axial guided waves, there is increasing interest in applying them to detect axial cracks and monitor corrosion over short distances [48–51]. GUL has successfully developed an innovative testing system called QSR (Quantitative Short Range) [52] for measuring corrosion, especially at pipe locations with limited access, such as pipe support locations. In this section, the theory of circumferential guided waves, as well as a comparison with those in a plate with the same thickness, will be presented.

The guided waves propagating in the circumferential direction of a pipe are similar to those propagating in a plate, especially when wall thickness can be taken as small compared to the pipe diameter. The similarities between circumferential guided waves in a pipe and guided waves in a plate have been discussed in detail in [53]. Similarly to guided waves in a plate, circumferential Shear Horizontal (SH) waves and circumferential Lamb waves can be discussed separately owing to the decoupling in wave equations.

2.2.2.1 Circumferential SH waves

As with the analysis of axial guided waves, the analysis of circumferential waves also starts from Navier's equation of motion in Eq. (2.1). For circumferential SH waves, the particle motions only have axial components, that is, $u_r = u_\theta = 0$. The plane strain condition is applicable for an infinitely long pipe, that is, $\partial/\partial z = 0$. Under these conditions, Navier's equation of motion, Eq. (2.1), is simplified as

$$\nabla^2 u_z = \frac{1}{c_s^2}\frac{\partial^2 u_z}{\partial t^2}. \tag{2.13}$$

Assuming a time-harmonic wave propagating in the circumferential direction of a pipe, the solution of Eq. (2.13) can be expressed as

$$u_z = \psi(r)e^{i(p\theta - \omega t)}, \tag{2.14}$$

where $\psi(r)$ describes the wave motion through the thickness of the pipe wall. p is the angular wavenumber, which is related to the wavenumber k as

$$p = kr, \tag{2.15}$$

where r is the radial location where the linear phase velocity is determined. The linear phase velocity of a circumferential wave mode, c_p, is calculated as

$$c_p(r) = \frac{\omega}{p}r, \tag{2.16}$$

which means that the linear phase velocity of a circumferential wave mode increases linearly from the inner surface to the outer surface of a pipe. This is necessary to maintain a constant angular phase velocity through the thickness of a pipe wall when guided waves are propagating around the pipe circumference.

The procedure to derive the characteristic equation of circumferential guided waves is similar to that applied to axial guided waves. Substitute the potential solution, Eq. (2.14), into the simplified wave equation, Eq. (2.13), and an expression of $\psi(r)$ in terms of Bessel functions can be obtained as

$$\psi(r) = A_1 J_p(k_s r) + A_2 Y_p(k_s r), \tag{2.17}$$

where A_1 and A_2 are the unknown coefficients to be determined, J_p and Y_p are the pth order Bessel functions, and k_s is the wavenumber of shear bulk waves, i.e., $k_s = \frac{\omega}{c_s}$. It should be noted that the order of Bessel functions, p, is not necessarily an integer, as suggested in Eq. (2.15).

Sequentially, the displacement and stress components can be expressed in terms of the unknown coefficients, A_1 and A_2, and the Bessel functions. Applying the traction-free boundary conditions of a free pipe, $\sigma_{rz}|_{r_1,r_2} = 0$, yields a set of linear homogeneous equations as

$$\mathbf{DA} = \begin{bmatrix} D_{11} & D_{12} \\ D_{21} & D_{22} \end{bmatrix} \begin{bmatrix} A_1 \\ A_2 \end{bmatrix} = \begin{bmatrix} 0 \\ 0 \end{bmatrix}, \tag{2.18}$$

where the detailed expression of the coefficient matrix $\mathbf{D}$ and the selection of Bessel functions can be found in [39].

The characteristic equation of circumferential SH waves is obtained by setting the determinant of the coefficient matrix $\mathbf{D}$ to zero, that is

$$det(\mathbf{D}(p, \omega)) = 0, \tag{2.19}$$

the eigenvalues of which form the dispersion curves of circumferential SH modes, and the corresponding eigenvectors describe the mode shape of each mode.

2.2.2.2 Circumferential Lamb waves

For circumferential Lamb waves, the particle motion occurs in both the radial and circumferential directions, i.e., $u_r \neq 0$, $u_\theta \neq 0$, and $u_z = 0$. Imposing the plane strain condition for an infinitely long pipe ($1/\partial z = 0$) leads to

$$H_r = H_\theta = 0. \tag{2.20}$$

For a time-harmonic wave propagating in the circumferential direction of a pipe, the solution of the Helmholtz equations, Eq. (2.4), can be written as

$$\begin{aligned}\phi &= f(r)e^{i(p\theta-\omega t)}\\ H_z &= h_z(r)e^{i(p\theta-\omega t)}.\end{aligned} \tag{2.21}$$

Substituting Eq. (2.21) into the Helmholtz wave equations, Eq. (2.4) leads to a set of second-order linear ODEs. The unknown factors in Eq. (2.21) can be expressed by a series of unknown coefficients and Bessel functions as follows

$$\begin{aligned}f(r) &= A_1 J_p(k_l r) + A_2 Y_p(k_l r)\\ h_z(r) &= A_3 J_p(k_s r) + A_4 Y_p(k_s r),\end{aligned} \tag{2.22}$$

where A_1, A_2, A_3, and A_4 are unknown coefficients to be determined, and k_l is the wavenumber of longitudinal bulk waves, i.e., $k_l = \frac{\omega}{c_l}$.

Similarly, a series of linear equations regarding A_1, A_2, A_3, and A_4 can be obtained by applying traction-free boundary conditions, i.e., $\sigma_{rr} = \sigma_{r\theta} = 0$. The characteristic equation of circumferential Lamb waves is derived by setting the determinant of this linear system to zero. Subsequently, the dispersion curves and corresponding mode shapes can be determined by solving the characteristic equation of circumferential Lamb waves. Further details and related equation expressions can be found in [39].

2.2.2.3 Dispersion curves

The dispersion curves of circumferential SH waves and circumferential Lamb waves are computed using DISPERSE, based on an 8-inch Schedule 80 steel pipe. The pipe's geometry matches that used for calculating the axial dispersion curves shown in Figure 2.2. Additionally, dispersion curves for a plate with the same thickness (13.3 mm) are calculated for comparison.

Figure 2.5 compares the dispersion curves of circumferential SH waves and circumferential Lamb waves with those in a plate. It is worth mentioning

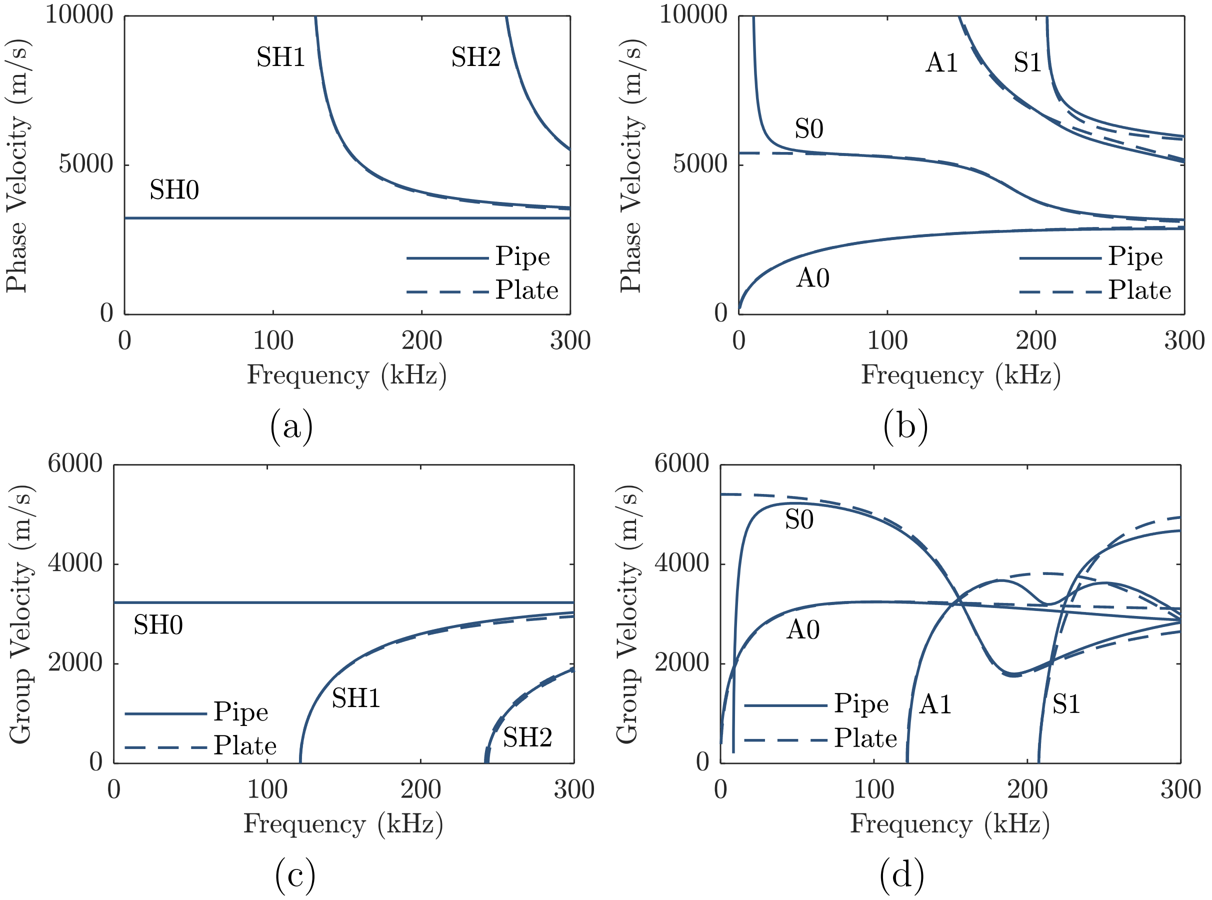

(a) (b) (c) (d)

Figure 2.5: Dispersion curves of circumferential guided waves for an 8-inch Schedule 80 steel pipe (solid lines), compared with that of a plate with the same thickness of 13.3 mm (dotted lines). (a) Phase velocity dispersion curves of SH waves, (b) phase velocity dispersion curves of Lamb waves, (c) group velocity dispersion curves of SH waves, and (d) group velocity dispersion curves of Lamb waves.

that the dispersion curves of circumferential wave modes in Figure 2.5 are shown as linear quantities with a radius of 96.3 mm (outer radius), at which wave velocities are calculated. For this pipe with a thickness-to-radius ratio of 0.1214, the dispersion curves of circumferential modes in the pipe roughly agree with those in the plate. Compared to the Lamb waves, there is less discrepancy in the wave velocities of SH waves within the frequency range below 300 kHz. However, larger divergence occurs at lower frequencies (below

50 kHz) for the S0 mode and at higher frequencies (above 200 kHz) for the S1 mode. Care needs to be taken when applying plate wave analogy for these two wave modes within these frequency ranges.

2.3 Noise analysis

The accurate modelling of noise necessitates a thorough understanding of its features. This section propose and demonstrate an experimental signal-based noise analysis methodology for the purpose of noise modelling.

2.3.1 Methodology

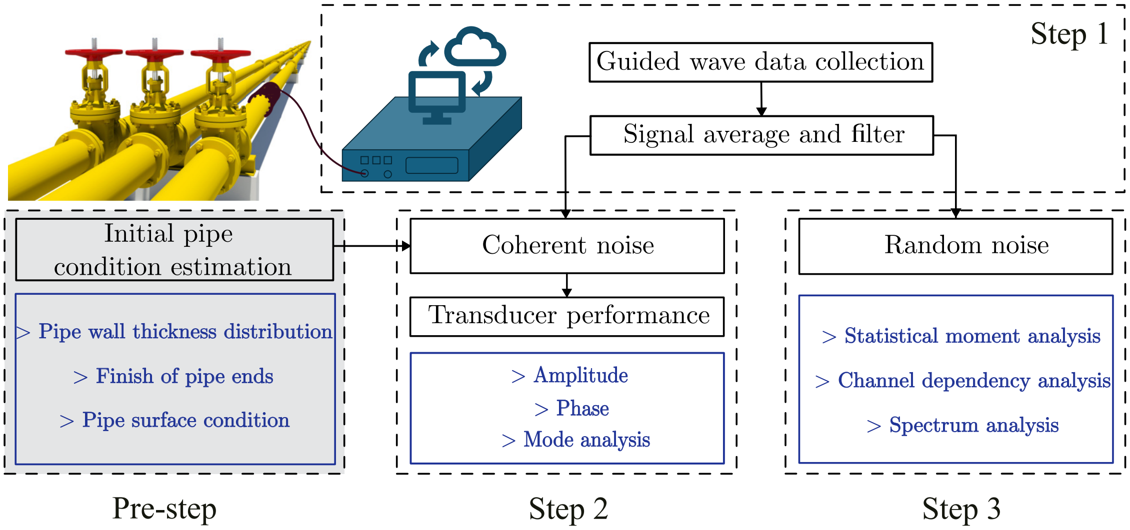

Figure 2.6: Flowchart describing the method for noise feature analysis based on experimental signals.

A flowchart illustrating the methodology for noise feature analysis, consisting of one pre-step and three subsequent steps, is presented in Figure 2.6.

2.3.1.1 Pre-step: initial pipe condition estimation

In the pre-step, initial pipe conditions under investigation are estimated. These include the distribution of pipe wall thickness, the finishing condition of the pipe ends, and the surface condition of the pipe. These initial estimations can be conducted using common NDE methods, such as visual inspection and ultrasound testing. If noticeable variations in pipe wall thickness, angled pipe ends, or rough pipe surfaces are detected, these factors must be incorporated into the simulation model to account for their contribution to coherent noise.

These imperfect pipe conditions may contribute to coherent noise in guided wave signals in various ways. For instance, the rough pipe surface can affect the coupling condition between the transducers and the pipe, thereby altering the excitation and reception of signals from each transducer and potentially leading to the excitation of unwanted wave modes. Additionally, scattering from the rough surface of the pipe also contributes to coherent noise. When the pipe end is angled due to imperfect pipe end finishing, it may induce strong mode conversions at the end of the pipe, contributing to coherent noise. The influence of geometrical imperfections on the coherent noise of guided wave signals will be discussed in detail in Chapter 5.

2.3.1.2 Step 1: noise collection

The first step of noise analysis involves collecting both random noise and coherent noise. As mentioned earlier and depicted in Figure 2.4, coherent noise arises from physical wave phenomena and its amplitude decays with wave propagation distance, while random noise remains at a constant level. To collect random noise, a long-duration signal collection is performed until a constant signal amplitude is observed on a logarithmic scale, indicating that guided wave signals dissipate sufficiently to a level below that of the random noise and mainly random noise remains. Coherent noise, on the other hand, can be collected from the signal between reflections from pipe features, sufficiently early in the signal that its amplitude is much larger than any random noise present, such as the signal between the first weld reflection and the second weld reflection, as marked in Figure 2.4.

Before noise collection, the guided wave signals undergo common signal processing techniques: signal averaging and signal filtering. Random noise can be reduced through averaging multiple signals together because of its stochastic randomness and zero means. The different realisations of random noise sum incoherently and are reduced in amplitude, while the features that remain constant between the measurements, such as defect responses, are enhanced. Assuming that the noises have the same Root Mean Square (RMS) for every realisation, combining M signals can increase the Signal-to-Noise Ratio (SNR) by $10\log_{10} M$ dB, where SNR is defined as $20\log_{10}\frac{\sigma_s}{\sigma_n}$, with σ_s representing the RMS of the signal component and σ_n representing the RMS of the random noise component.

The guided wave signals are then filtered in the postprocessing using a bandpass filter with a frequency band of $[f_{low}, f_{upper}]$ to eliminate extraneous noise beyond the frequency range of interest, where f_{low} and f_{upper} are the lower and upper frequency limit, respectively. The bandpass filter limits are determined through trials, adjusting them and assessing the noise level compared to the desired response from the system.

Data is collected using two distinct acquisition strategies for different analyses: Full Matrix Capture (FMC) and Common Source Method (CSM) [54]. In the FMC approach, each transmitter is activated in sequence, with all receivers capturing the signals. This process creates a comprehensive transmit-receive matrix, incorporating the pulse-echo response from each transducer. The T(0,1) signal is derived by summing the matrix elements. Conversely, the CSM technique involves the simultaneous excitation of all transmitters, generating an axial plane wave. A T(0,1) signal can be obtained by summing all signals concurrently recorded from all receivers.

2.3.1.3 Step 2: coherent noise analysis

The second step involves analysing coherent noise, focusing on the imbalance of transducer performance, which has been identified as one of the most significant factors contributing to coherent noise [55]. During this step, the imbalance in transducer performance is analysed in terms of the variations in signal amplitude and phase, and the composition of the coherent noise is examined through mode analysis. It is important to note that the output from each transducer is influenced by all the electrical and electro-mechanical components present in the measurement system, including the pulser, cables, transducers, amplifiers, and transducer coupling conditions. Specifically, the pulser generates the excitation pulse that drives the transducer; the cables transmit the electrical signal between system components; the transducer converts electrical energy to mechanical waves (and vice versa); the amplifier boosts weak signals to detectable levels; and the coupling conditions affect how efficiently energy is transferred between the transducer and the structure. Therefore, the discussion of transducer performance in this thesis encompasses all factors that may affect the generation and reception of guided waves in the signal generation and reception process.

To assess transducer performance, signals are acquired using the FMC method. The pulse-echo signal from each transducer channel undergoes a windowing process to effectively isolate a clear wavepacket. The amplitude and phase of these windowed signals are then quantified in the frequency domain. At the central excitation frequency, variations in amplitude and phase are indicative of differences in transducer performance when inspecting an axisymmetric pipe. Further analysis is carried out to evaluate the potential excitation of flexural modes of different circumferential orders. A Fourier analysis of amplitude variations across the transducer array around the pipe circumference is performed. This analysis identifies the presence of unwanted flexural modes when a pure axisymmetric wave is desired.

The composition of the coherent noise is then analysed based on mode analysis. Coherent noise arises from the imperfect cancellation of circumferential waves and the excitation of unwanted flexural wave modes. Circumferential waves are predominantly present at the beginning of the signal, with their amplitude decaying due to the material damping and the beam spread effect. On the other hand, unwanted flexural wave modes can only be detected when they are reflected from pipe features and become predominant in the later part of the signal due to wave superposition and reverberation. The point determining the presence of axial flexural modes can be identified with the assistance of simulation or analytical analysis, based on the wave travelling distance and the wave speed of a specific flexural mode.

2.3.1.4 Step 3: random noise analysis

The third step involves the analysis of random noise through statistical analysis. Random noise is commonly represented using Gaussian white noise [56], with its intensity primarily dependent on the measurement system and ambient environment. The analysis of random noise includes statistical moment analysis, spectrum analysis, and channel dependency analysis.

Firstly, two fundamental statistical moments, namely skewness and kurtosis, are employed to gauge the deviation of the collected random noise distribution from normality [57, 58]. skewness, γ_1, and kurtosis, γ_2, are defined as

$$\gamma_1 = \frac{E[(X-\eta)^3]}{E[(X-\eta)^2]^{3/2}}, \tag{2.23}$$

and

$$\gamma_2 = \frac{E[(X-\eta)^4]}{E[(X-\eta)^2]^2}, \tag{2.24}$$

where $E[\cdot]$ denotes the expectation operator, X is the data point, and η is the mean value of the data. skewness quantifies the asymmetry of the distribution around the sample mean, while kurtosis indicates the degree of flatness near the distribution centre. For a Gaussian distribution, skewness and kurtosis are equal to 0 and 3, respectively. Then, the Probability Density Function (PDF) of the random noise collected in the experiments is compared with that of an ideal Gaussian distribution to confirm the distribution of the random noise.

To determine if the noise power spectrum maintains its “white” characteristics after filtering, the Power Spectral Density (PSD) of the random noise signal is computed and then compared with the PSD of a reference Gaussian white noise signal that has a matched power level, with both subjected to the same bandpass filter. Furthermore, to understand how the random noise varies across individual channels, the noise signals are recorded using the CSM. For each transducer channel, the RMS value of the noise is computed, providing insight into the channel-specific noise behaviour.

2.3.2 Experimental demonstration

In this section, the method proposed for the analysis of noise will be demonstrated based on the laboratory experiments. A comprehensive analysis of the noise signal is performed based on the guided wave signals collected from an experimental setup within a controlled laboratory environment at a room temperature of around 23 °C and humidity of around 25%. This analysis serves as the basis for the subsequent modelling of noise in the simulations in the following chapters.

2.3.2.1 Noise collection

In the experiments, two API (American Petroleum Institute) standard seamless carbon steel pipes of different sizes, Pipe 1 and Pipe 2, as listed in Table 2.1, were tested. The material properties of the pipes were referenced from a public engineering material database [59] but were calibrated based on the wave velocities measured experimentally to account for variations in material properties due to uncertainty in the exact processing parameters during manufacturing. The geometric and material information of the pipes is detailed in Table 2.1, and the experimental setup is illustrated in Figure 2.7.

Table 2.1: Geometric and material information of the instrumented pipes used in the experiments.

	Geometric					**Material**	**Material Properties**			
	Nominal Size (inches)	**Schedule**	**Outside Diameter (mm)**	**Wall Thickness (mm)**	**Length (mm)**		**Density (kg/m^3)**	**Young's Modulus (GPa)**	**Poisson's Ratio**	**Mass Proportional Damping Coefficient (Hz)**
Pipe 1	8	60	219.1	10.31	2370	P265GH	7850	212.56	0.294	0
Pipe 2	8	80	219.1	13.3	3000	P265GH	7850	210.86	0.285	0

For the excitation and reception of the T(0,1) wave mode, a transducer ring with 40 equally-spaced shear-force transducer elements was installed at one of the ends of the pipe. This positioning allowed for the longest inspection range and avoided the need for directional control. The excitation signal was a 5-cycle Hann-windowed toneburst signal with a central frequency of 50 kHz. The high number of transducer elements around the pipe circumference theo-

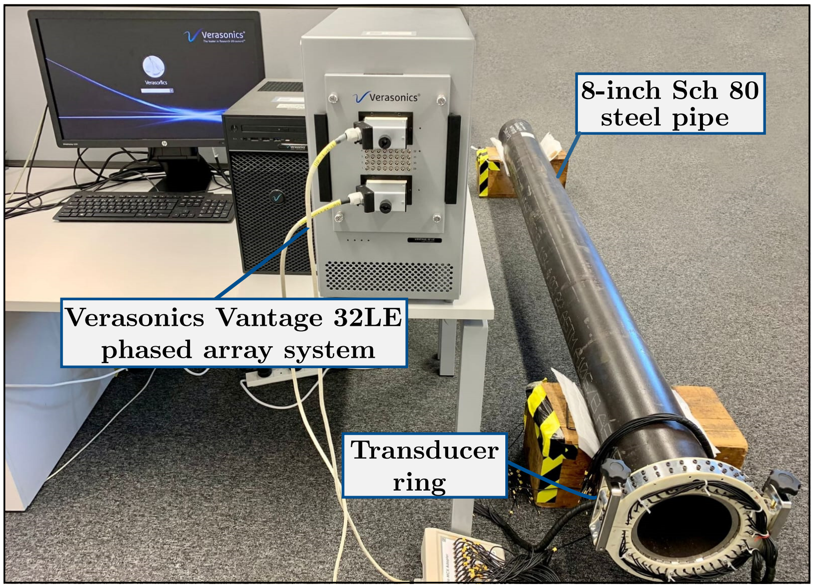

Figure 2.7: Experimental setup for noise collection.

retically ensured the formation of the axial plane wave without grating lobes and the suppression of all flexural modes within the frequency of interest, as shown in the disperse curves in Figure 2.2b. A Verasonics Vantage 32LE phased array measurement system was employed for signal excitation and reception, with a sampling frequency of 2 MHz. To mitigate the influence of random noise, 21 averages were taken in the collection of experimental signals. After averaging 21 times, the signal exhibits a consistent appearance, and the effect of random noise is effectively reduced. The collected experimental signals were filtered using a bandpass filter, with a lower frequency limit of 36 kHz and an upper frequency limit of 64 kHz.

Figure 2.8 presents a representative T(0,1) guided wave signal collected on Pipe 2, depicted on the logarithmic scale and acquired using the CSM data capture arrangement with an extended duration. The transition point between coherent and random noise is identified based on the amplitude profile in Figure 2.8a. Specifically, the coherent region is characterised by a decaying signal envelope, while the random noise region corresponds to the portion

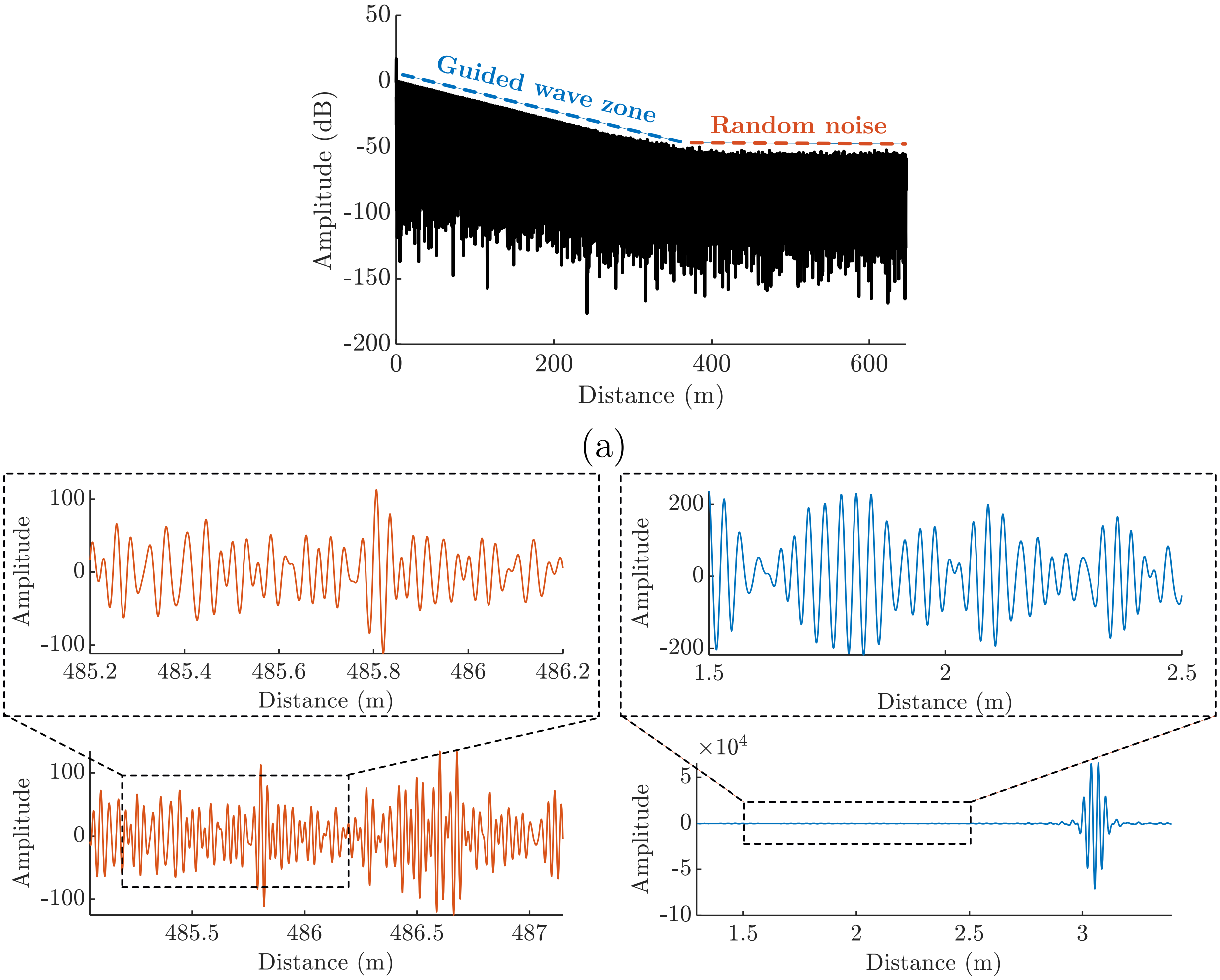

(a)

(b)

(c)

Figure 2.8: (a) A representative T(0,1) guided wave signal measured with an extended duration depicted on the logarithmic scale. (b) Random noise. (c) The signal containing the first T(0,1) wave reflected from the pipe end. The amplitude of signals in (b) and (c) are shown in arbitrary units.

where the signal amplitude stabilises and remains approximately constant. The point at which the decaying trend flattens is considered the transition between coherent and random noise. The random noise signal obtained from the later part is illustrated in Figure 2.8b. The accompanying zoomed-in figure in Figure 2.8b displays the random noise signal within a 1 m travelling range, revealing a stochastic amplitude distribution. It should be noted that the signal in Figure 2.8b was filtered by a bandpass filter, excluding the very low-frequency and very high-frequency components of random noise.

The "Guided wave zone" highlighted in Figure 2.8a captures the initial portion of the signal, which includes multiple echoes of the T(0,1) mode resulting from reflections at the pipe ends due to the short length of the pipe. Figure 2.8c illustrates the portion of the signal containing the first reflection of the T(0,1) wave from the pipe end at 3 metres. Within this zone, any signal component other than the T(0,1) wavepacket reflected from the pipe end is classified as noise, encompassing both coherent and random noise.

2.3.2.2 Coherent noise

This section analyses the characteristics and composition of the coherent noise based on the experimental data collected from Pipe 2, as listed in Table 2.1.

To evaluate the imbalance of transducer performance, Figure 2.9a presents pulse-echo signals from four individual transducer channels, acquired using FMC arrangement. The variations in the wavepackets, as illustrated in the zoomed-in figure in Figure 2.9a, directly correspond to the variations in transducer response. A quantitative analysis of amplitude and phase variations across 40 transducer channels at three distinct frequencies is depicted in Figure 2.9b and Figure 2.9c, respectively. Amplitude and phase exhibit non-uniformity across all transducer channels, while phase variations also demonstrate a dependency on frequency, particularly due to the dispersion of circumferential wave modes.

To analyse the potential excitation of axial guided wave modes due to the transducer performance imbalance, a spatial Fourier transform was applied along the circumferential direction of the pipe, as demonstrated in Figure 2.9b. The resulting amplitude spectrum, indicative of the ability to

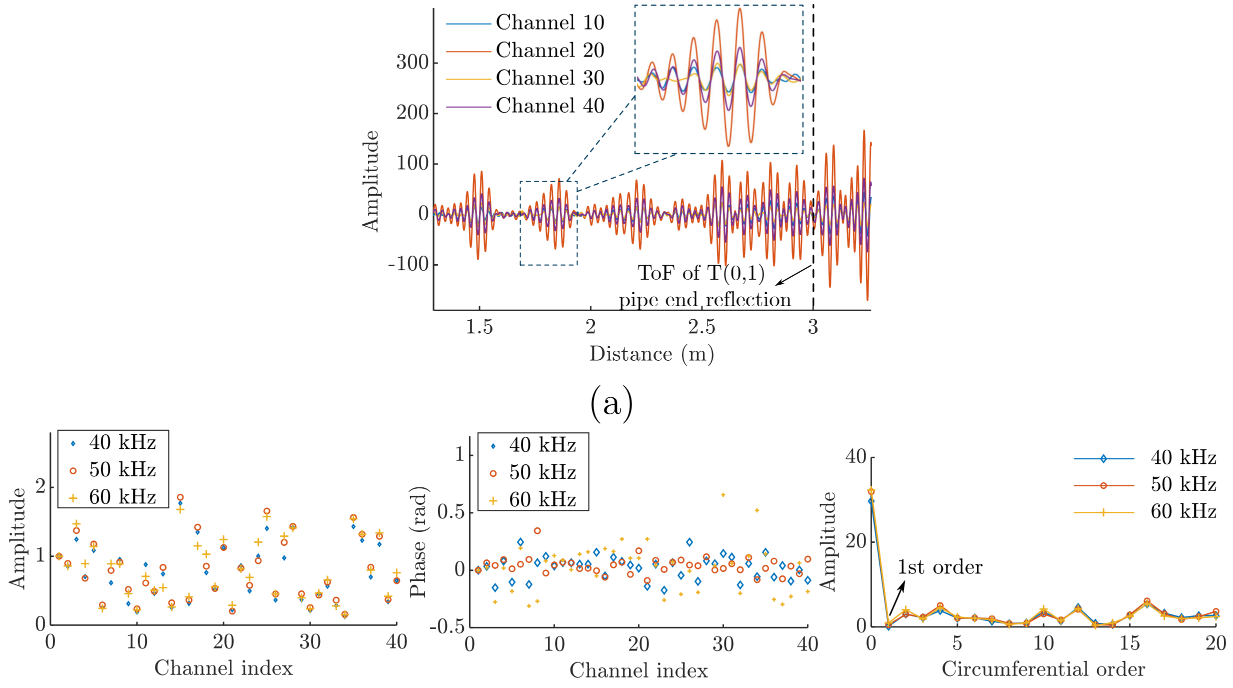

(a)

(b) (c) (d)

Figure 2.9: (a) Pulse-echo signals from four individual transducers when each transducer was individually excited, and quantitative analysis of (b) amplitude and (c) phase variations across 40 transducer channels at three distinct frequencies. (d) Spatial Fourier transforms for analysing the excitation of axial guided wave modes with the transducer performance imbalance.

excite flexural wave modes, is displayed in Figure 2.9d for three different frequencies. Notably, the low amplitude at order 1 in the spectrum suggests that the F(1,m) mode is inadequately excited by this imbalanced transducer performance.

The contribution of circumferential waves and axial flexural waves to coherent noise can be identified by comparing the simulation signals with different boundary conditions. The simulation setup matches that of the experiment. Figure 2.10a shows a simulation of the wavefield generated by a single point source with a shear force applied to the pipe surface in the circumferential direction. Both excitation and reception are positioned at the pipe end,

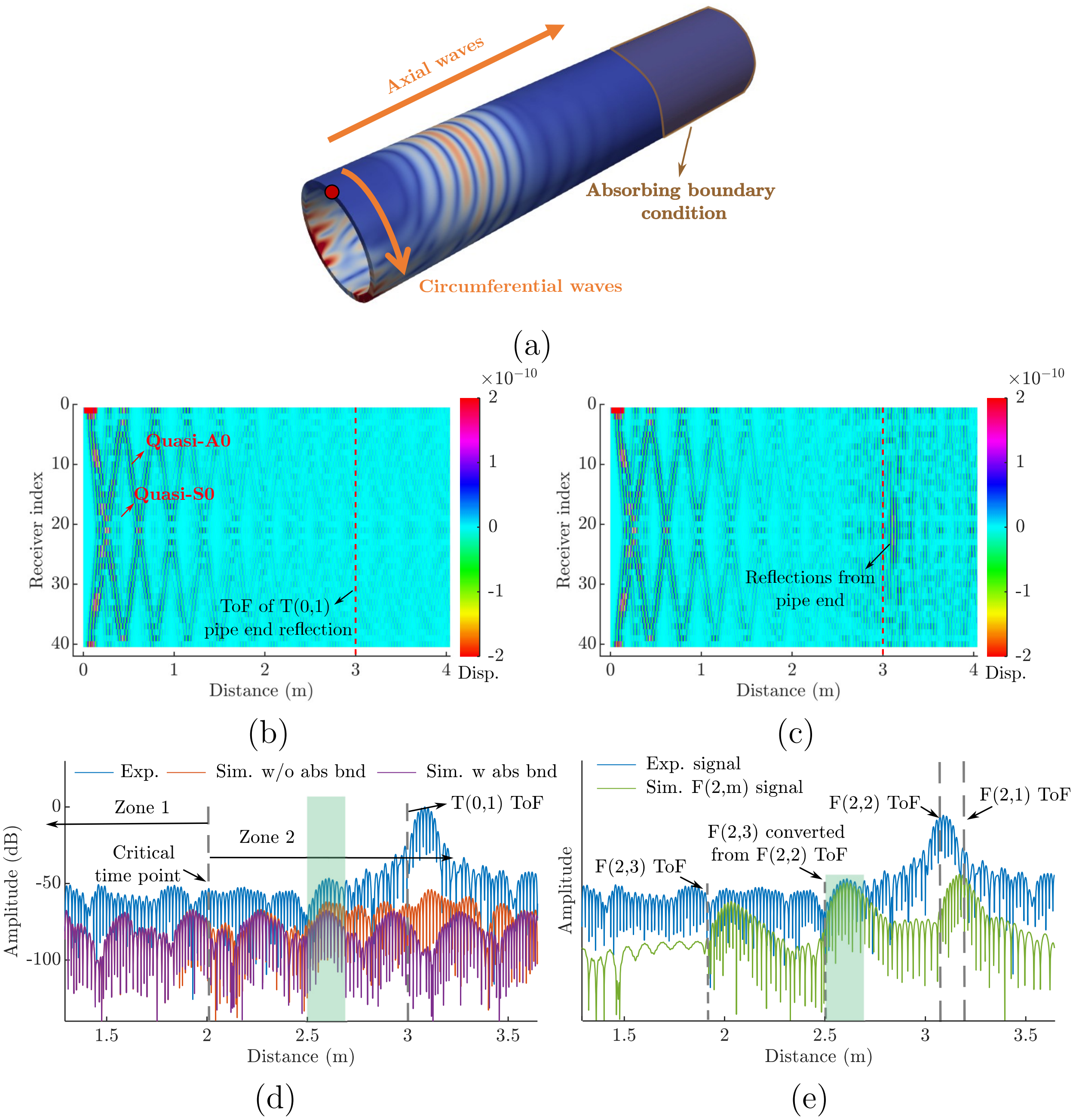

(a)

(b)

(c)

(d)

(e)

Figure 2.10: (a) The wavefield generated by a circumferential shear-force point source applied at the pipe end. (b) Simulated amplitude map of signals from all receivers with transducer No. 1 excited, with an absorbing boundary applied in the simulation. (c) Simulated amplitude map of signals from all receivers with transducer No. 1 excited, without absorbing boundary. (d) Normalised comparison of the simulated signals received at transducer No. 20 with transducer No. 1 excited against the experimental T(0,1) signal with coherent noise. (e) Comparison of the extracted F(2,m) modes with the experimental T(0,1) signal with coherent noise.

matching the experimental setup. The wavefield consists of waves propagating in both the circumferential and axial directions. Figure 2.10b illustrates the amplitude map of signals from all 40 receivers excited by transducer No. 1 with an absorbing boundary applied in the simulation, as depicted in Figure 2.10a. In this case, the signals received by the receivers consist only of circumferential waves, observed as the quasi-S0 mode and the slower quasi-A0 mode with higher amplitude propagating circumferentially. Here, these wave modes are termed “quasi-S0” and “quasi-A0” to differentiate them from the Lamb wave modes typically propagating in flat plates and to account for the edge effects introduced by the pipe end. In contrast, Figure 2.10c presents the amplitude map of signals from all 40 receivers excited by transducer No. 1 without an absorbing boundary. In this scenario, axial waves reflected from the pipe end can be sensed by receivers, including the flexural modes propagating axially.

The simulated time-trace signals received by transducer No. 20 with transducer No. 1 excited, under two different boundary conditions, are compared with the experimental T(0,1) signal in Figure 2.10d on a logarithmic scale. All these signals are normalised to the envelope amplitude of the T(0,1) mode reflected from the pipe end. The comparison reveals the contribution of circumferential waves and axial flexural waves in coherent noise of the experimental T(0,1) signal. Figure 2.10d shows two distinct zones separated by a critical time point: Zone 1, where only circumferential waves are present, and Zone 2, where both circumferential and axial waves are present. The amplitude of circumferential waves diminishes inversely as the square root of the distance from the point source location due to geometric spreading in what is effectively a two-dimensional space. Therefore, the contribution of circumferential waves to the coherent noise decreases with the wave propagation distance due to energy spread.

In Zone 2, a coherent wavepacket is visible within the coherent noise (marked by a green area), which is contributed to by both circumferential waves and axial flexural waves. To identify the flexural wave mode that potentially contributes to this wavepacket, several factors are considered. Firstly, F(1,m) modes are excluded due to their low amplitude in the spatial Fourier analysis, as shown in Figure 2.9d. Additionally, the energy of higher flexural modes like F(3,m) is relatively small compared to the lower-order modes. Consequently, the analysis focuses on F(2,m) modes. In the experiments, shear force was applied to the pipe circumference, which primarily excites shear displacement-dominated wave modes, such as F(1,2), F(2,2), and F(3,2), as shown in Figure 2.2. Given the exclusion of F(1,m) modes and the relatively low energy of F(3,m) modes, it is likely that the wavepacket in Zone 2 is attributed to the F(2,2) mode or a mode converted from F(2,2).

The flexural mode that contributes to this wavepacket can be further identified by comparing the Time of Flight (ToF) of F(2,m) modes with the experimental signal. For calculating the ToF of each wave mode, and considering mode conversion at the pipe end, three-dimensional finite element simulations were employed based on Pipe 2. To selectively excite and extract the F(2,m) mode group, a phase shift corresponding to the second circumferential order was introduced to the signal at both the excitation and reception stages [60]. Figure 2.10e illustrates a comparison of the extracted F(2,m) modes with the experimental T(0,1) signal on a logarithmic scale. A high similarity in the ToF between the F(2,3) wavepacket, converted from the F(2,2) mode, and the marked wavepacket is observed. This indicates that this coherent wavepacket is likely produced by the F(2,3) mode converted from F(2,2) mode and circumferential waves. It is worth noting that the amplitude of the F(2,m) mode in Figure 2.10e is depicted on an arbitrary scale, and the quantitative amplitude of a flexural mode depends on specific installation conditions. The qualitative analysis of this falls beyond the scope of this study.

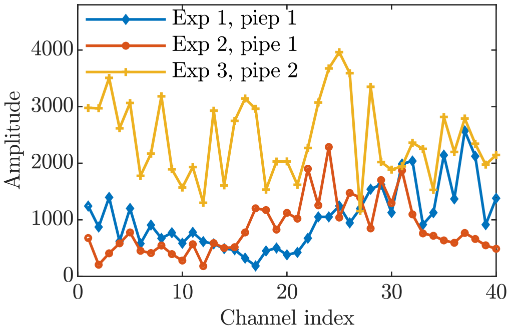

Figure 2.11: The variations in the amplitude of the first T(0,1) pipe end reflections across 40 transducer channels, acquired using CSM arrangement, with different installation conditions. The amplitude is shown in arbitrary units.

Furthermore, to investigate the influence of installation conditions on the imbalance of transducer performance, the transducer ring was detached and reinstalled before data collection to introduce variability to the installation conditions. Figure 2.11 displays the variations in the amplitude of the first T(0,1) pipe end reflections from different transducer channels, acquired using CSM arrangement. The amplitude of the first T(0,1) wavepacket reflected from the pipe end varies among transducer channels and changes with different installation conditions in various experiment sets.

2.3.2.3 Random noise

To determine whether the collected random noise follows a Gaussian distribution, Figure 2.12a presents an analysis of the statistical characteristics of the random noise collected in the laboratory environment, along with the fitting of a reference Gaussian distribution. The shape of the PDF and the skewness and kurtosis values imply that the collected random noise follows a Gaussian distribution.

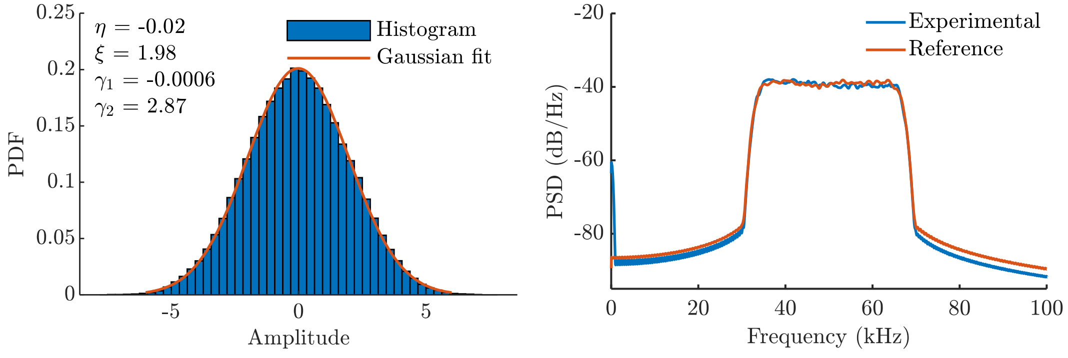

(a) (b)

Figure 2.12: Statistical analysis of the random noise. (a) PDF of the random noise alongside the fitting of a reference Gaussian distribution, where η is the mean value, ξ is the standard deviation, γ_1 and γ_2 are skewness and kurtosis, respectively. (b) PSD of the filtered random noise signal compared to that of a reference Gaussian white noise with a similar power level.

For a deeper examination of whether the random noise maintains its white noise characteristics after being subjected to a bandpass filter, the PSD of the filtered random noise signal was computed and compared to that of a reference Gaussian white noise with a similar power level, as shown in Figure 2.12b. Both the recorded noise and the reference Gaussian white noise were passed through the same bandpass filter. The PSD comparison reveals that the spectrum of the recorded noise remains nearly constant within the frequency range of interest, which is a key characteristic of white noise. This finding confirms that the recorded noise maintains its white power spectrum even after being subjected to the bandpass filter.

To investigate the channel dependency of random noise, Figure 2.13 compares the RMS amplitude spectrum of random noise signals from 40 transducer channels under three different installation conditions. The RMS amplitude of random noise varies across transducer channels. Unlike the amplitude fluctuations observed in the first T(0,1) pipe end reflections (Figure 2.11), a broadly similar channel-wise pattern in RMS amplitude is observed across the

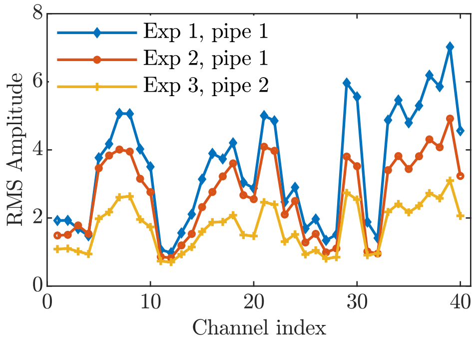

Figure 2.13: The variations in the RMS amplitude of random noise signals across 40 transducer channels, acquired using CSM arrangement, with different installation conditions. The amplitude is shown in arbitrary units.

three experiments, despite differing transducer installation conditions. This observation suggests a degree of channel-dependent behaviour in the random noise level that appears relatively unaffected by changes in installation setup.

2.4 Summary

This chapter covers fundamental concepts of wave propagation in a pipe, including axial and circumferential guided waves. Three types of axial guided waves exist and their properties have been investigated through dispersion curves. The T(0,1) mode is emphasised, highlighting its advantages in guided wave testing over other modes, the excitation of a pure T(0,1) wave mode, and factors introducing coherent noise during the excitation of the T(0,1) mode. Furthermore, an analogy between circumferential guided waves in pipes and plates is examined.

A noise analysis methodology is then presented, covering coherent and random noise, based on experimental data collection. It involves initial estimation of pipe conditions, noise collection, and subsequent analysis of coherent and random noise. The proposed method is demonstrated based on the laboratory experiments. Coherent noise is analysed by examining the imbalance of transducer performance, considering variations in both amplitude and phase. Furthermore, the contribution of flexural waves and circumferential waves to coherent noise is evaluated through mode analysis. Additionally, it is observed that random noise can be effectively modelled using a Gaussian white noise model with limited bandwidth. This analysis provides valuable insights into guided wave signal noise, laying the foundation for noise modelling in the following sections.

Chapter 3

Generation of realistic guided wave signals

Most of the material presented in this chapter is based on findings detailed in publication [P1].

3.1 Introduction

Chapter 2 introduces a method to analyse noise features in real guided wave signals and provides a comprehensive understanding of the statistical characteristics of random noise and the formation and composition of coherent noise. In this chapter, a method to generate realistic guided wave signals incorporating both random and coherent noise is presented, and potential applications are discussed later.

Generating synthetic signals continues to be crucial in various NDE and SHM scenarios, such as facilitating the development of defect characterisation methods, providing iterative model data for model-based damage imag-

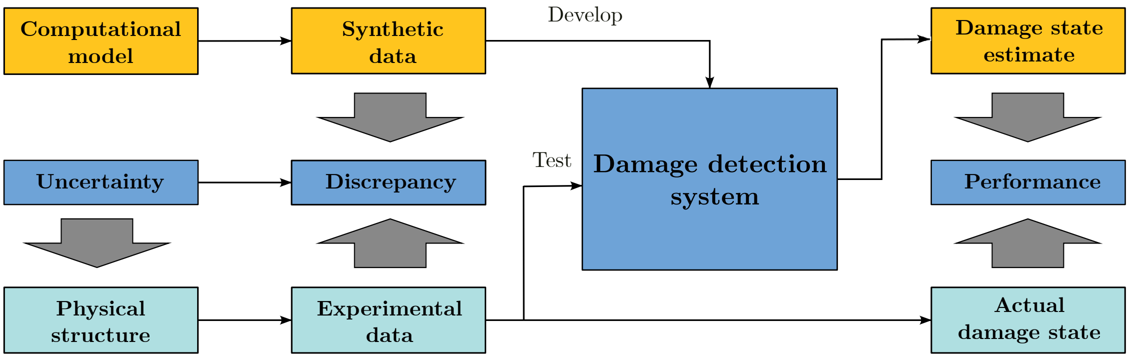

Figure 3.1: A general procedure for estimating the damage state of a physical structure using a damage detection system developed based on synthetic data.

ing techniques like full waveform imaging [61], creating datasets for training machine learning models for damage detection [62], obtaining inspection databases for training NDE operators and technicians [63, 64], and generating datasets containing damage signatures for model-based POD analysis [65].

Figure 3.1 illustrates a general procedure for estimating the damage state of a physical structure using a damage detection system developed with synthetic data. Initially, synthetic data is generated from an idealised computational FE model, which can then be used to develop a damage detection model; for example, training a machine learning model for this purpose. After the training phase, this machine learning model processes experimental data acquired from sensors monitoring the actual physical structure to predict the extent of damage. It is important to note that the real-world physical structure includes inherent uncertainties not captured by the computational model, potentially leading to discrepancies between the synthetic and experimental data. These discrepancies underscore the challenges that the damage detection system faces in addressing the inherent uncertainties present in the experimental data, which could compromise the accuracy of the damage state estimations. The effectiveness of the damage detection system depends on the fidelity of the synthetic data, that is, its resemblance to the experimental data. The extent to which the damage state estimations reflect the actual state of the structure is indicative of the system's performance. While the specifics of the flowchart may differ across various applications depending on the role of synthetic data in the procedure, the fidelity of the synthetic data remains critical in all cases.

However, synthetic data, typically generated by theoretical models or numerical simulations, rarely match real experimental signals with the accuracy needed [66–70]. This discrepancy arises from various uncertainties [71], such as temperature, humidity, and random noise in the context of guided wave testing. The unavoidable discrepancy between experimental and synthetic data may limit system performance [72], especially when the measurement system is subject to significant measurement uncertainty.

To mitigate the impact of uncertainty on system performance, different strategies can be employed, which generally fall into two categories. As shown in the flowchart in Figure 3.1, the performance of the developed system can be improved either by enhancing the robustness of the system to uncertainty or by reducing the discrepancy between the synthetic data and the experimental data. The following discussion briefly outlines selected studies from each category of strategies, highlighting the advantages and drawbacks of each family of techniques.

The robustness of the developed system to these uncertainties can be improved by quantifying the uncertainties and accounting for them in the developed system based on advanced signal processing [73–75], statistical methods [76, 77], or machine learning methods [78, 79]. This category of methods has a wider application in damage detection.

Advanced signal processing techniques can enhance system robustness by improving the SNR of experimental signals or reducing their complexity. For example, Hall et al. [80] introduced an adaptive parameter compensation method to mitigate the sensitivity of phase information to environmental fluctuations in ultrasonic imaging. By estimating transducer transfer functions and dispersion relations, the method compensates for experimental guided wave signals, enhancing imaging capabilities. Despite their efficacy, these signal processing strategies demand precise parameter estimation and robust implementation to effectively address uncertainty in guided wave applications, particularly within complex structures. Concurrently, feature extraction methods, such as the one developed by Liu et al. using Singular Value Decomposition (SVD), isolate damage-sensitive features that are insensitive to uncertainty, thereby increasing the system's robustness [81].

In the face of measured structural responses exhibiting stochastic variations due to environmental and operational uncertainties, statistical methods are gaining increasing interest to achieve more robust damage detection and quantification with confidence bounds. Amer et al. [82] proposed a Non-Parametric Time Series (NP-TS) based statistical framework to manage uncertainty within guided wave monitoring. Utilising stochastic NP-TS representations like the Welch PSD estimate, and its statistical attributes (mean, variance, etc.), this framework improves damage detection sensitivity and robustness compared to conventional damage indices. Nevertheless, the application of statistical methods introduces additional complexities such as the need for selecting appropriate statistical distributions and estimators.

More recently, machine learning-based methods have emerged as a popular approach to tackling measurement uncertainty related to guided wave monitoring. Harley et al. have employed a series of machine learning-based methods to tackle varying Environmental and Operational Conditions (EOCs), mainly temperature variations, in guided wave testing/monitoring, including dictionary learning [83], deep learning [56], ensemble learning [62], Principal Component Analysis (PCA) [84], and Variational Autoencoder (VAE) [85]. While machine learning shows promise in improving the robustness of damage detection systems, it is typically tailored to specific structures and conditions. Generalised robustness across varied guided wave setups, materials, and damage types remains a challenge, necessitating additional validation.

Another family of strategies to ensure the system's performance is to bridge the gap between synthetic signals and real experimental signals through generating realistic signals. These signals aim to capture key uncertainties observed in real measurements, such as signal variability, noise, and measurement artifacts, which are often missing in idealised simulations. By incorporating these real-world characteristics, the synthetic data used for system development becomes more representative of the actual conditions encountered in practice. As illustrated in Figure 3.1, a damage detection system (e.g., a machine learning model for damage detection) developed using more realistic synthetic signals is better equipped to handle uncertainties in experimental data, thereby improving its generalisation and robustness during real-world inspections. Generating realistic guided wave signals is attracting increasing attention due to its straightforward implementation, broad applicability, and adaptability across different applications. The main approaches for generating realistic signals can be categorised into three groups: machine learning-based methods, superposition-based methods, and physics-based FE simulations. Each of these methodologies will be discussed in this chapter.

Machine learning, beyond its potential for damage detection, is becoming pivotal in the realm of signal generation. The VAE and the Generative Adversarial Network (GAN) are the foremost machine learning techniques employed for this purpose. Loveday et al. [86,87] developed a VAE-based model to generate guided wave signals that contain different modes and damage features for railway testing under uncertainty. Despite the increased complexity and realism of the synthetic signals generated by this model, its fidelity is constrained by the fact that it was trained on ideal simulation signals. Moreover, its reliance on encoding and decoding processes may impede its ability to capture unique signal features, such as noise and anomalies present in real guided wave signals.

GAN models, in contrast to VAEs, exhibit greater diversity and robustness in signal generation, especially in the presence of noise or anomalies [88, 89]. Heesch et al. [90] trained a StyleGAN-based model that produced guided wave signals closely resembling experimental data, incorporating inherent noise without necessitating physics-based considerations. Nevertheless, GAN-generated signals often lack explainability and do not provide insights into the physics of guided wave propagation or the characteristics of the measurement system. Additionally, GAN models are difficult to train [91], with their performance heavily dependent on the machine learning architecture and hyperparameter tuning. The requirement for extensive training data, which is not always readily available or might be costly to obtain, poses another significant challenge.

An alternative approach for generating realistic signals that account for measurement uncertainty is data superposition. This method involves layering noise-free damage signatures, derived from FE models or analytical wave scattering models, onto experimental data collected from undamaged samples. This technique has proven effective in applications like generating realistic ultrasonic phased array imaging with coherent noise [92]. For the generation of guided wave signals under uncertainty, as mentioned in Chapter 1, Liu et al. [35] proposed superposing data collected under varying environmental conditions from an undamaged structure with artificial damage signals. While promising, the superposition method faces limitations in complex scenarios, such as those involving multiple reflections and interactions with structural features.

To tackle the complexities of guided wave testing, physics-based FE methods are highly valued for their adaptability. Currently, most FE models perform well in simulating the physics of wave propagation but lack an incorporation of measurement uncertainty, leading to a lack of realism in the synthetic signals. To improve the fidelity of synthetic data, Gaussian white noise is commonly added to simulation data to generate noisy data [56]. However, experimental signals contain both random and coherent noise, the latter arising from imperfect excitation conditions, as discussed in Chapter 2. In real scenarios, the main challenge in realistic simulation is the accurate depiction of the measurement conditions, such as sensor adhesion and electronic device characteristics, which primarily affect the transducer performance and noise characteristics of guided wave signals rather than the wave propagation physics itself. Furthermore, additional factors can also contribute to signal changes, such as temperature variations. This makes realistic signal generation even more challenging due to the lack of input data information for a specific measurement system.

As highlighted in Chapter 2, coherent noise in guided wave signals can be attributed to transducer performance imbalances. Mariani's work demonstrated that variations in excitation signal amplitude, indicative of transducer imbalances, could produce guided wave signals with coherent noise [55]. However, phase variations also exist alongside amplitude variations due to inherent transducer imbalances [93], and they are also influenced by varying environmental conditions. Therefore, a more realistic way to incorporate transducer performance in simulation models is needed.

The performance of a transducer is determined by its properties, such as electrical impedance and sensitivity, which can be obtained through a series of electrical calibration measurements [94]. However, this process is laborious and requires specialised equipment. Moreover, these measurements typically do not account for external EOCs, such as transducer installation conditions and ambient temperatures, which especially affect ultrasonic transducer performance in long-term SHM applications. Research suggests that transfer function-based characterisation methods are more effective for profiling ultrasonic transducer performance [95], making it potentially applicable to be integrated into simulation models to produce more realistic guided wave signals.

Therefore, this chapter presents an efficient and accurate numerical framework designed to generate realistic guided wave signals, tailored specifically for reliability estimation in guided wave SHM systems for pipeline monitoring. The proposed methodology captures key signal characteristics, including random and coherent noise, associated with transducer performance imbalances. The success of this approach is validated through comparing the synthetic signals with individual experimental traces as well as performing statistical comparisons. In addition, realistic synthetic signals are used to quantify the inspection range of a guided wave SHM system through location-dependent POD analysis, providing a quantitative and confidence-based evaluation of detection capability, in contrast to conventional methods based on subjective interpretation of noise levels. Furthermore, it explores how precise transducer performance estimation can aid in reducing coherent noise in experimental signals, with subsequent sections detailing coherent noise reduction by compensating for transducer performance imbalances.

3.2 Generic scheme

In this section, a numerical framework developed for generating synthetic realistic guided wave signals is introduced, which relies on a finite amount of experimental data representative of real measurement conditions. The schematic diagram of the proposed methodology is illustrated in Figure 3.2. To faithfully capture experimental signals, the proposed framework incorporates both coherent noise and random noise into the simulation.

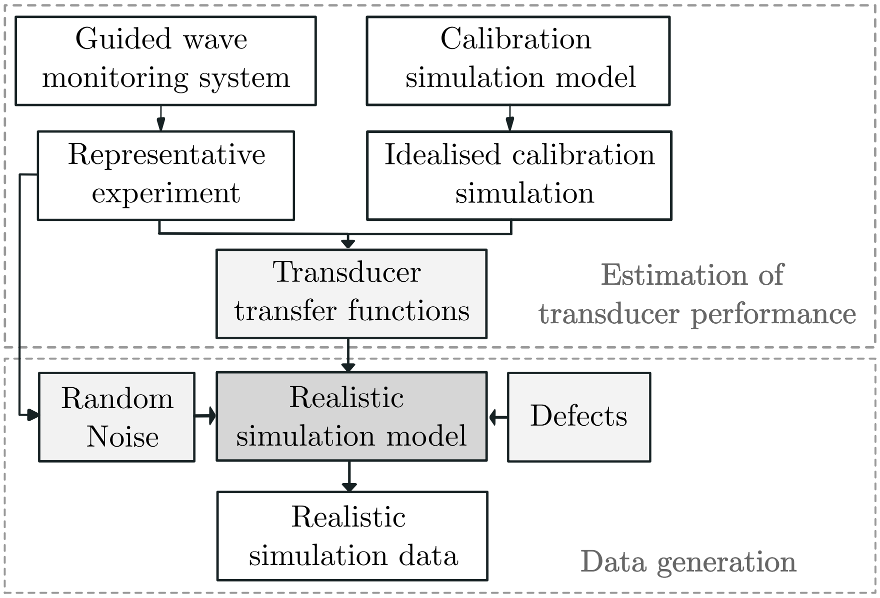

Figure 3.2: Schematic of the proposed framework for generating realistic guided wave signals through FE simulation.

In the proposed framework, simulations are conducted in two key phases: the idealised calibration simulation and the realistic simulation. In the idealised calibration simulation, all transducers are assumed to have uniform performance. A CSM dataset is obtained by applying the identical excitation signals to all transmitter nodes and the T(0,1) signal is obtained by summing the CSM signals from the reception side. In the realistic simulation model, both coherent noise and random noise are incorporated to generate realistic guided wave signals. For coherent noise consideration, transducer transfer functions are estimated and applied in the simulation on both the excitation and reception sides. Subsequently, random noise is added to the signals from each transducer channel. A realistic T(0,1) signal is obtained by summing the signals from all transducer channels.

The incorporation of random noise involves a statistical analysis of the noise collected in the representative experiments, which is specific to the ambient environments and measurement system employed. In this study, random noise is modelled using Gaussian white noise with a limited bandwidth, as described in Section 2.3. The RMS level of the random noise across transducer channels follows the distribution described in Figure 2.13.

To model coherent noise, transducer transfer functions are estimated based on a comparison between the representative experimental signal and the idealised calibration simulation signal in the frequency domain. The transducer transfer function obtained in this manner has shown good agreement with the transfer function obtained by characterising all electrical and electromechanical components within the measurement system in the literature [95, 96]. The implementation of these transfer functions enables the capture of the transducer performance across the entire frequency range of interest, which is necessary for the representation of coherent noise, as discussed in Section 2.3. This section will illustrate the methodology for estimating the transducer transfer functions in detail.

Without considering the effect of transducer performance, the signal emitted from transducer i and received by transducer j is denoted as S_{ij}, and represents the physical wave propagation in both the circumferential and axial directions, as illustrated in Figure 2.10a. The T(0,1) signal, S_{T01}, is obtained by summing the signals from all transducer pairs, is given by

$$S_{\mathrm{T01}}=\sum_{i=1}^{N}\sum_{j=1}^{N}S_{ij}, \tag{3.1}$$

where N represents the number of transducer elements. In an ideal measurement scenario, N transducers equally spaced around the pipe circumference are excited with identical signals. The circumferential waves are suppressed through destructive interference, resulting in the formation of a clear T(0,1) plane wave propagating axially. Simultaneously, the enforced identical displacement around the pipe circumference induced by N transducers suppresses all flexural modes with a circumferential order lower than N, leaving only the T(0,1) wave mode propagating along the pipe axis within the frequency range of interest. In practical situations, both coherent noise and random noise exist in the T(0,1) signal, which can be described as

$$S'_{\mathrm{T01}}=\sum_{i=1}^{N}\sum_{j=1}^{N}S'_{ij}, \tag{3.2}$$

where S'_{ij} represents the signal S_{ij} contaminated by random noise and affected by transducer performance. The transducer performance can be represented as transducer transfer functions, T_{Ti} and T_{Rj}, on the excitation and reception sides, respectively, within the frequency range of interest. Hence, S'_{ij} can be expressed as

$$S'_{ij}=T_{Ti}\cdot T_{Rj}\cdot S_{ij}+S'_{\mathrm{N}ij}, \tag{3.3}$$

where $S'_{\mathrm{N}ij}$ represents the random noise signal in the signal S'_{ij} and $\cdot$ donates multiplication in the frequency domain, corresponding to convolution in the time domain. By substituting Eq. (3.3) to Eq. (3.2), Eq. (3.2) is transformed to

$$S'_{\mathrm{T01}} = \sum_{i=1}^{N}\sum_{j=1}^{N}(T_{Ti} \cdot T_{Rj} \cdot S_{ij} + S'_{\mathrm{N}ij}). \tag{3.4}$$

In Eq. (3.4), S_{ij}, representing the physical wave propagation, can be accurately captured in an idealised calibration simulation. The transducer transfer functions T_{Ti} and T_{Rj} can be estimated based on the T(0,1) wavepacket reflected from the known features, such as welds, collected in the representative experiment.

When data is captured with the CSM arrangement, Eq. (3.4) can be alternatively expressed as

$$S'_{\mathrm{T01}} = \sum_{j=1}^{N}(T_{Rj} \cdot \sum_{i=1}^{N}(T_{Ti} \cdot S_{ij}) + S'_{\mathrm{N}j}), \tag{3.5}$$

where $S'_{\mathrm{N}j}$ represents the random noise signal. The signal available from transducer j in an experimental measurement is denoted as

$$S'_j = T_{Rj} \cdot \sum_{i=1}^{N}(T_{Ti} \cdot S_{ij}) + S'_{\mathrm{N}j}. \tag{3.6}$$

The plane wave formed by the common source excitation is assumed to be minimally affected by the performance imbalance of transducers on the excitation side due to wave superposition. The plane wave consists of both T(0,1) and other unwanted flexural modes resulting from the imbalance of transducer performance. For cases where the functional transducer ring is properly installed under the guided wave monitoring guidelines, the amplitude of the unwanted flexural modes mixed in the T(0,1) wavepacket used is negligible compared to the amplitude of the T(0,1) wavepacket, due to the limited transducer performance variations and the dispersive nature of flexural wave modes. It allows for the assumption that variations on the excitation side can be omitted, resulting in

$$S'_j \approx T_{Rj} \cdot \sum_{i=1}^{N} S_{ij} + S'_{\mathrm{N}j}. \tag{3.7}$$

Hence, the one-side transfer function of transducer j can be estimated as

$$T_{Rj} \approx \frac{S'_j}{S_j}, \tag{3.8}$$

when the random noise $S'_{\mathrm{N}j}$ is negligible, where $S_j = \sum_{i=1}^{N} S_{ij}$ is the receiving signal from transducer j in the calibration simulation.

Therefore, the transducer transfer functions can be estimated by Eq. (3.8) based on the comparison of the idealised calibration simulation signal and the representative experimental signal. It is important to note that the direct division in Eq. (3.8) is unstable due to the inherent presence of random noise. To address this, a Wiener filter can be implemented to stabilise the estimation of transducer transfer functions [97]. Eq. (3.8) can be reformulated as

$$T_{Rj} \approx \frac{S_j^* \cdot S'_j}{|S_j|^2 + \vartheta}, \tag{3.9}$$

where $*$ denotes the complex conjugate and ϑ represents the stabilisation factor, which is determined based on the noise level of the signal S'_j and can be estimated by

$$\vartheta = Q|S_j|^2_{max}. \tag{3.10}$$

Here, the parameter Q is determined empirically according to the noise level of the signal S'_j. A smaller Q value may result in inadequate noise suppression, whereas a larger value can lead to a higher error in the estimation of transducer transfer functions [98]. In this study, Q has been set to be 0.0005 through a trial-and-error procedure. In this procedure, the evaluation of the parameter Q is conducted in the frequency domain, ensuring that the spectral content within the main lobe around the central frequency is preserved with high fidelity and preventing any disruption in the side lobe frequency range that could arise from inadequate stabilisation.

3.3 Numerical validation

3.3.1 Simulation setup

All simulations in this study were performed using Pogo, an FE solver developed at Imperial College London [30]. Three-dimensional FE models were constructed based on the specific pipes employed in the experiments, as detailed in Table 2.1. In the simulation, the transducer ring was positioned at the end of the pipe, with 40 equally spaced source nodes representing 40 transducer elements for guided wave excitation and reception. This is considered a reasonable approximation because the actual contact area between each flat transducer element and the curved pipe surface forms a narrow line contact, which is small compared to the wavelength of the T(0,1) mode, approximately 60 mm at 50 kHz in this study.

Aligned with the experimental setup, a 5-cycle Hann-windowed toneburst with a central frequency of 50 kHz was used as the excitation signal in the simulation, characterised by a T(0,1) wavelength of approximately 60 mm. This signal was assigned to the aforementioned source nodes. To ensure a precise simulation of wave propagation, a structured mesh with an element size of 1 mm, comprising roughly 60 elements per wavelength, was implemented, with a corresponding time step of approximately 1×10^{-7} s. This level of mesh refinement was selected to ensure sufficient convergence of the solution and has been previously used in similar FE modelling studies [99]. The total simulation duration was 10 ms, capturing the first six T(0,1) reflections from the pipe end. The chosen element type was a general-purpose linear brick element with reduced integration (C3D8R). For a typical simulation of Pipe 1, the number of nodes was 16,691,840, requiring 6.7 GB of memory and approximately 7 minutes for a 10 ms wave propagation simulation on three NVIDIA GeForce RTX 2080 Ti GPUs.

3.3.2 Simulation results

To validate the methodology proposed in this study for the estimation of transducer transfer functions, a set of reference simulation signals with coherent noise was generated based on Pipe 1, using the same excitation configuration as in the experiment. These signals were then stored for comparison as the ground truth, serving as the virtual experimental data within the framework illustrated in Figure 3.2. The process described in Section 3.2 was applied to estimate transducer transfer functions. Notably, random noise was excluded in this section, with specific emphasis placed on coherent noise.

For the generation of virtual experimental signals, different phase shifts, amplitude variations, and varying passbands were applied to both the excitation and reception sides, as depicted in Figure 3.3a to Figure 3.3c. The resulting virtual experimental T(0,1) signal is presented in Figure 3.3d with coherent noise present.

The one-side transfer function of transducer i was estimated using Eq. (3.9) based on the receiving signal S_i' from transducer i with the CSM data capture arrangement. Figure 3.4 illustrates the virtual experimental signal acquired from transducer No. 1, S_1', when all transducers were excited simultaneously. The T(0,1) wavepacket reflected from the pipe end was windowed out using a Tukey window for the estimation of the transducer transfer function.

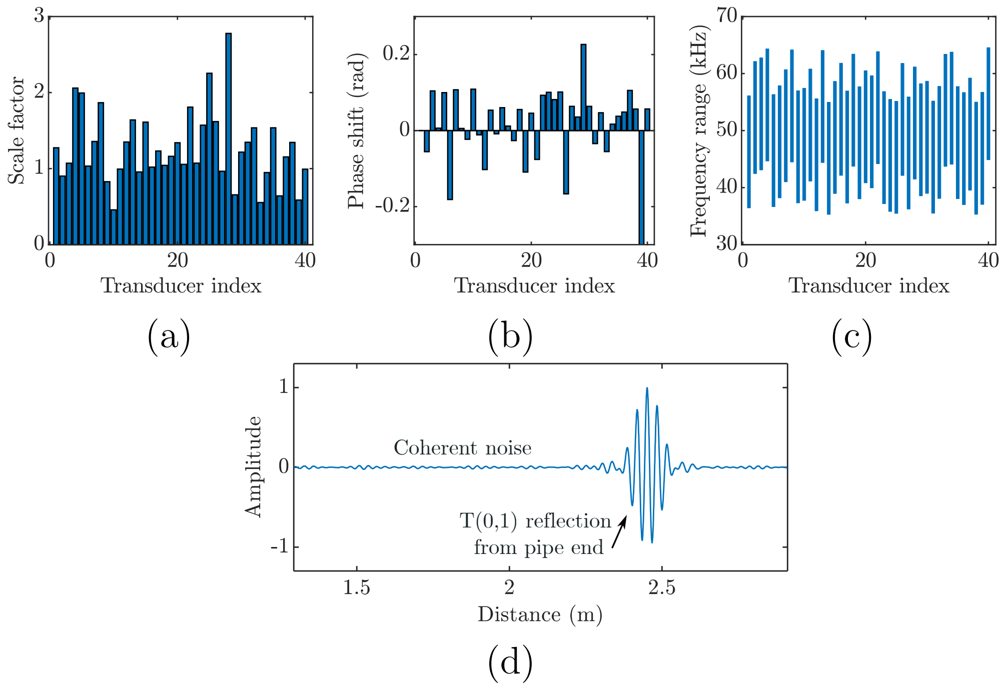

(a) (b) (c)

(d)

Figure 3.3: Distribution of (a) phase shifts, (b) amplitude variations, and (c) bandwidths across transducer channels applied in the reference simulation. (d) Virtual experimental T(0,1) signal with coherent noise generated in the reference simulation.

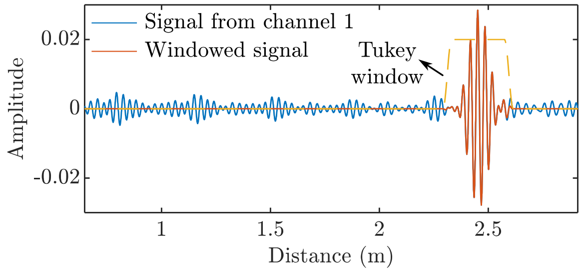

Figure 3.4: Virtual experimental signal S'_1 (shown in orange) acquired from transducer No. 1 used for estimating transducer transfer functions, which were windowed from the original signals (shown in blue) with a Tukey window indicated by the yellow dotted line.

The synthetic T(0,1) signal with coherent noise is compared with the virtual experimental T(0,1) signal in Figure 3.5a. The synthetic T(0,1) signal shows a similar coherent noise level as that in the virtual experimental T(0,1) signal

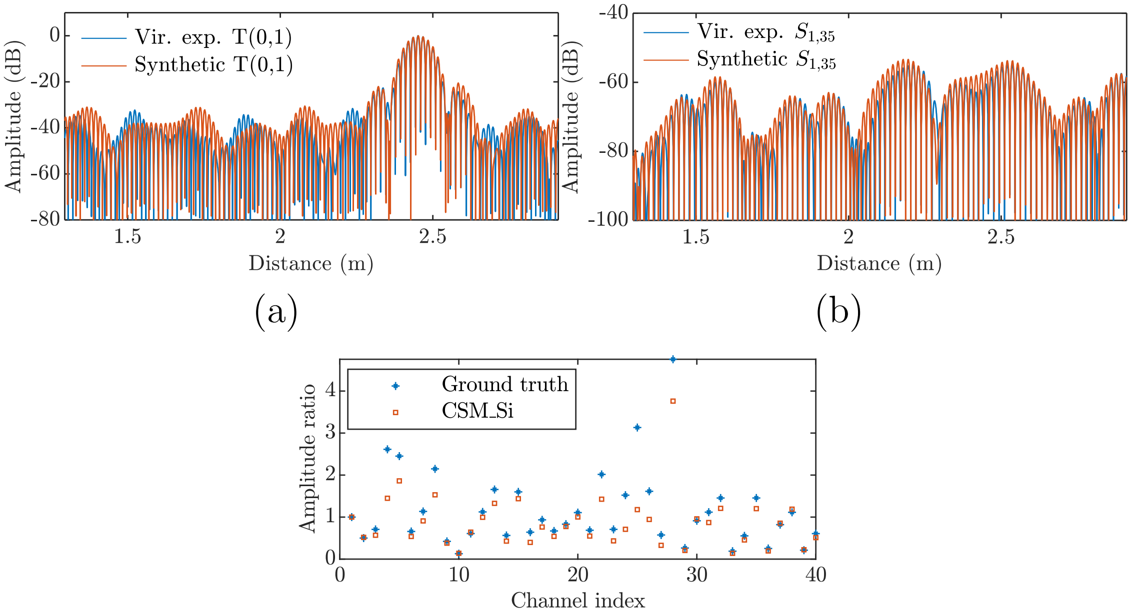

(a) (b)

(c)

Figure 3.5: (a) Comparison of the synthetic T(0,1) signal with the virtual experimental T(0,1) signal on the logarithmic scale. (b) Comparisons between the synthetic pitch-catch signal emitted from transducer No. 1 and received by transducer No. 35, with the corresponding virtual experimental signal $S'_{1,35}$. (c) Comparisons between the estimated amplitude variations at the central frequency with the ground truth of amplitude variations applied in the reference simulation.

but with some discrepancies in the waveform. Furthermore, Figure 3.5b shows the synthetic pitch-catch signal emitted from transducer No. 1 and received by transducer No. 35, which is overestimated compared to the corresponding virtual experimental signal $S'_{1,35}$. The discrepancy in the synthetic signal and the virtual experimental signal is due to the approximation in the estimation of transducer transfer functions made in Eq. (3.7).

Figure 3.5c compares the estimated amplitude variations at the central frequency, 50 kHz, with the ground truth of amplitude variations applied in the reference simulation. The estimation generally shows good agreement with the ground truth but exhibits a larger deviation when the variations in transducer response become too large, thereby violating the assumption in Eq. (3.7).

3.4 Experimental validation

In this section, the proposed methodology is evaluated based on experimental signals collected from Pipe 2. As mentioned in Section 2.3.2, the experimental signals were obtained with 21 averages to suppress random noise, focusing on the effects of coherent noise.

3.4.1 Experimental results

3.4.1.1 Individual T(0,1) signal comparison

Figure 3.6a displays the synthetic T(0,1) signal generated based on the estimated transducer transfer functions, along with the corresponding experimental signal. The experimental signals were digitised using a 14-bit analog-to-digital converter, providing an approximate dynamic range of 84 dB, which ensures sufficient resolution to accurately capture both low-level noise and the guided wave signals. A comparison between the synthetic and experimental signals reveals good agreement in both the coherent noise level and the waveform of the T(0,1) wavepacket reflected from the pipe end. The frequency spectrum comparison in Figure 3.6b highlights the similarity between the synthetic signal and the experimental T(0,1) signal, displaying an overall smooth shape with minor distortions attributed to the presence of coherent noise.

3.4.1.2 Error analysis

Similarly to the comparison in the simulation validation shown in Figure 3.5a, the comparison between the synthetic T(0,1) signal and the experimental sig-

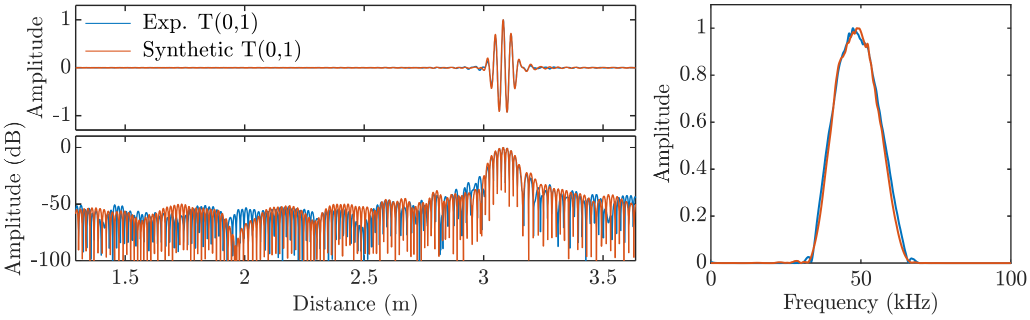

(a) (b)

Figure 3.6: Comparison between the synthetic T(0,1) signals and the corresponding T(0,1) experimental signals in (a) the time domain and (b) the frequency domain.

nal in Figure 3.6a presents a discrepancy in the waveform of coherent noise. One possible reason for this discrepancy is the error in estimating transducer transfer functions. Assumptions were made about random noise and the variations in transducer responses in Eq. (3.9) for the estimation of transducer transfer functions. These assumptions may be violated for certain transducer channels where random noise or transducer response variations are more pronounced. In the experiments, additional error sources may be present due to imperfections in the real world. For instance, variations in pipe wall thickness [100] and material anisotropy resulting from the manufacturing process [101] can contribute to these errors. The manufacturing of seamless pipes typically involves processes such as extrusion and hot finishing, which inevitably introduce changes in the material microstructure, leading to anisotropy, particularly in the axial and circumferential directions [102]. These imperfections introduce extra errors in the idealised calibration simulation signal S_j presented in Eq. (3.9).

3.4.1.3 Statistical T(0,1) signal comparison

In this section, a statistical analysis is conducted to quantitatively evaluate the effectiveness of the proposed framework in accurately capturing coherent noise. Experimental data with various transducer performance variations, hence exhibiting different coherent noise levels, were collected based on a full-matrix dataset obtained by exciting individual transmitters sequentially. Specifically, a varying number of transducer channels were randomly selected and disabled, and the corresponding signals in the full-matrix dataset related to these channels were suppressed. Generally, an increase in the number of disabled transducer channels results in a higher coherent noise level in the experimental signal. Subsequently, the modified full-matrix dataset was summed on the excitation side to acquire the CSM data, which was then used to estimate transducer transfer functions according to the method detailed in Section 3.2.

Figure 3.7 compares the synthetic T(0,1) signals with the experimental T(0,1) signals, showcasing diverse coherent noise levels. The disabled transducer channels are highlighted in red in the corresponding figures on the right side. Overall, a good agreement is observed in the coherent noise level. For a quantitative evaluation, the coherent noise level of a T(0,1) signal was calculated using SNR, defined as:

$$\mathrm{SNR} = 20\log_{10}\left(\frac{\mathrm{RMS}_{\mathrm{CoherentNoise}}}{\mathrm{AMP}_{\mathrm{T(0,1)}}}\right), \tag{3.11}$$

where $\mathrm{RMS}_{\mathrm{CoherentNoise}}$ represents the RMS value of coherent noise, and $\mathrm{AMP}_{\mathrm{T(0,1)}}$ denotes the amplitude of the T(0,1) wavepacket reflected from the pipe end.

Figure 3.8 displays a scatter plot of the SNR values of the synthetic T(0,1)

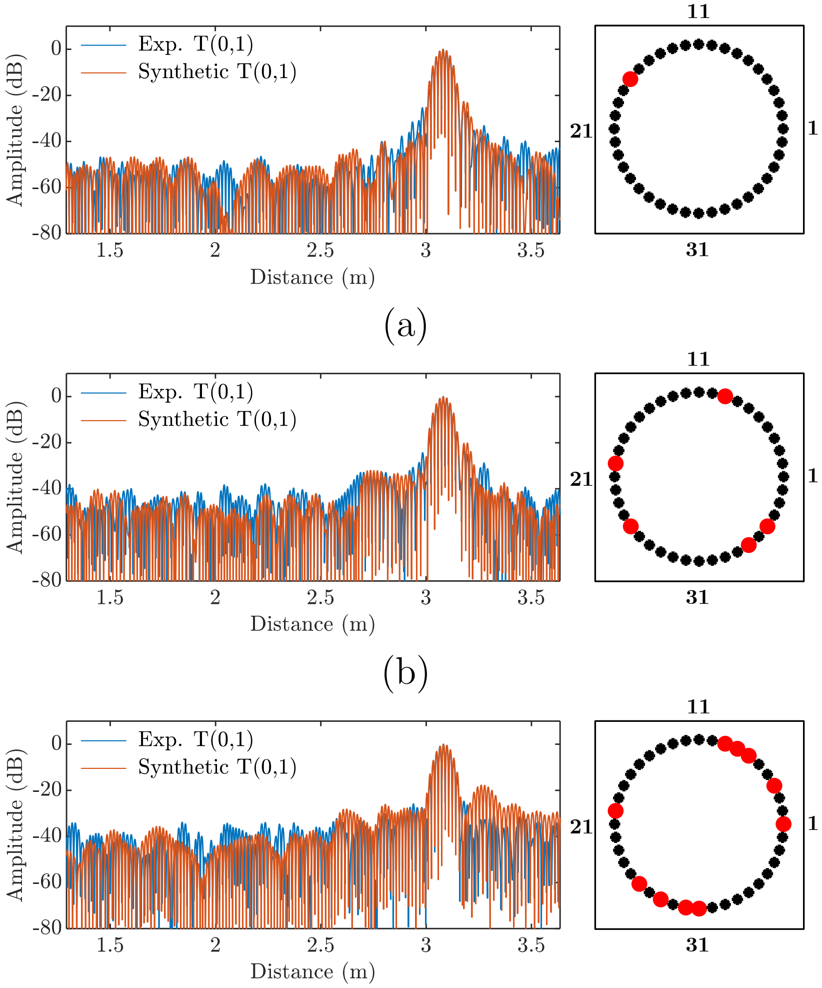

(a)

(b)

(c)

Figure 3.7: Comparison between the synthetic T(0,1) signals (shown in orange) with the experimental T(0,1) signals (shown in blue) with different coherent noise levels induced by disabling signals from several transducer channels, which are highlighted in red in the corresponding figures shown on the right. (a) One transducer channel disabled, (b) five transducer channels disabled, (c) and ten transducer channels disabled.

signals against those of the experimental T(0,1) signals, comprising 100 data samples. The strong linearity observed in the SNR values between these two datasets suggests that the proposed framework performs well in quantitatively capturing coherent noise in T(0,1) guided wave signals. Furthermore, the large set of realistic simulation data generated by the proposed frame-

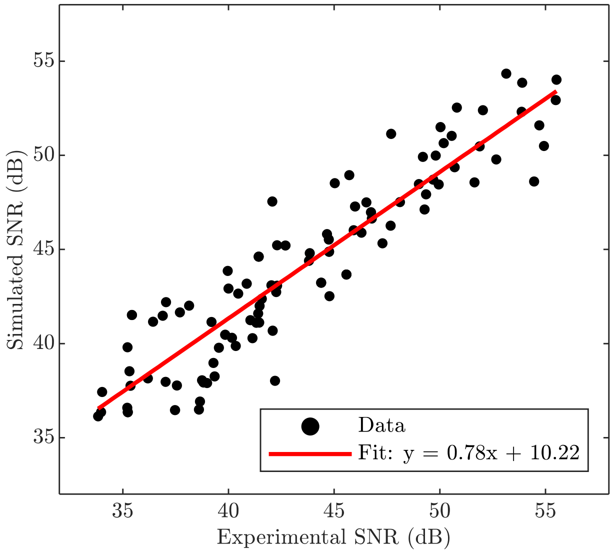

Figure 3.8: Scatter plot of the SNR values of the synthetic T(0,1) signals against those of the experimental T(0,1) signals, comprising 100 data samples.

work can be used for various applications that require such large datasets, such as the training of machine learning models for damage identification from complex guided wave signals and POD analysis.

In the next section, an application in the determination of the inspection range in pipe monitoring will be illustrated based on the POD analysis using the synthetic realistic data.

3.5 Application to inspection range estimation

In current industrial practice, the inspection range of a guided wave system for monitoring is determined based on the system sensitivity and noise levels, which rely on the subjective judgement of inspectors. In this section, a quantitative estimation method is presented for determining the inspection range of a guided wave monitoring system without human intervention, using guided wave signals generated in the proposed realistic simulation model.

3.5.1 POD analysis procedure

For the quantitative evaluation of the detection performance of a guided wave monitoring system at a specific location, a POD analysis was conducted using the synthetic guided wave signals. The methodology for the POD analysis employed in this study adheres to the guidelines outlined in MIL-HDBK-1823A 2009 (Nondestructive Evaluation System Reliability Assessment) [23], which is a universally accepted reliability assessment guideline for NDE. It provides comprehensive instructions on performing POD analysis based on signal response or hit-miss data. In this study, the POD analysis was carried out based on the signal response data.

POD curves illustrate how the detection probability varies with the defect parameter, such as flaw size, effectively quantifying the system's capability to detect defects when they are present. The POD value, represented as the blue shaded area in Figure 3.9, is defined as

$$\text{POD} = P(\hat{a} > \hat{a}_0 | \text{defect}), \tag{3.12}$$

where $\hat{a}$ represents the signal response, and $\hat{a}_0$ denotes the Detection Threshold. Another metric used to assess system performance in defect detection is the Probability of False Alarm (PFA), which indicates the system's likelihood of falsely identifying a defect when there is no defect present. The purple shaded area in Figure 3.9 illustrates this, and it is defined as

$$\text{PFA} = P(\hat{a} > \hat{a}_0 | \text{no defect}). \tag{3.13}$$

Traditionally, the POD curve based on the signal response can be calculated using linear regression. This method assumes that the relationship between the signal response and the flaw size is linear and that any data scatter follows

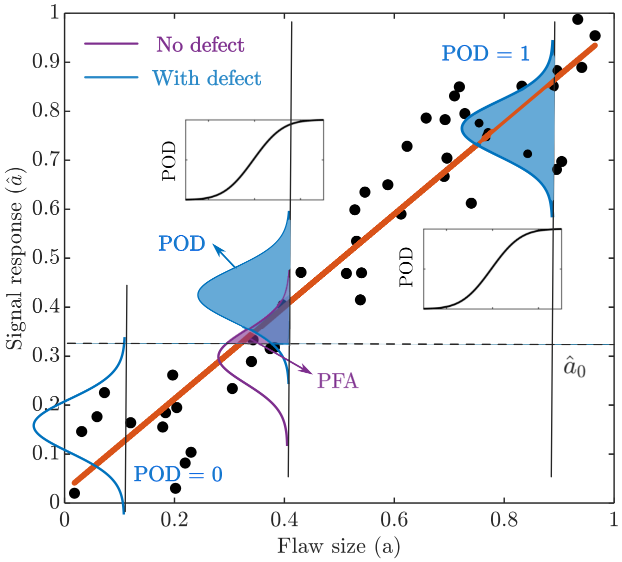

Figure 3.9: Illustration of the definition and calculation of a POD curve (adapted from Figure 9 on Page 28 in [103]).

the same probability distribution. The parametric model can be expressed as

$$\hat{a}_i = \beta_0 + \beta_1 a_i + \varepsilon_i. \tag{3.14}$$

Here, a_i and $\hat{a}_i$ represent the flaw size and the corresponding signal response measured from the experimental or simulation data. The model parameters β_0, β_1 and ε_i can be estimated based on the scattered data $(a_i, \hat{a}_i)$. β_0 and β_1 represent the intercept and slope, respectively, while ε_i is the random component following a normal distribution with a mean of zero and a standard deviation of τ, i.e., $\varepsilon \sim N(0, \tau)$. The parameter ε_i accounts for the uncertainty of the data collected in the experiments or simulation. Estimation of model parameters can be performed through linear regression, such as Ordinary Least-Squares (OLS) regression.

The shape of the POD curve can be described by the cumulative density function of a normal distribution, given by

$$p_{\mathrm{norm}}(x|\eta,\xi) = \frac{1}{\xi\sqrt{2\pi}} e^{-\frac{1}{2}(\frac{x-\eta}{\xi})}. \tag{3.15}$$

The parameters in Eq. (3.15) are related to the parameters in Eq. (3.14) as follows:

$$\eta = \frac{\hat{a}_0 - \beta_0}{\beta_1} = a_{50}, \tag{3.16}$$

and

$$\xi = \frac{\tau}{\beta_1}, \tag{3.17}$$

where a_{50} corresponds to the flaw size where the POD is 50%. Hence, the expression of POD is

$$\begin{aligned} \mathrm{POD}(a_i) &= P(\hat{a}_i > \hat{a}_0) \\ &= 1 - \Phi_{\mathrm{norm}}\left(\frac{\hat{a}_0 - (\beta_0 + \beta_1 a_i)}{\tau}\right) \\ &= \Phi_{\mathrm{norm}}\left(\frac{a_i - \eta}{\xi}\right), \end{aligned} \tag{3.18}$$

where Φ_{norm} represents the cumulative density function of a standard normal distribution.

With the estimated parameters based on the collected data, a confidence bound reflecting the error due to the limited sample size can be calculated using the Wald method based on the standard deviation in the estimated parameters [103].

3.5.2 Generation of datasets

To demonstrate the quantitative estimation method for determining the inspection range of a guided wave monitoring system in a practical scenario, a series of guided wave signals were generated using the proposed numerical framework. The simulation involved a 10-metre-long, 5-inch Schedule 40 steel pipe with 3 welds, designated as Pipe 3 in Table 3.1. To simulate the decay in amplitude caused by wave propagation, a high mass proportional damping coefficient of 1500/second, corresponding to an attenuation value of 1.98 dB/m, was implemented to represent a high-damping environment, such as when the pipe is buried underground [104]. In the simulation model, the welds were characterised by a width of 20 mm and a cap height of 3 mm, resulting in approximately 49% Cross-Sectional Change (CSC) and a reflection coefficient of about 41% in the absence of damping. It should be emphasised that the weld sizes in terms of CSC were exaggerated for illustrative purposes, exceeding practical norms. The positions of the welds are depicted in Figure 3.10, and defects were introduced as through-thickness defects with varying circumferential extent, reaching up to 6% CSC. An absorbing boundary condition was applied on the left side of the transducer ring, meaning only the waves reflected from the welds on the right side were analysed.

Table 3.1: Geometric and material information of the pipe modelled for POD analysis.

	Geometric					**Material**	**Material Properties**			
	Nominal Size (inches)	**Schedule**	**Outside Diameter (mm)**	**Wall Thickness (mm)**	**Length (mm)**		**Density (kg/m^3)**	**Young's Modulus (GPa)**	**Poisson's Ratio**	**Mass Proportional Damping Coefficient (Hz)**
Pipe 3	5	40	141.3	6.55	10000	P265GH	7850	210.86	0.285	1500

For the POD analysis, two sets of data were generated for comparison. One set comprised purely random noise, commonly employed in literature to include noise effects. Figure 3.10a demonstrates an example T(0,1) signal with random noise on both linear and logarithmic scales, showing a consistent noise level marked by the shaded grey area. The noise level can be estimated through an SNR calculation, similar to Eq. 3.11, by comparing the RMS amplitude of the random noise to the peak amplitude of the T(0,1) wavepacket. Based on this approach, the SNR of the simulated signal with random noise is approximately 65 dB, matching the random noise level measured in the representative experiment. The other dataset included both coherent and random noise, as shown in Figure 3.10b, generated using the proposed realistic simulation model. This signal exhibits a behaviour similar to the real experimental signal depicted in Figure 2.4. The coherent noise is proportional to the signal amplitude and decreases with wave propagation due to material damping and energy spread, whereas random noise remains constant.

In current industrial practice, the inspection range is typically determined according to Distance Amplitude Correction (DAC) curves. According to the ASTM (American Society for Testing and Materials) standard practice for guided wave testing of steel pipework [105], DAC curves are used to assess the attenuation and amplitude reduction over wave propagation distances, aiding in the assessment of damage extent, particularly in terms of pipe's CSC. In Fig. 3.10, DAC curves (dotted lines) were generated during post-processing using the Absolute Calibration method [106], based on known pipe features such as welds. The commonly used DAC curves include Flange DAC, Weld DAC, and Call DAC. Flange DAC illustrates the anticipated amplitude reflected from a feature with an approximate 100% reflection coefficient, while Weld DAC demonstrates the anticipated amplitude reflected from a pipe girth weld, typically presenting 20% to 25% CSC. The Call DAC level is generally established at roughly 6% CSC, representing the system's sensitivity to detect the defect. Additionally, the noise level is illustrated as the dark grey area in Fig. 3.10, and the Detection Threshold is typically set at 6 dB above the noise level to avoid false alarms in defect detection. The end of the detection/inspection is set as the point where the Call DAC drops below the Detection Threshold.

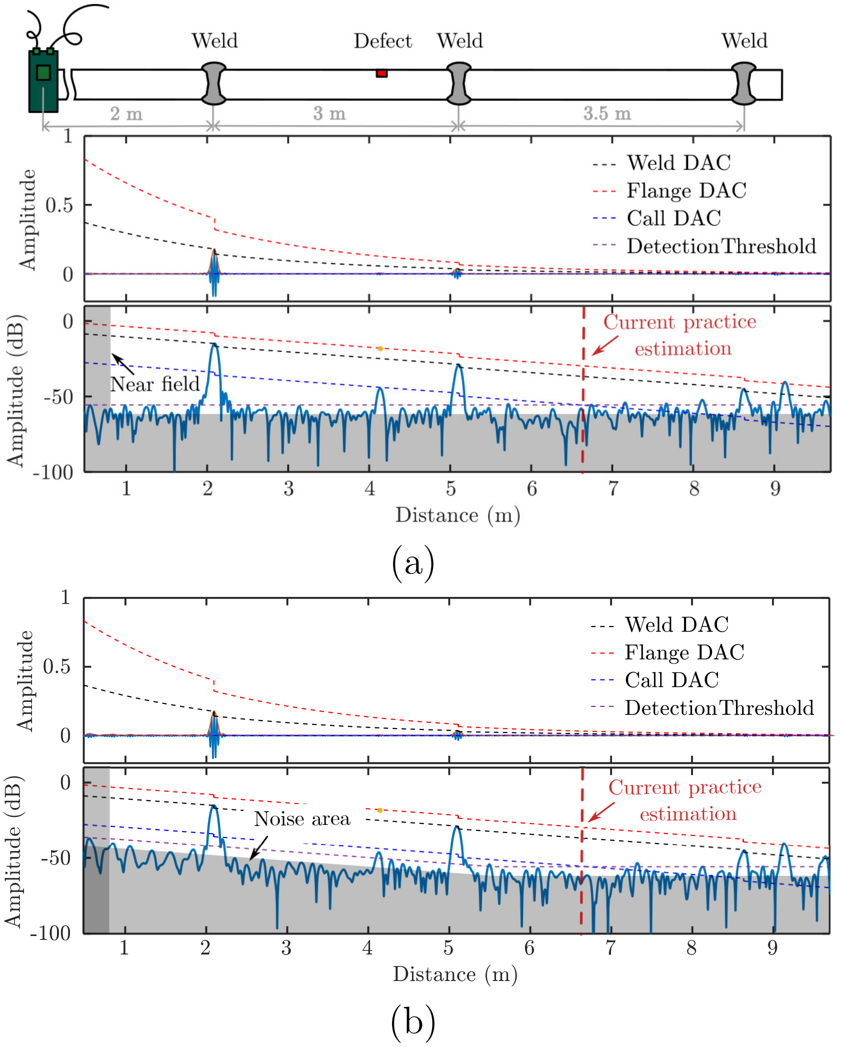

(a)

(b)

Figure 3.10: Example T(0,1) signals generated in the simulation for POD analysis, depicted on both linear (upper figure) and logarithmic (lower figure) scales. (a) T(0,1) signal with only random noise, (b) T(0,1) signal with both coherent noise and random noise. The defect is positioned at a distance of 3.54 m from the transducer ring.

In Figure 3.10, the noise area was subjectively marked based on intuitive noise levels, with the Detection Threshold set at 6 dB above the noise level. Consequently, in both cases depicted in Figure 3.10, the estimated inspection range is approximately 6.6 m. The estimation of the inspection range for these two cases, in Figure 3.10a and Figure 3.10b, shows similarity, as the intersection points fall within the range dominated by random noise, which exhibits similar levels for both cases. However, this method of determining inspection ranges presents two issues: firstly, the Detection Threshold is established based on subjective judgement of noise levels by the operator, and secondly, there lacks a quantified measure of confidence within the inspection range, which is not guaranteed to be 100%. Hence, a more objective, automatic, and quantitative estimation procedure will be presented in this section based on POD analysis.

In Figure 3.10, a certain area was analysed for the estimation of the inspection range of a guided wave SHM system. In practical guided wave monitoring, a near-field zone, as shown in Figure 2.4, exists on either side of the transducer ring, characterised by artificially reduced amplitudes unsuitable for defect quantification [105]. In the simulation, this region was set at 0.8 m away from the transducer ring for illustrative purposes, as indicated in grey on the left side of Figure 3.10a and Figure 3.10b. Consequently, the estimation area was defined as 1.5 m to 7.4 m for sampling defect locations, and POD curves were computed along the pipe axis at intervals of 60 mm, approximately one wavelength of the T(0,1) wave. A total of 100 locations along the pipe axis were considered to calculate the POD curves for estimating the inspection range.

To quantify the defect response, DAC curves were determined based on the weld reflections, as shown in Figure 3.10. In this study, the Flange DAC curve was used to quantify the reflection from a defect in terms of CSC. As indicated in Eq. (3.18), another key factor that determines the calculation of POD and PFA values is the Detection Threshold, $\hat{a}_0$. In this study, $\hat{a}_0$ is set to a value corresponding to 1% PFA [107, 108] to ensure fair comparisons across different cases. Due to variations in the noise level across cases, the Detection Threshold was adjusted accordingly to maintain a consistent PFA level.

3.5.3 Generation of POD curves

Figure 3.11a and Figure 3.11b illustrate the linear regression relationship between the signal response and flaw size in terms of CSC when the defect is positioned at a distance of 3.54 m from the transducer ring. Figure 3.11a is based on the data set with only random noise, whereas Figure 3.11b is based on the dataset with both coherent noise and random noise. At the chosen location, coherent noise dominates in Figure 3.11b. The estimates of β_0

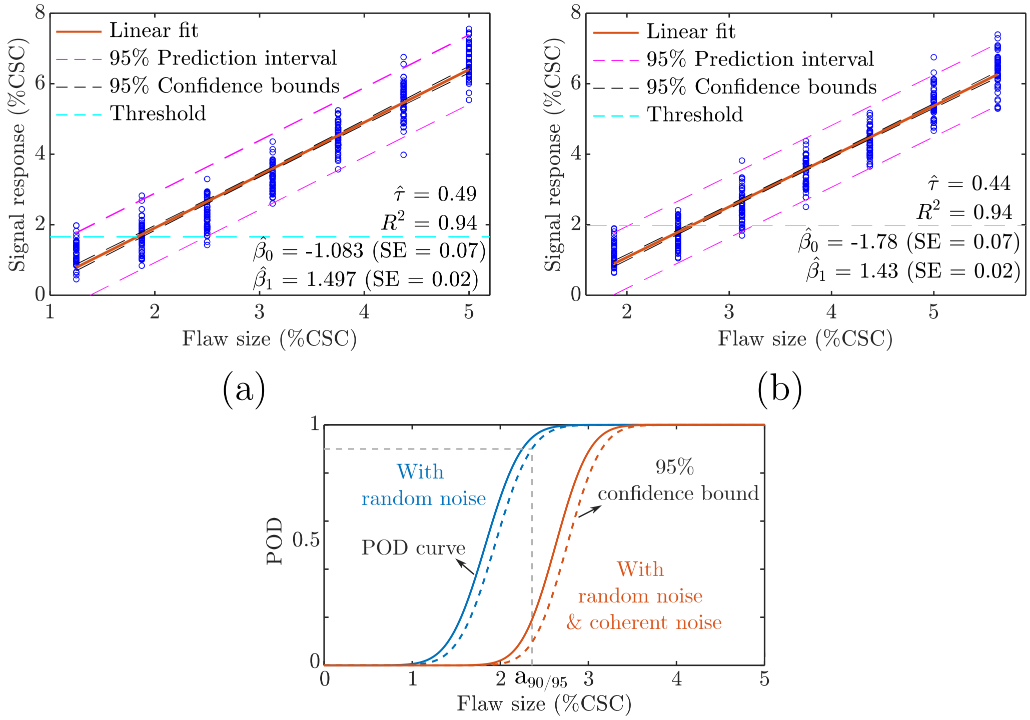

(a) (b)

(c)

Figure 3.11: Linear regression relationship between the signal response and flaw size in terms of CSC and the corresponding POD curves when the defect is positioned at a distance of 3.54 m away from the transducer ring. (a) Linear regression of the data with only random noise, (b) linear regression of the data with both coherent noise and random noise, where $\hat{\beta}_0$ and $\hat{\beta}_1$ represent the estimated intercept β_0 and slope β_1 of the regression, respectively. SE denotes the standard error associated with these coefficients, while R^2 quantifies the coefficient of determination. (c) Comparison of the POD curves calculated based on two distinct datasets.

and β_1, along with the corresponding Standard Error (SE) of the estimates, are illustrated in Figure 3.11a and Figure 3.11b. These coefficients were subsequently used in accordance with Eq. (3.18) to compute the POD curves. The notably high coefficient of determination (R^2) in both cases indicates a linear relationship between the signal response and the increasing flaw size in terms of CSC, aligning with the findings reported in [109].

The POD curves and their corresponding 95% confidence intervals, calculated from two distinct datasets, are compared in Figure 3.11c. It is evident that the POD curve, when including coherent noise, shifts to the right of the curve derived from data considering only random noise. This shift implies that, for the same-sized defect, a lower POD value is expected when the influence of coherent noise is considered. In POD analysis, the $a_{90/95}$ value is typically of interest for comparison, representing the flaw size at which the system has 90% POD with 95% confidence. The $a_{90/95}$ values determined for these two cases are 2.36% CSC and 3.16% CSC, respectively, indicating the risk of overestimating POD when only random noise is considered in the calculation of POD curves. As mentioned before, coherent noise is proportional to signal amplitude and decreases with distance, whereas random noise remains constant, becoming more important as the distance increases. Therefore, modelling coherent noise in the range where it dominates is necessary for a more precise estimation of the inspection range.

3.5.4 Estimation of the inspection range

For the quantitative estimation of the inspection range of a guided wave system for pipe monitoring, POD maps along the pipe axis were generated based on two distinct datasets. Figure 3.12a presents the POD map calculated based on the data with only random noise, where the horizontal axis corresponds to the distance of the defect away from the transducer ring, the vertical axis corresponds to the flaw sizes, and the colour-coded map displays the corresponding POD values. Figure 3.12b presents the POD map calculated based on the data with both coherent noise and random noise. In both figures, the $a_{90/95}$ values at different distances are shown for quantitative comparison. In both POD maps, the $a_{90/95}$ flaw size increases with the increasing distance away from the transducer ring, indicating a decay in the system performance with increasing detection distance. It is noted that the dips observed in the POD maps in Figure 3.12 occur at the weld locations, where the signal response and the calculation of the POD curves differ from other regions due to the overlapping of defect reflections and weld reflections. This effect is specific to the physical pipe used in the simulation. Hence, the POD maps at the weld locations are excluded from the analysis for a fair comparison.

In Figure 3.12a, the $a_{90/95}$ curve exhibits different characteristics in the area near the transducer ring compared to that farther from the transducer ring. In the area near the transducer ring, the defect reflection generally exhibits a higher amplitude, resulting in a higher SNR with a constant random noise level. The signal response calculated based on the Flange DAC curve is less affected by random noise, leading to a smooth change in the $a_{90/95}$ curve in the nearby area. Conversely, for defects located far from the transducer ring, the signal response is significantly influenced by random noise, resulting in larger variations in the $a_{90/95}$ values.

In Figure 3.12b, the effect of coherent noise is included. The $a_{90/95}$ curve demonstrates evident fluctuations in the region close to the transducer ring, attributed to the significant influence of coherent noise on the defect reflection. In the region far from the transducer ring, random noise dominates the noise signal. The POD map displays variations similar to those observed in the POD map calculated based on the dataset with only random noise in

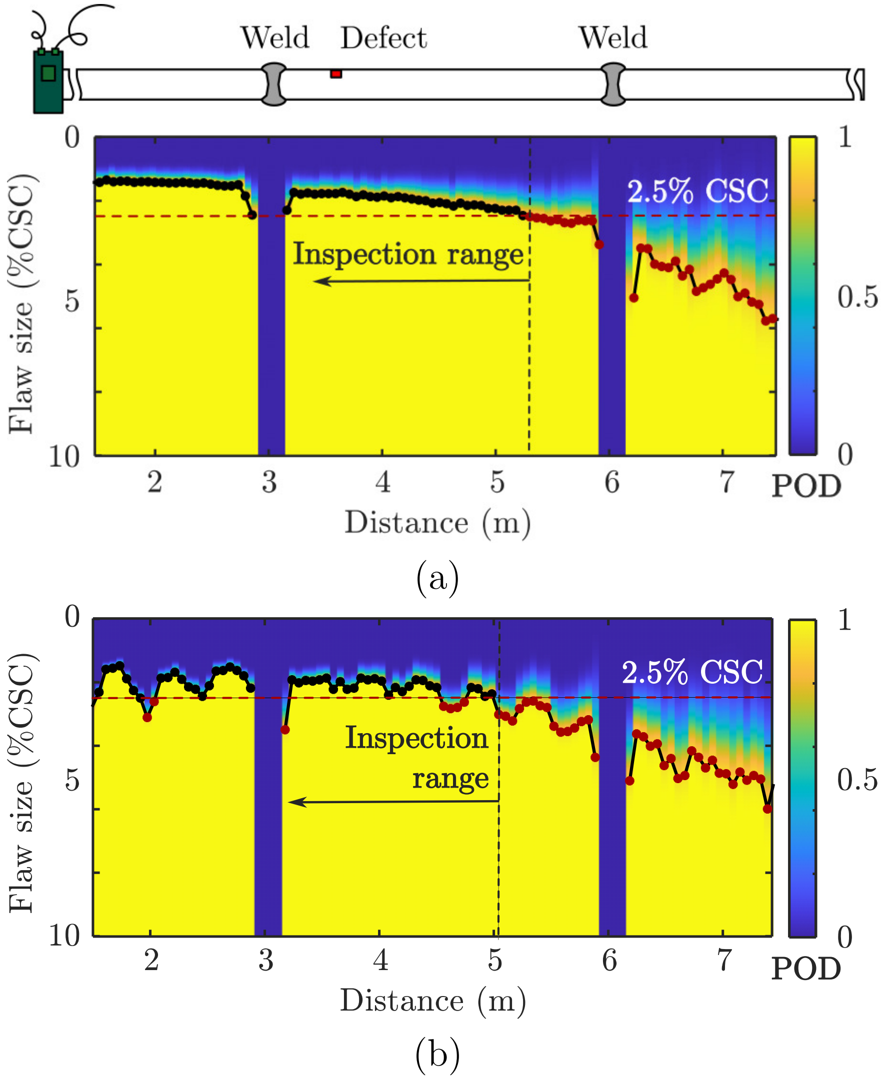

(a)

(b)

Figure 3.12: POD maps calculated from two distinct datasets for the quantification of the inspection range. (a) POD map calculated based on the data with only random noise, (b) POD map calculated based on the data with both coherent noise and random noise. The POD map was created by calculating the POD curve at different distances from the transducer ring. The plotted line with dot markers represents the $a_{90/95}$ flaw sizes at each distance. The black markers indicate values below the 2.5% CSC threshold, while the red markers indicate values above it.

Figure 3.12a.

For determining the inspection range with a specific sensitivity requirement, for example, 2.5% CSC as marked in Figure 3.12, a threshold line can be drawn, and the furthest distance at which the $a_{90/95}$ curve permanently falls below this threshold line specifies the inspection range. The locations where the $a_{90/95}$ flaw size exceeds 2.5% CSC are highlighted by the red points in Figure 3.12a and Figure 3.12b. For the same required $a_{90/95}$ flaw size, Figure 3.12b indicates that there are short regions with a lower POD within the inspection range due to the presence of coherent noise. The inspection range determined based on the dataset with only random noise data is approximately 5.28 m, while that determined based on the dataset with both coherent noise and random noise is about 5.04 m, albeit with some locations exhibiting lower POD values.

In comparison with the current industry practice for determining the inspection range, which stands at about 6.6 m for both cases based on the intersection between the Call DAC and the Detection Threshold as depicted in Figure 3.10, the method proposed in this study based on the POD map calculated using the realistic synthetic guided wave signals provides a more detailed quantitative estimation of the system's detection capabilities within the inspection range. In addition, the flaw sizes investigated in this study are less than 6% of the CSC, which falls below the industry standard Call DAC. This flaw size is typically considered small-scale and traditional damage detection systems often exhibit reduced confidence in it. However, by employing POD analysis using realistic synthetic signals, this research enhances the detectability of small-scale defects and provides quantified confidence levels, thus facilitating more informed decision-making.

3.6 Application to noise reduction

As discussed in Chapter 2, imbalances in transducer performance are a significant source of coherent noise within guided wave signal measurements. This has suggested that compensating for these imbalances may facilitate a reduction in coherent noise. This section explores a methodology for coherent noise reduction based on the estimation of transducer transfer functions, as introduced in Section 3.2.

3.6.1 Methodology

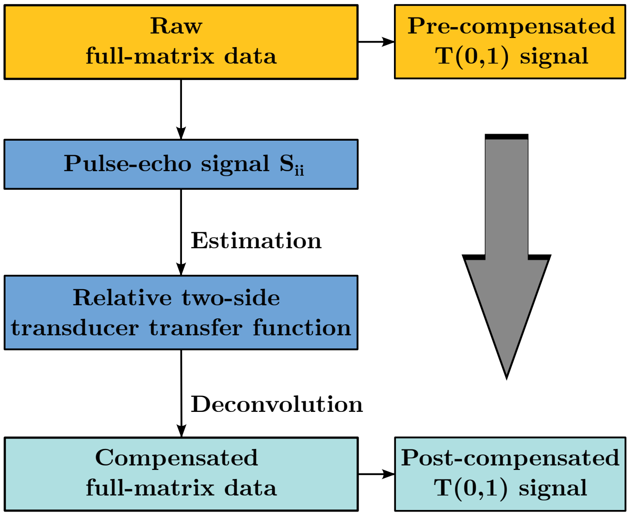

Figure 3.13: Flowchart for the noise reduction methodology based on the estimation of transducer transfer functions.

Figure 3.13 illustrates the flowchart for the proposed coherent noise reduction approach, which is based on the estimation of transducer transfer functions. For noise reduction purposes, the procedure differs slightly from that outlined in Section 3.2 for realistic signal generation. This approach employs experimental signals rather than ideal simulation signals to estimate the transfer functions. Specifically, a relative transfer function for a given transducer is derived by comparing its performance with a reference transducer, such as transducer No. 1. Additionally, instead of employing the CSM data capture configuration, FMC is used to obtain a full-matrix dataset. This ensures that the pulse-echo signal from an individual transducer is available for estimating its transfer function.

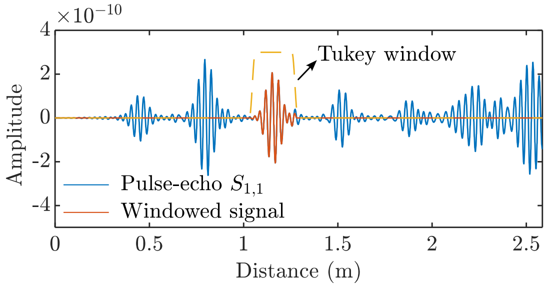

Figure 3.14: Reference pulse-echo signal $S_{1,1}$ (orange) acquired from transducer No. 1. This signal is used for estimating the relative transducer transfer functions. The original signal is shown in blue, and the Tukey window is highlighted by the yellow dotted line.

For the estimation of the relative transducer transfer functions, as illustrated in Figure 3.14, a quasi-A0 wave packet is windowed out by a Tukey window from a pulse-echo signal from an individual transducer, and then the relative two-side transfer function of transducer j can be calculated using a Wiener filter and is expressed as

$$T_{Tj}^{R} \cdot T_{Rj}^{R} \approx \frac{S_{1,1}^{\prime *} \cdot S_{jj}^{\prime}}{|S_{1,1}^{\prime}|^2 + \vartheta}, \tag{3.19}$$

where T_{Tj}^{R} and T_{Rj}^{R} represent the relative transfer functions of transducer j acting as transmitter and receiver, respectively. $S_{1,1}^{'}$ denotes the experimental pulse-echo signal from transducer No. 1, and $S_{jj}^{\prime}$ denotes the experimental pulse-echo signal from transducer j.

Subsequently, the signal transmitted from transducer i and received by transducer j can be compensated through deconvolution:

$$S_{ij}^{c} = \frac{S'_{ij}}{T_{Ti}^{R} \cdot T_{Rj}^{R}}. \tag{3.20}$$

By invoking the reciprocity principle [110], which states that the transfer function between transducer i as transmitter and j as receiver is equivalent to that between transducer j as transmitter and i as receiver, the above equation simplifies to:

$$S_{ij}^{c} = \frac{S'_{ij}}{\sqrt{T_{Ti}^{R} \cdot T_{Ri}^{R}} \cdot \sqrt{T_{Tj}^{R} \cdot T_{Rj}^{R}}}. \tag{3.21}$$

To obtain the compensated T(0,1) signal, all signals within the compensated full-matrix dataset are summed. It is important to note that this methodology presumes the presence of negligible random noise relative to coherent noise within the experimental signals — a condition that can be satisfied through signal averaging, as discussed in Chapter 2. In addition, as illustrated in Figure 3.14, this method requires a clear separation between the quasi-A0 wave packet and other wave modes. In cases where the pipe diameter is small, the quasi-A0 and quasi-S0 wave packets may overlap, in which case more advanced mode separation techniques are required to ensure accurate mode isolation and maintain the applicability of the method [111, 112]. However, for most practical oil and gas pipelines, which typically have large diameters and sufficient mode separation, the approach of separating the quasi-A0 mode based on wavepacket arrival time remains valid and effective.

3.6.2 Simulation Validation

The proposed method for coherent noise reduction was initially validated using the virtual experimental signals generated from the model of Pipe 1 in Section 3.3. This signal with coherent noise was obtained by varying its amplitude, phase, and response band to serve as an experimental signal. The signal received by transducer No. 1 was utilised as a reference to compute the relative transfer functions for the other transducers. Subsequently, these relative transfer functions were applied to the full-matrix captured data to achieve noise compensation.

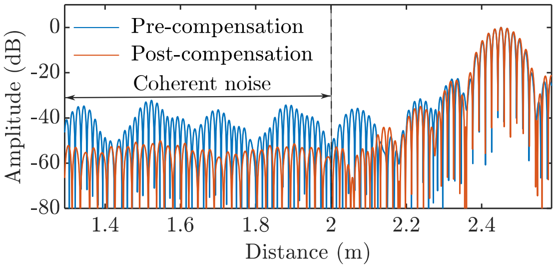

Figure 3.15: Comparison between the pre-compensated T(0,1) signal and the compensated T(0,1) simulation signal after coherent noise reduction. A discernible reduction in the coherent noise level is evident.

A comparative analysis of the T(0,1) signal before and after noise compensation is illustrated in Figure 3.15. The segment between 1.3 m and 2 m preceding the first reflection from the pipe end, identified as coherent noise in Figure 3.15, was analysed. The coherent noise level was quantified using the SNR, as delineated by Eq. 3.11. For the pre-compensated T(0,1) signal, the coherent noise level was measured at 41.59 dB. After the application of noise reduction techniques, the SNR of the post-compensated T(0,1) signal was enhanced to 56.17 dB, corresponding to a 14.58 dB enhancement.

3.6.3 Experimental validation

The performance of the proposed coherent noise reduction method was evaluated using experimental signals collected in Section 3.4. Figure 3.16a compares the pre-compensated T(0,1) signal with the post-compensated signal with coherent noise reduction. The compensation resulted in a 6.25 dB increase in SNR, enhancing it from 56.97 dB to 63.22 dB. The RMS level of coherent noise was computed within the region spanning 1.3 m to 2.67 m, as shown in Figure 3.16a. The effectiveness of coherent noise reduction on experimental signals is less pronounced compared to that on the simulated signals, due to the large error in the estimation of transducer transfer functions, as discussed in Section 3.4.1.2. It is important to note that the experimental T(0,1) signal was acquired with a 21-time signal averaging to mitigate the impact of random noise. When random noise predominates, the coherent noise reduction method, which relies on transducer transfer function compensation, is less effective. Figure 3.16b compares the original T(0,1) experimental signal collected without signal averaging and the compensated signal. In this scenario, coherent noise reduction becomes ineffective due to significant errors in estimating relative transducer transfer functions caused by the substantial presence of random noise. To further assess the efficiency of the noise

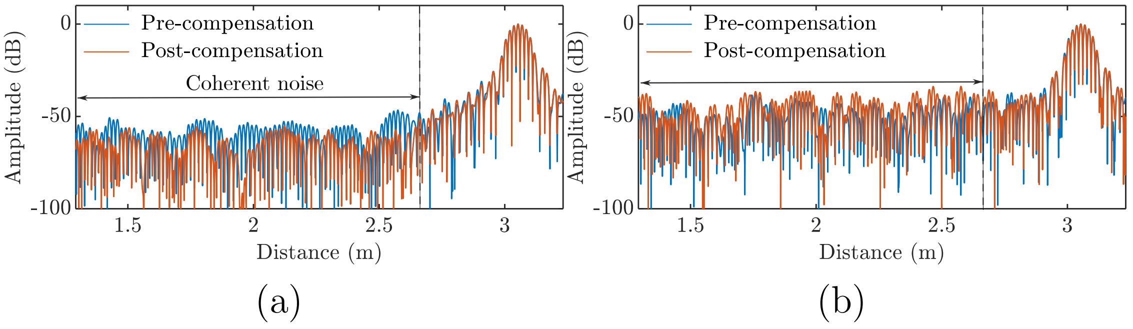

Figure 3.16: Comparison between the pre-compensated T(0,1) signals and the post-compensated T(0,1) signal: (a) with signal averaging to mitigate random noise; (b) without signal averaging, where random noise predominates.

reduction method, an artificial corrosion patch was manufactured on Pipe 2 using 3-axis CNC (Computer Numerical Control) machining and the experimental T(0,1) signal was collected using the setup described in Section 2.3.2. Figure 3.17 showcases the manufactured corrosion patch. The patch has a radius of approximately 80 mm and a depth of 5.32 mm, representing a 40% loss in thickness.

Figure 3.17: Artificial corrosion patch manufactured on Pipe 2, which has a radius of approximately 80 mm and a depth of 5.32 mm, representing a 40% loss in thickness.

The T(0,1) signal, collected after introducing the corrosion patch, is depicted on a logarithmic scale in Figure 3.18 in blue. The T(0,1) signal before corrosion is also presented in orange for comparison, and the expected location of the corrosion patch is marked. However, identifying the reflected signal from the raw time trace signals is challenging due to its low amplitude, which is not easily distinguishable from coherent noise.

Enhancing damage detection sensitivity might be achievable through baseline subtraction [113]. In this case, the signal before the introduction of the artificial corrosion patch serves as a baseline for subtraction, aiming to eliminate the influence of coherent noise. However, as illustrated in Figure 3.19, the residual signal, highlighted in blue, still makes it challenging to discern the corrosion patch due to the overbearing residual coherent noise.

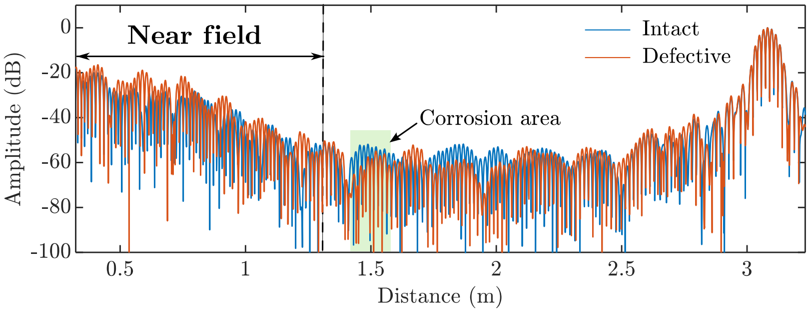

Figure 3.18: Comparison of the raw T(0,1) time trace signal collected from Pipe 2 on a logarithmic scale, before and after the introduction of the corrosion patch.

As depicted in Figure 3.18, the signals exhibit different coherent noises, which can be induced by several factors. One possibility is a change in installation conditions, as discussed in Section 2.3. The transducer ring was removed during the corrosion patch's manufacture and reinstalled afterwards, leading to the change in installation conditions. This is evidenced by the variation in signal prior to reaching the corrosion site. Despite being in the near field — typically less reliable for defect quantification due to the proximity of the transducer ring — the changes between these two T(0,1) signals qualitatively signify the impact of installation condition variations on coherent noise levels. Additionally, the introduction of the corrosion patch itself may alter the noise profile due to mode conversions and reverberations. These disturbances result in a residual coherent noise that masks the reflection from the corrosion, making it difficult to locate the defect from the signal post-baseline subtraction.

To address this, a baseline subtraction was applied to the compensated signals, where coherent noise reduction was already performed. Figure 3.19 contrasts the residual signal of the pre-compensated and post-compensated T(0,1) signals, and an improvement in the residual signal amplitude at the expected corrosion patch location is evident, enhancing the identifiability of

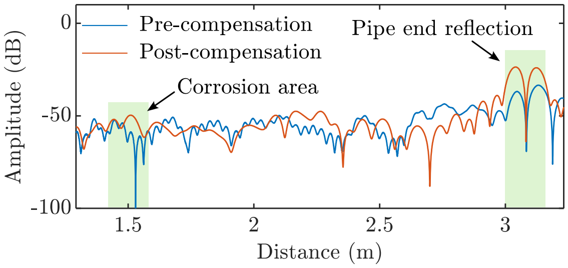

Figure 3.19: Residual T(0,1) signal comparison: The original signal with coherent noise (pre-compensation) versus the signal after coherent noise reduction (post-compensation).

the defect. Furthermore, the more pronounced residual signal at the pipe end reflection may also serve as an indicator of the defect's presence. However, residual coherent noise persists at other locations, such as around 2.25 m, where signal increases are observed. This indicates that although coherent noise reduction improves the detectability of the defect, complete isolation of the damage signature remains challenging, particularly when the defect reflection is weak compared to the background noise level. Overall, although the damage signature does not fully emerge from the residual noise, these findings demonstrate the potential of coherent noise reduction technology to enhance system performance in damage detection, particularly under substantial measurement uncertainty.

3.7 Summary

In this chapter, a numerical framework tailored to generate realistic signals for reliability estimation purposes is presented, focusing on the application of guided wave SHM for pipe monitoring. It specifically incorporates key characteristics of real signals: random noise and coherent noise caused by the imbalance in transducer performance within guided wave monitoring systems. The effectiveness of the proposed methodology is demonstrated through simulation and experiments, and proves to be an efficient method both for capturing features within individual experimental traces as well as when performing statistical comparisons. Furthermore, an application to assess the reliability of a guided wave system in terms of the inspection range for pipe monitoring is illustrated based on a series of POD analyses using synthetic data. The comparison of POD curves derived from ideal and realistic simulation data underscores the necessity of considering coherent noise for accurate POD curve calculations. Moreover, the POD analysis based on realistic synthetic data provides a quantitative estimation of the inspection range with more details compared to the current industry practice.

Furthermore, an application of the transducer transfer function estimation in coherent noise reduction is explored. The methodology involves experimental signal acquisition through FMC to derive relative transfer functions for each transducer by comparing pulse-echo signals to a reference transducer's signal, followed by deconvolution for compensating for imbalances in transducer performance using their transfer functions. The method is validated through simulations and experiments. Simulation validation showed a significant improvement in the SNR after noise compensation. Experimental validation also indicated an SNR improvement, though less pronounced due to estimation errors in transfer functions, particularly when random noise was prevalent. The method is further tested with an artificial corrosion patch on a pipe, confirming the potential for improved damage detection through baseline subtraction and coherent noise reduction.

The numerical framework proposed in this study provides, for the first time, an efficient method for generating realistic guided wave signals tailored for practical applications. This framework facilitates the performance evaluation of a guided wave monitoring system under diverse and realistic conditions within the SHM context, offering enhanced flexibility and feasibility. Although the focus of this chapter has been on pipe monitoring, the modelling strategy developed in this work is applicable to a broad range of structural configurations. Since the framework is based on an FE model combined with realistic representations of measurement noise, it can be adapted to simulate ultrasonic wave responses in other types of structures such as plates, stiffened panels, or components with more complex geometries. By modifying the structural model and sensor layout accordingly, the same approach can be used to replicate realistic signal behaviour in different SHM scenarios. Beyond guided wave testing, the framework can also be extended to realistic bulk wave simulation in phased array ultrasonic testing by incorporating representations of random noise from the measurement system and coherent noise arising from non-ideal transducer element performance. This further enables the production of realistic phased array images tailored for a range of diagnostic purposes. Furthermore, the proposed framework exhibits potential as a versatile tool for generating realistic simulation data with broader applications, including training machine learning models. This capability addresses challenges related to data scarcity in the NDE and SHM communities.

Chapter 4

Digital twin-based reliability estimation

Most of the material presented in this chapter is based on findings detailed in a forthcoming publication [P2].

4.1 Introduction

SHM is promising to enhance structural integrity and safety by providing real-time, continuous monitoring of structures. This proactive approach employs permanently installed transducers to detect and assess damage, significantly improving the ability to maintain and extend the lifespan of critical structures [114]. Compared with traditional NDE-based inspections, SHM offers numerous advantages including minimal human intervention, reduced downtime, lower access and operational costs, and potentially higher sensitivity and precision due to the significant increase in data availability [113]. These benefits facilitate a transition from schedule-based inspections to condition-based maintenance, further improving safety and decreasing maintenance expenses. While the development of SHM technologies, such as new detection methods [115,116] and the optimisation of sensors [117], has advanced rapidly in recent years, the regulation and standardisation of these systems remain undeveloped, largely due to the challenges associated with reliability estimation.

The reliability estimation of SHM systems is crucial for their commercialisation, certification, and eventual implementation across various industries [118]. For system developers and providers, accurately quantifying the performance of SHM systems is not only a technical necessity for system optimisation but also a commercial requirement to convincingly demonstrate their effectiveness to potential clients [119]. From a certification standpoint, demonstrating that SHM systems meet stringent performance standards, including detection capabilities, reliability, and longevity, remains a prerequisite for their approval for large-scale industrial use [120]. This is especially true in aerospace sectors where safety is critical and strict standards are required [121]. Moreover, in the realm of lifecycle management of critical infrastructure, such as aircraft, quantified performance data, particularly regarding damage detection and false call rates, plays a vital role in supporting damage-tolerant design approaches. Damage-tolerant design assumes that flaws may exist and ensures structures maintain sufficient integrity until detected damage can be addressed. Incorporating reliability estimation results, such as POD curves, into this framework enhances the accuracy of structural integrity assessments and enables better-informed condition-based maintenance strategies. Additionally, the establishment of reliability estimation underpins the wide acceptance and deployment of SHM systems by providing the necessary confidence to adopt these technologies and fully harness their potential benefits in terms of improved safety, optimised maintenance, and extended asset life [122].

Currently, specific standards for the reliability estimation of SHM systems are lacking. For NDE methods though, reliability estimation is fairly well regulated; for instance, as mentioned in Chapter 3, MIL-HDBK-1823 [23] serves as a best practice guideline, providing comprehensive guidance on assessing NDE reliability using a POD analysis. Given that both SHM and NDE techniques generally use similar physical principles for damage detection, the POD analysis methods detailed in MIL-HDBK-1823 have been taken as a starting point to develop reliability estimation methods for SHM systems. For instance, SHM systems can be employed as NDE systems with periodic inspections, adhering to regulatory requirements, to obtain a POD curve for qualification [123–125]. However, this application does not fully leverage the continuous monitoring capabilities and the potential benefits of large data flows inherent in SHM systems. Meeker et al. [126] have thoroughly discussed whether and how the POD analysis models and procedures outlined in MIL-HDBK-1823 can be adapted for the reliability estimation of SHM systems. They note that while there are some similarities between NDE and SHM, the direct application of POD analysis from NDE to SHM is complicated by fundamental differences between the two techniques.

A key challenge in POD analysis for SHM systems is ensuring data independence, which is crucial for linear regression-based POD analysis. In SHM data, potential dependencies arise from various factors. Typically, an SHM system is permanently installed on a structure, and data for POD analysis is usually gathered from a limited number of samples with progressive damage, leading to clustered and correlated data points [127]. Additionally, SHM data is frequently collected at short intervals, further increasing the likelihood of correlation due to repeated measurements [128]. Moreover, certain SHM strategies for defect detection, such as SVD and Independent Component Analysis (ICA) [35], rely on analysing trends in damage growth. These strategies inherently create dependency since the response data for a particular flaw size is influenced by data from other flaw sizes.

The effects of dependent data on POD curves have been discussed in detail, both mathematically and experimentally, in [127, 129, 130]. Ignoring the presence of dependence among data samples may lead to biased and inconsistent estimators in linear regression, as well as either overestimated or underestimated standard errors, resulting in erroneous confidence bounds in the corresponding POD curves [131]. In NDE applications, the independence of the collected data is guaranteed by fabricating a series of representative samples with varying explanatory variables, such as flaw size. The presence of variability in the process allows each inspection to be treated as statistically independent. However, achieving such independence through experiments is nearly impossible in SHM applications due to prohibitively high costs and a broader range of variability to consider. Researchers have proposed various methods to address the issue of data dependence in SHM POD analysis. One approach is to use random effects models, which allow for the inclusion of random effects to capture the variability between different structures or samples while still enabling the estimation of POD curves [127,132]. Another method, known as the Length at Detection (LaD) method, has been explored to deal with repeated data by only using the flaw size when the defect is first detected. These two methods have been discussed and compared in detail in [132].

Another difference in POD analysis between SHM and NDE lies in the consideration of variability [124, 133]. In NDE, the operators, structure geometry, defect morphology, and coupling conditions of sensors change from inspection to inspection, and a meaningful POD curve should incorporate variability from all these sources present in the measurement system [134]. In POD analysis of NDE, variability is captured by performing a large number of measurements on multiple representative samples. In contrast, SHM systems are typically permanently installed on the structures under monitoring, with measurements automatically recorded without direct human interference. This setup significantly reduces variability related to human factors, structure geometry, and sensor mounting process. However, potential sources of variability for SHM arising from in situ effects need to be considered, including electronic noise [130], changing environmental conditions [35, 120], and sensor degradation [135]. In addition, NDE is generally performed at regions of suspected damage or degradation, whereas SHM transducers are usually installed at limited locations but have a larger coverage area than the transducer installation location, such as in guided wave monitoring. In this case, spatial dependence needs to be taken into account in the POD calculation, an example of which has been illustrated in Chapter 3.

In the context of SHM, it is often impractical to incorporate all sources of variability through experimental approaches. This impracticality arises from the prohibitive costs associated with extensive testing on representative structures, the use of expensive testing equipment, and the need to generate representative EOCs. Consequently, there is an increasing shift toward MAPOD methodologies, which leverage advanced computational resources to achieve statistically robust POD analysis [136, 137]. The use of simulation models in MAPOD allows for extensive exploration of potential variability and the generation of independent datasets. To represent variability in these models, assumptions must be made about the probability distributions of input parameters that influence this variability [138, 139]. However, verifying these assumptions can be challenging, and an extensive number of simulations may be required to explore all possible combinations of parameters. To mitigate these challenges, considerable efforts have been made to exploit limited empirical experimental data to enhance the MAPOD analysis. For example, Bayesian methods can be used to estimate POD parameters or evaluate variability in model input parameters, by integrating simulation data with limited experimental data [77,140,141]. Additionally, Liu et al. [35] proposed a superposition method that integrates experimental signals, collected from damage-free structures, with simulation-generated damage signatures. This method effectively incorporates the variability and uncertainty of experimental signals into the simulated data, thus enhancing the robustness of the POD analysis.

Another distinction from NDE systems is that the performance of an SHM system depends not only on the equipment but also on installation conditions, the state of the structure under inspection, and environmental factors. This performance is dynamic, evolving throughout the system's lifecycle due to degradation. On one hand, it is impractical to account for all these variabilities in the analysis, as this would require an unrealistic number of test pieces and measurements over a long period. On the other hand, the POD curve, typically estimated before the system is deployed and at the beginning of its lifecycle, may not accurately reflect performance throughout the entire lifecycle of the SHM system. This is due to its limited predictive capability in assessing the performance of a system that has undergone significant degradation.

In light of the above, rather than relying on a single POD analysis conducted before system deployment, implementing a time-evolving POD analysis tailored to a specific structure and adapted to changing measurement conditions can offer more accurate and timely predictions of system performance. This dynamic capability can be realised through the MAPOD method, where the simulation model, used for data generation, is continuously updated to reflect real-time measurement conditions. This updated simulation model, often referred to as a "digital twin", serves as a virtual counterpart to the actual structure, mirroring real-time measurement conditions accurately. Given the aforementioned advantages and associated versatility, this study proposes a digital twin-based reliability estimation framework to provide a tailored, structure-specific, and time-evolving performance evaluation of an SHM system throughout its entire lifecycle.

In the digital twin-based reliability estimation framework, key modelling parameters in the simulation such as material properties, excitation signals, and random noise levels are dynamically estimated based on in-situ measurements. These in-situ measurements encapsulate temperature variations, transducer performance, and instrument noise levels. This process of dynamic estimation aims to minimise discrepancies between simulation-generated data and in-situ experimental data. The validity of the digital twin model is demonstrated through tests conducted both on a laboratory experimental SHM system and a commercial system. Once the measurement conditions are accurately estimated, defects of interest can be modelled to predict the performance of an SHM system in damage detection on a specific structure under current measurement conditions, without the need to create actual physical defects. The flexibility of modelling techniques also allows for easily changing any defect parameters such as height, orientation, location or roughness. The reliability estimation procedure based on the digital twin model is then demonstrated and verified by comparing it with a superposition-based method proposed by Liu et al. [35] and validated by Heinlein et al. [142].

4.2 A digital twin-based reliability estimation framework

4.2.1 Generic framework

The proposed digital twin-based framework for the reliability estimation of an SHM system involves five key steps: (1) in-situ measurement, (2) system estimation, (3) defect modelling, (4) temperature compensation and damage detection, and (5) MAPOD analysis, as shown schematically in Figure 4.1.

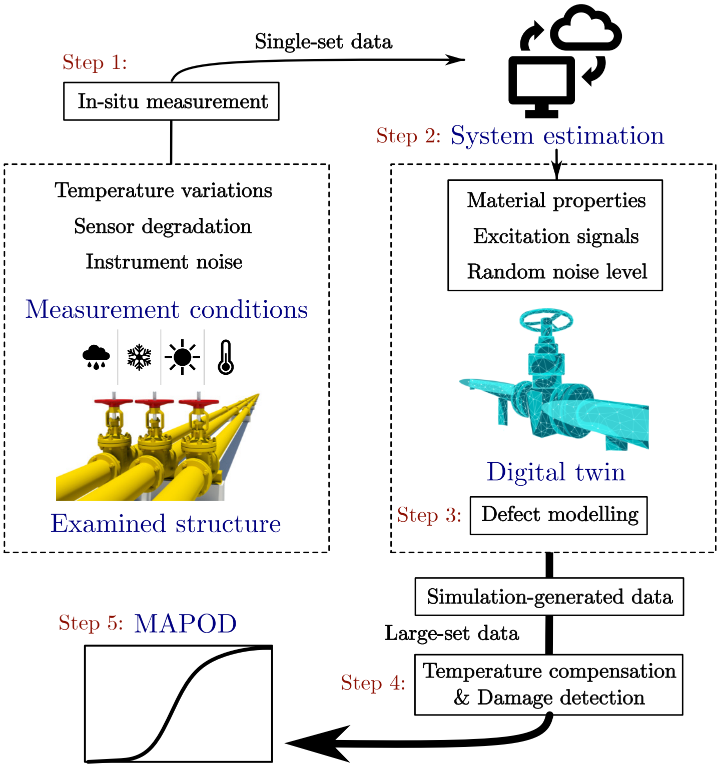

Figure 4.1: Schematic of the proposed digital twin-based framework for the reliability estimation of SHM systems.

For an SHM system installed on a structure, guided waves are periodically excited and measured to monitor the structure's condition. In addition to structural information, the collected in-situ measurements inherently capture the effects of environmental and system conditions. In this framework, three major factors affecting guided wave monitoring are considered: temperature variations, transducer degradation, and instrument noise. When quantitative assessment of the SHM system's reliability is required, for instance following the detection of signal anomalies, a digital twin model can be established based on the current in-situ measurements to evaluate system performance. To enable this, a full-matrix dataset with extended recording duration is first collected using the FMC acquisition setup.

In the second step, three key parameters in the simulation model, including material properties, excitation signals, and random noise levels, are updated based on the estimation using the in-situ measurements acquired in Step 1. The detailed technical methodology for the estimation of each parameter will be discussed in the following sections. This updated simulation model is referred to as a digital twin model in this study.

For reliability estimation purposes, a series of defects with varying explanatory parameters, such as flaw sizes and locations, are modelled in the digital twin model in the third step. A large set of digital twin-generated data specific to the examined structure and measurement conditions at the moment of interest is obtained for subsequent signal processing and statistical analysis.

In the fourth step, for the extraction of the damage response from the digital twin-generated guided wave signals, the most widely used baseline subtraction method is employed in the proposed framework [143]. In this method, the baseline signal is subtracted from the current measurement signal, and the damage response is measured from the residual signals after subtraction. In the proposed framework, the baseline signal is obtained at the initial stage of the inspection at any available temperature. Considering the possible temperature change during the in-situ measurement, a temperature compensation method, namely the Baseline Signal Stretch (BSS) method [15], is employed to mitigate the influence of temperature variations on the subtraction signals. The methods to handle temperature variations in damage detection are not limited to the BSS. More advanced methods, such as the Location Specific Temperature Compensation (LSTC) method [34] and the SVD method [144], can be employed as needed.

The final step of the proposed framework involves calculating the POD curves based on the damage response extracted in Step 4. In this study, POD analysis based on linear regression, as detailed in [23], is employed. The related statistical assumptions are tested before conducting the POD analysis. It should be noted that POD analysis is not limited to linear regression-based methods; more sophisticated methods, such as the LaD method [132], should be employed when any of the assumptions for linear regression are invalid.

The digital twin-based framework proposed in this study offers several advantages over traditional baseline-based reliability estimation methods, such as the superposition-based method proposed by Liu et al. [35]:

1. **No need for extensive baseline collection**: This framework does not rely on collecting baseline signals under various environmental conditions, which is potentially challenging in field measurements. Applying environmental variations for baseline collection within a short period, as done in laboratory settings, is often impractical in the field.
2. **Tolerance to existing defects**: Traditional baseline-based methods require baseline signals to be collected from damage-free structures. In contrast, the digital twin model does not require the structure to be intact; small defects do not affect the estimation of the model's input parameters.
3. **Flexibility and robustness**: The digital twin-based method can adapt

to varying conditions by updating input parameters based on in-situ measurements, enabling flexible and robust reliability estimation without pre-collected baselines. However, this flexibility relies on the digital twin capturing all major influencing factors; if unmodelled effects, such as humidity, become significant, the reliability of the estimation may be compromised.

4.2.2 Technical methodology

4.2.2.1 Estimation of material properties

One significant impact of measurement conditions, particularly temperature variations in this study, on guided wave monitoring is the alteration of material properties, which consequently affects wave propagation. The influence of temperature on material properties, especially longitudinal and shear wave velocities, is well-recognised and has been extensively investigated [145–148]. However, these relationships are typically studied in well-controlled laboratory environments and may not be always available to structures in service.

To address this, some in-situ measurement methods have been developed to test material properties during service [149, 150] with the aid of high-frequency ultrasonic testing devices [151, 152]. These methods, however, often require specialised equipment and provide localised measurements. In response, an in-situ material property estimation method is proposed in this study using guided wave signals collected from the same transducer ring used for damage detection. This approach eliminates the need for additional equipment and configurations. Moreover, a guided wave measurement contains information equivalent to a spatial average, as the waves traverse the entire component during propagation, which is difficult to achieve with conventional localised measurements.

The estimation process involves two steps based on the full-matrix data collected in Step 1: first, estimating the shear wave velocity using the fundamental torsional T(0,1) mode, and second, estimating the longitudinal wave velocity using the flexural modes, which will be described below. It is worth noting that the influence of temperature on material density and pipe geometry is assumed to be negligible, given the small thermal expansion coefficient of carbon steel. For example, a 100 °C increase in temperature would result in a pipe expansion of only about 0.12% in length, based on the typical thermal expansion coefficient of carbon steel, which is around 1.2×10^{-5}/ °C [145].

In this section, the proposed method is detailed and demonstrated using the simulation data generated in Section 3.3 based on Pipe 1 listed in Table 2.1. The wave excitation and reception occur at one end of the pipe, mirroring the experimental setup used for validation in subsequent sections.

Shear wave velocity estimation

The T(0,1) signal used for estimating the shear wave velocity is obtained by summing all signals in the full-matrix dataset collected during the in-situ measurement in Step 1. For this estimation, two distinctive T(0,1) wave packets, reflected from pipe features such as the pipe end cut, are windowed using a Tukey window. The phase velocity at the central frequency of the T(0,1) signal corresponds to the shear wave velocity of the examined pipe, as shown in Figure 4.2a. The phase velocity at the central frequency is calculated by

$$c = \frac{2\pi f_c d}{\Delta\theta}, \tag{4.1}$$

where f_c is the central frequency of the excitation signal, d is the wave propagation distance between the two windowed pipe feature reflections (twice the pipe length in this study), and $\Delta\theta$ denotes the phase shift between the two windowed pipe feature reflections.

For a more stable calculation of the phase shift, $\Delta\theta$, the ratio of the two frequency spectra of the windowed pipe feature reflections is calculated using the Wiener filter. The unwrapped phase of the spectrum ratio at the central frequency represents the phase shift between the two reflections. Note that a $2b\pi$ adjustment is needed to resolve phase ambiguity in phase wrapping, where b is an integer determined by the non-dispersive property of the T(0,1) mode. The correct b ensures that the ratio of the two frequency spectra around the central frequency remains non-dispersive, as shown in Figure 4.2b. In the noise-free simulation case, the estimated shear wave velocity is 3233.475 m/s, with an estimation error of approximately 0.03% compared with the ground truth.

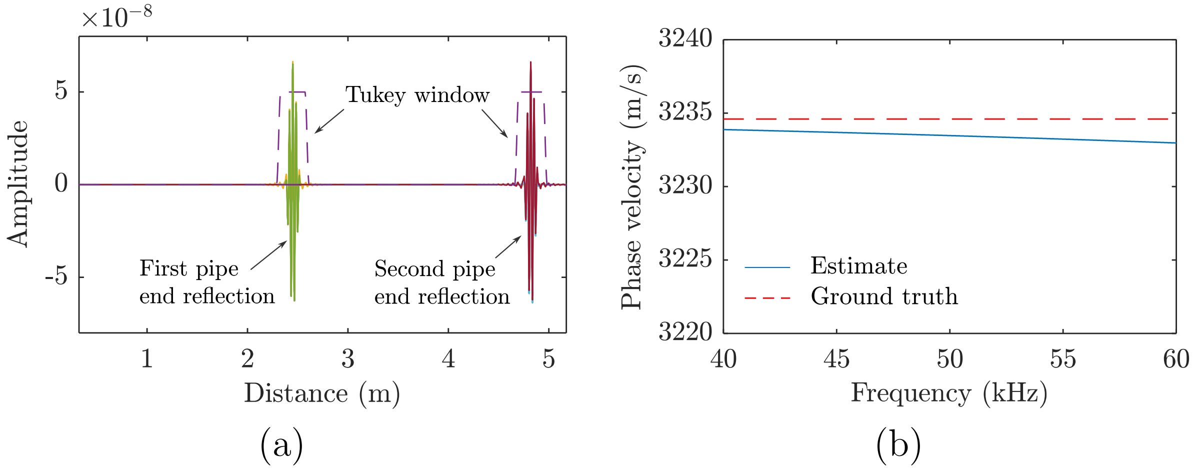

Figure 4.2: Estimation of the shear wave velocity using T(0,1) wave packets reflected from pipe features. (a) The first and second T(0,1) reflections from the pipe end, windowed by Tukey windows. (b) Phase velocity estimates in the frequency domain, with the phase velocity at the central frequency of 50 kHz representing the shear wave velocity.

Longitudinal wave velocity estimation

Estimating longitudinal wave velocity using guided waves is less straightforward than estimating shear wave velocity due to the dispersive nature of guided wave modes that are sensitive to longitudinal velocities, such as

L(0,2) longitudinal wave mode and F(n,3) flexural wave modes, as shown in Figure 2.2. This often involves an inversion process by matching the phase velocity dispersion curve with theoretical predictions [153].

The L(0,2) longitudinal wave mode is nearly non-dispersive within the frequency range typically used in guided wave pipe monitoring, and its phase velocity corresponds to the longitudinal wave velocity. However, for longitudinal wave modes, excitation is achieved by applying force in the pipe's axial direction, which requires an additional configuration of the transducer ring when the fundamental torsional T(0,1) mode is used for damage detection. In contrast, flexural wave modes can be obtained using the same transducer ring configuration used for damage detection. The same full-matrix dataset collected for estimating shear wave velocities can be used to extract flexural wave modes by applying the phase shift corresponding to the circumferential order on both the excitation and reception sides [60]. This method allows for the estimation of both shear wave velocity and longitudinal wave velocity using a single set of full-matrix data without changing the transducer ring configuration. Therefore, flexural wave modes are used in the proposed framework to estimate the longitudinal wave velocity.

Due to the multi-mode nature of guided waves in pipes, multiple flexural wave modes, denoted as F(n,m), can exist within the excitation frequency range. Figure 4.3 compares the F(1,m), F(2,m), and F(3,m) family guided wave signals extracted from the simulated full-matrix dataset, with the first arrival time of each mode reflected from the pipe end marked. The F(3,m) family guided waves exhibit significant dispersion, making it difficult to extract individual wave packets due to time-domain overlap. Conversely, the F(2,m) mode has a moderate amplitude, providing a good SNR and moderate dispersion, allowing for the separation of wave packets in the time domain. Therefore, the F(2,m) mode is used in the proposed framework for estimating the longitudinal wave velocities.

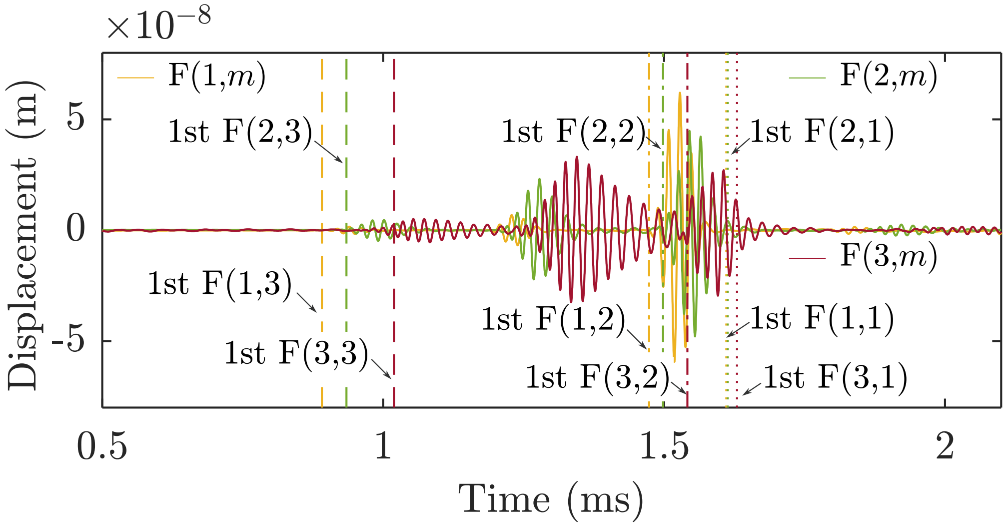

Figure 4.3: Comparison of the F(1,m), F(2,m), and F(3,m) family guided wave signals extracted from the full-matrix dataset, with the corresponding first arrival time of each mode reflected from the pipe end marked.

Figure 4.4a shows the extracted F(2,m) family wave modes reflected from the pipe end, with the corresponding expected ToFs marked. Extra wave packets due to mode conversions can be seen apart from the direct reflections. For example, the second wave packet in Figure 4.4a arises from mode conversion between the F(2,2) and F(2,3) wave modes at the pipe end. The F(2,2) mode propagates to the pipe end and converts to the F(2,3) mode, travelling back to the transducer ring, or vice versa. The amplitude of the F(2,2) mode wave packet is higher than that of the first direct F(2,3) wave mode reflected from the pipe end. This observation suggests that, of the two possible mode conversion scenarios, it is more likely that the F(2,3) wave mode is converted from the F(2,2) mode, rather than the converse. The higher amplitude of this F(2,3) wave packet ensures a higher SNR, thereby increasing accuracy in wave velocity estimation. Therefore, this wave packet with mode conversion is extracted using a Tukey window for the first reference wave packet for phase velocity calculation of the F(2,3) mode. This converted F(2,3) mode propagates further, and the second wave packet reflected from the pipe end can be extracted and used as the second reference wave packet for the calculation of the F(2,3) phase velocity, as shown in Figure 4.4a.

The phase velocity of the F(2,3) wave mode in the frequency domain, represented by the dispersion curve, is calculated using Eq. (4.1) based on the extracted reference F(2,3) wave packets and is shown by the blue line in Figure 4.4b. An optimisation procedure is performed to update the longitudinal wave velocity to match this estimated dispersion curve. In this study, the Golden Section Search method is used as a basic optimisation method with an acceptable convergence speed for determining longitudinal wave velocity [154]. The forward model in this optimisation process involves calculating the theoretical dispersion curve of the F(2,3) mode for each iteration, which is then compared to the experimentally estimated curve to guide the optimisation.

In this optimisation procedure, the Mean Square Error (MSE) value between the updated and the estimated dispersion curve within the frequency range of interest is calculated to construct the cost function. In the illustrative simulation case, the MSE is calculated across the dispersion curve between 44 kHz and 55 kHz, centred at the excitation signal frequency of 50 kHz. The updated dispersion curve, depicted by the yellow line in Figure 4.4b, aligns closely with the estimated dispersion from the F(2,3) wave packets within this range. Both curves are close to the dispersion curve derived from the ground truth of the longitudinal wave velocity, which is represented by the red dashed line in the same figure. The estimated longitudinal wave velocity based on this procedure is 5987.43 m/s, which has an error of 0.01% compared to the ground truth of 5988.3 m/s.

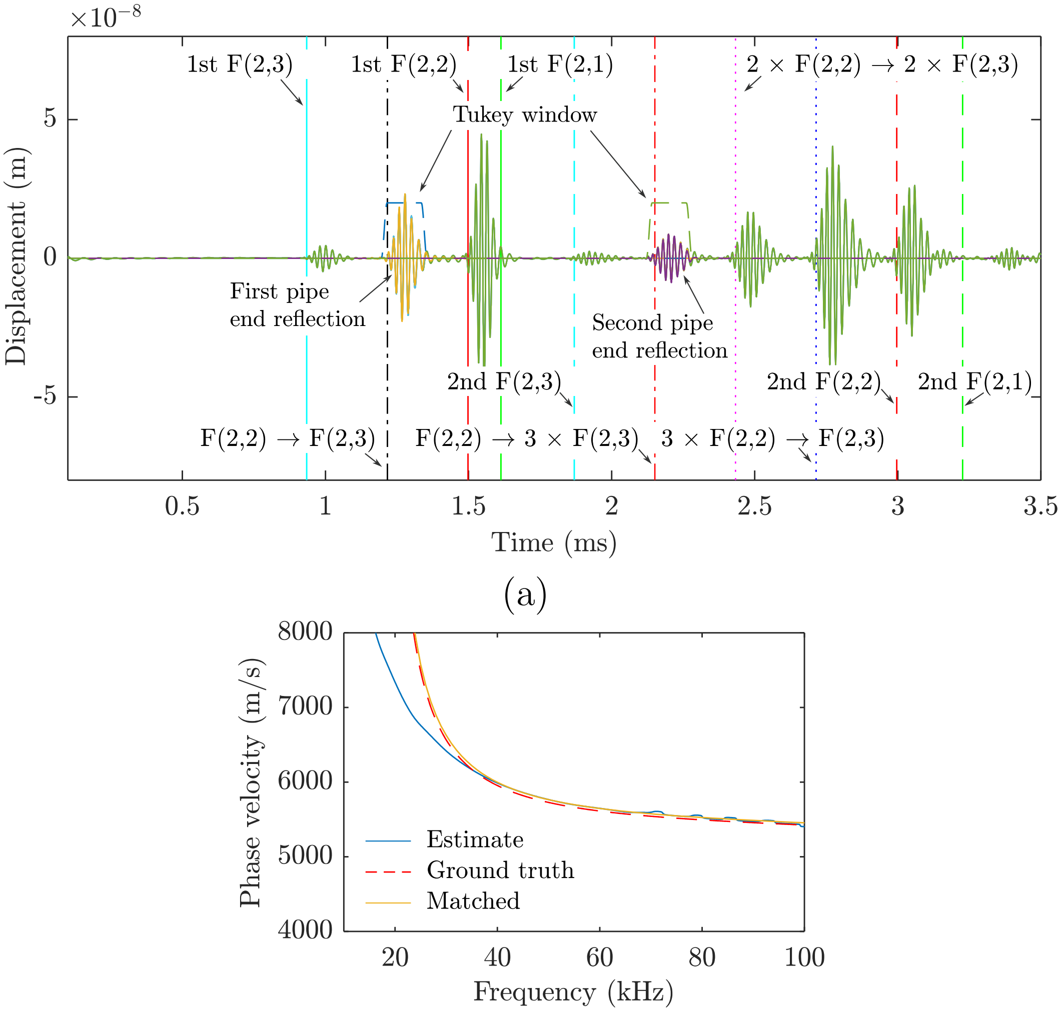

(a)

(b)

Figure 4.4: Estimation of the longitudinal wave velocity based on the F(2,3) wave packets reflected from a pipe feature. (a) The extracted F(2,m) family wave modes reflected from the pipe end, with the corresponding expected ToFs marked. The F(2,3) wave packets reflected from the pipe end are windowed using Tukey windows for the calculation of the F(2,3) phase velocities. (b) The dispersion curve estimated based on the windowed F(2,3) wave packets, compared with the dispersion curve updated by the iteration procedure, and the dispersion curve calculated from the ground truth of the longitudinal wave velocity.

4.2.2.2 Estimation of transducer performance

The estimation of transducer performance under various environmental conditions follows the methodology outlined in Section 3.2. Once the material properties have been accurately estimated, the calibration simulation model in the transducer performance estimation scheme (Figure 3.2) is updated accordingly. The transducer transfer functions are derived from a comparison between representative experimental signals and idealised calibration simulation signals. Excitation signals in the digital twin model are refined by convolving the original excitation signal with the estimated transfer function of each transducer, which accounts for the transducer performance imbalance.

4.2.2.3 Estimation of random noise

The random noise level is estimated based on the latter stages of long-duration full-matrix signals, where guided waves have fully dissipated, leaving what is assumed to be pure random noise. This process is detailed in Section 2.3.1.4. In the digital twin model, both the channel-specific dependencies of random noise and the overall random noise level of T(0,1) signals, quantified by SNR, are considered. Channel dependence of random noise is managed by adjusting the relative amplitude ratio of Gaussian white noise added to each channel of the simulation model before applying the transducer transfer function on the reception side. An adjustment factor is applied uniformly to the Gaussian white noise across all channels to match the random noise SNR of the in-situ T(0,1) measurement. This adjustment accounts for changes in the random noise level after the transducer transfer function is applied, which inherently has a limited bandwidth.

4.2.2.4 Temperature compensation and damage detection

Baseline subtraction method

After establishing the digital twin, a large set of guided wave signals with defect modelling can be generated. To improve defect detectability, the baseline subtraction method is applied in this framework [143]. This method involves using a baseline signal collected at the initial stage of inspection and comparing it with a newly collected current signal through simple point-by-point subtraction. Ideally, any structural changes can be identified from the level of the residual signal after subtraction.

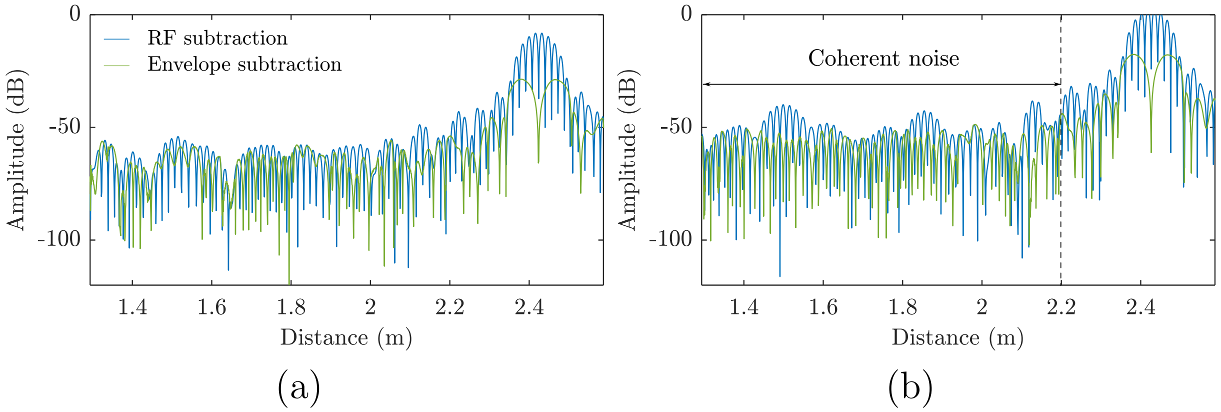

(a) (b)

Figure 4.5: Two example residual signals collected at different temperatures, subtracted from the baseline collected at 23.12 °C, using RF subtraction and envelope subtraction. (a) The current signal was collected at 29.26 °C. (b) The current signal was collected at 45.50 °C.

Baseline subtraction can be performed using either Radio Frequency (RF) subtraction or envelope subtraction. It has been shown that the residual signal from envelope subtraction is lower than that from RF subtraction [15]. Figure 4.5 compares two example residual signals collected at different temperatures using RF subtraction and envelope subtraction. It can be observed that the residual signal level with envelope subtraction is much lower than that with RF subtraction, especially in the range of residual coherent noise, as marked in Figure 4.5b. However, envelope subtraction leads to a non-linear defect response when the baseline signal is not zero, as shown by the equation:

$$|u_{\text{current}}| - |u_{\text{baseline}}| = |u_{\text{baseline}} + u_{\text{defect}}| - |u_{\text{baseline}}| \neq |u_{\text{defect}}|\,, \tag{4.2}$$

where u_{current}, u_{baseline}, and u_{defect} are the current signal, baseline signal, and defect signal, respectively. This is especially the case when coherent noise is present. Therefore, RF subtraction is used in the proposed framework for this study.

Baseline signal stretch for temperature compensation

The performance of the baseline subtraction method is affected by environmental conditions, especially temperature variations in this study. The influence of temperature variations on the residual signals from baseline subtraction has been widely discussed, and corresponding temperature compensation methods have been well developed [15,32]. Generally, the residual signal between the current signal and the baseline signal increases with the temperature difference between the two signals due to the temperature-induced phase shift. The BSS method is the most commonly used method to address this problem and will be employed in the framework proposed in this study [147].

For a non-dispersive wave mode propagating over a distance d, the baseline signal in the frequency domain can be expressed as

$$U_0(\omega) = S_0(\omega) e^{-i\frac{\omega}{c_0}d}, \tag{4.3}$$

where $S_0(\omega)$ denotes the excitation signal in the frequency domain and c_0 is the phase wave velocity at the baseline temperature. The current signal, with a temperature variation and therefore different wave velocities, can be expressed as

$$U_1(\omega) = S_0(\omega)e^{-i\frac{\omega}{c_1}d} = S_0(\omega)e^{-i\frac{\omega}{c_0}d\cdot\frac{c_0}{c_0+\Delta c}}, \tag{4.4}$$

where c_1 is the phase wave velocity of the current signal at the current temperature, and Δc is the wave velocity change due to temperature variations.

For the compensation of the phase shift induced by temperature variation, a stretch factor can be applied to the current signal:

$$U_1^s(\Omega) = \frac{S_0(\omega)}{S_0(\Omega)}S_0(\Omega)e^{-i\frac{\Omega}{c_0}d}, \tag{4.5}$$

where Ω is transformed angular frequency and $\Omega = \frac{c_0}{c_0+\Delta c} = \beta\omega$, and β is the stretch factor. Compared with the baseline signal in Eq. (4.3), it can be seen that the waveform of the excitation signal is changed due to the stretch. Therefore, a correction term is applied to solve this problem, and the signal with temperature compensation is

$$U_1^c(\Omega) = F(\Omega)U_1^s(\Omega), \tag{4.6}$$

where $F(\Omega)$ is the correction factor, given by $F(\Omega) = \frac{S_0(\Omega)}{S_0(\omega)}$.

It should be noted that in Eq. (4.6), the propagating wave is assumed to be a non-dispersive single mode. When the wave mode is dispersive, the stretch factor β is frequency-dependent instead of a constant. When different modes are present in the signal, the stretch factors corresponding to the individual modes are needed for compensation. In realistic guided wave signals, coherent noise is present apart from the main T(0,1) wave mode. As discussed in Chapter 2, this coherent noise is contributed by different wave modes with different travelling distances, which means different stretch factors should be calculated for different components. This is impractical in guided wave signal analysis and is why the baseline stretch method usually has limited performance in reducing the coherent noise part. To address this challenge, more advanced temperature compensation methods have been proposed, such as the LSTC method by Mariani [34].

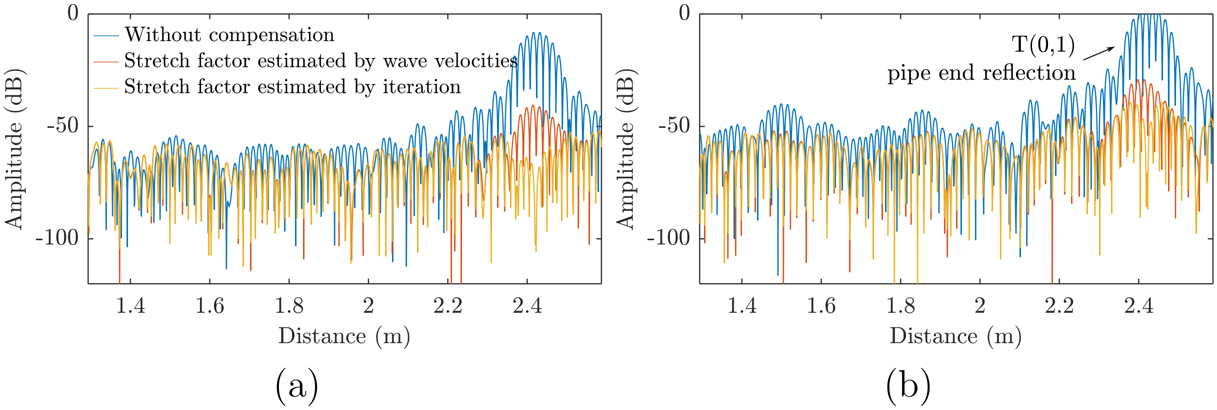

Figure 4.6: Temperature compensation based on the baseline stretch method. (a) The current signal was collected at 29.26 °C. (b) The current signal was collected at 45.50 °C.

In the literature, the stretch factor is commonly determined iteratively by applying a range of stretch factors until the best match is achieved between the compensated current signal and the baseline signal. From the expression of β, it can also be determined by the ratio of the wave speed at two different temperatures. In the proposed framework, the wave velocities are estimated in real-time using in-situ measurement, and thus can be directly used to determine the stretch factor of the current signal. Figure 4.6 shows two examples of residual signals after baseline subtraction. The baseline was collected at 23.12 °C and the current signals were collected at 29.26 °C and 45.50 °C, respectively. The residual signals with temperature compensation, where the stretch factor is determined by the wave velocity ratio and through iteration, are compared with those without temperature compensation. It can be seen that the overall residual signal is significantly reduced after temperature compensation using the BSS method. The main difference between the two residual signals, using the stretch factor determined by the wave velocity ratio and iteration, is in the amplitude of the T(0,1) pipe end reflection, while the residual level for the coherent noise part remains similar. In the context of guided wave testing for pipe monitoring, reflections from pipe features are easily identified, while identifying defects present in the coherent noise range is more challenging and of greater interest. To achieve effective temperature compensation and efficient determination of the stretch factor, this study employs the stretch factor determined by the wave velocity ratio.

4.2.2.5 POD analysis

After extracting the signal response from the large dataset generated by the digital twin model, the POD analysis is performed to quantitatively evaluate the performance of the SHM system at the moment of interest. The POD analysis procedure is detailed in Section 3.5.1. For estimating the parameters in linear regression, the bootstrapping method is used due to its versatility over the OLS method [155]. Unlike OLS, bootstrapping does not require normal distribution assumptions for the residual errors and provides a non-parametric way to estimate confidence intervals when the underlying distribution is unknown or complex. The bootstrapping method for linear regression involves repeatedly resampling with replacement from the original dataset and fitting a linear regression model to each sample, creating an empirical distribution of the regression coefficients. This allows for robust estimation of standard errors and confidence intervals without relying on traditional distributional assumptions.

In addition, data independence can be assessed from the covariance matrix, which is calculated statistically without extra assumptions. In traditional OLS linear regression, data is assumed to be independent, meaning the covariances between the parameters β_0 and τ (i.e., $\sigma_{\beta_0\tau}$) and between β_1 and τ (i.e., $\sigma_{\beta_1\tau}$) are assumed to be zero. However, this is not always valid for SHM data, as discussed in Section 4.1. In this study, the covariances $\sigma_{\beta_0\tau}$ and $\sigma_{\beta_1\tau}$ in the covariance matrix are calculated to test the independence of the data generated by the digital twin model for reliability estimation purposes.

4.3 Validation of digital twin model

4.3.1 Laboratory experimental validation

In this section, the digital twin model within the proposed reliability estimation framework is demonstrated and validated in a controlled laboratory environment. The establishment of the digital twin model is detailed, including the estimation of key model parameters at different temperatures, such as material properties, transducer performance, and random noise levels. Finally, the synthetic data generated by the digital twin model are compared with the experimental data for validation.

4.3.1.1 Experimental setup

As discussed earlier, a key factor that affects the performance of a guided wave SHM system is temperature variation, especially in field measurements. In this study, a temperature-controlled guided wave monitoring system was developed to collect data at different temperatures. Figure 4.7 shows the complete experimental setup designed for this purpose. It includes three main components: a guided wave testing system, a temperature control system, and a temperature sensing system.

The guided wave testing system, based on the Verasonics system, used the same configurations for T(0,1) guided wave excitation and sensing as detailed in Section 2.3.2. The temperature control system included a thick jacket of

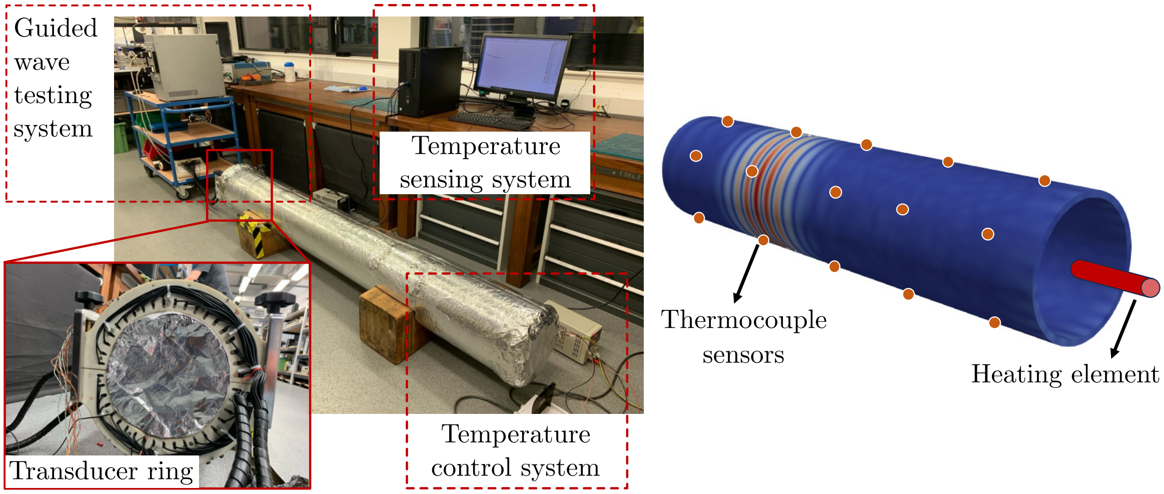

(a) (b)

Figure 4.7: The temperature-controlled guided wave monitoring system developed to collect data at different temperatures. (a) The complete experimental setup, featuring three main components: the guided wave testing system, temperature control system, and temperature sensing system. (b) The configuration of the heating system and the placement of thermocouple sensors (denoted by the red circles) for temperature monitoring.

thermal insulation and a heating element placed at the centre of the pipe. The inspected pipe was heated to a specified temperature. The thermal insulation reduced heat loss and aided temperature stability when the heating element was switched off. The temperature distribution along the pipe axis was initially non-uniform, with lower temperatures at the pipe ends. To achieve a uniform temperature distribution, two computer fans installed at the ends of the pipe were used to accelerate air circulation inside the pipe, promoting even heat distribution along the pipe. In this study, a uniform temperature distribution was assumed to isolate the effects of overall temperature variation on the SHM system's reliability. Although minor temperature gradients can occur in real pipelines, particularly at pipeline junctions or locations where different fluid streams merge, these effects are outside the scope of this study.

For temperature sensing, 20 thermocouple sensors were installed at five equally spaced locations along the pipe axis, with four sensors placed equidistantly around the pipe circumference at each location, as shown in Figure 4.7b. This setup monitored the temperature distribution along the entire pipe and provided feedback to the temperature control system for precise temperature regulation.

The pipe under test is Pipe 1 listed in Table 2.1, which is an 8-inch Schedule 60 steel pipe with a length of 2370 mm. Detailed geometrical dimensions and material properties of this pipe can be found in the same table. During data collection, the pipe was heated to approximately 55 °C, after which the heating element was switched off to allow the pipe to cool to ambient temperature. Guided wave signals were collected at uniform 15-minute intervals during the cooling phase. Specifically, a long-duration FMC dataset was collected at each temperature to estimate material properties, transducer performance, and random noise levels. The data acquisition took approximately two minutes per FMC dataset.

Figure 4.8 shows the temperature record during the experimental data collection process, along with statistical features calculated from the 20 thermocouple sensors. At each temperature, the central line within the box represents the median, while the lower and upper edges of the box correspond to the 25th and 75th percentiles, respectively. The whiskers stretch to the furthest data points that are not outliers, and any outliers are marked individually with a '+' symbol [156]. It can be seen that the temperature is relatively uniform across the pipe, although variation increases at temperatures above 50 °C. Consequently, data collected at temperatures below 50 °C were used for analysis to minimise the effects of non-uniform temperature distribution, as indicated by the dotted line in Figure 4.8. Within this range, the maximum temperature difference between the highest and lowest points is 3.1 °C.

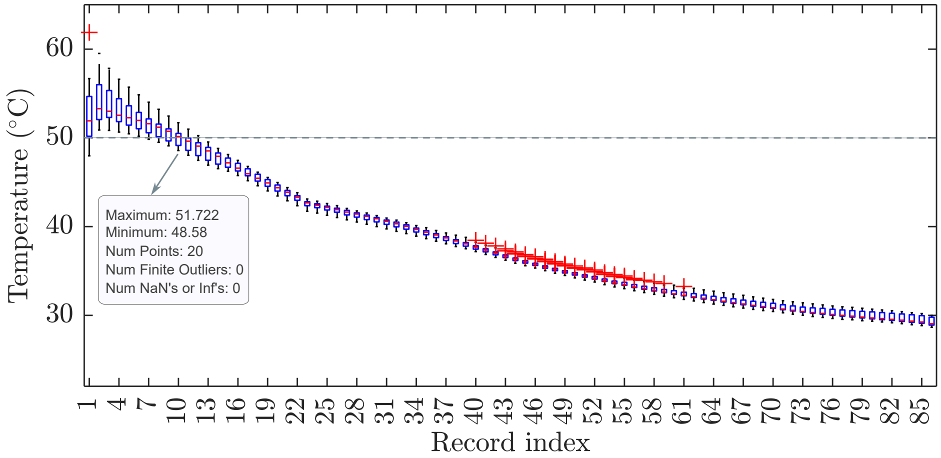

Figure 4.8: Temperature record during the experimental data collection process, along with statistical features calculated from the 20 thermocouple sensors. The central line within the box represents the median, while the lower and upper edges of the box correspond to the 25th and 75th percentiles, respectively. The whiskers stretch to the furthest data points that are not outliers, and any outliers are marked individually with a red '+' symbol.

Four typical T(0,1) time trace signals collected at four different temperatures (52.70 °C, 42.10 °C, 36.08 °C, and 31.74 °C) are shown in Figure 4.9. In the figure, the T(0,1) reflections from the pipe end and the coherent noise are compared. A clear increase in ToF and a decrease in the amplitude of the T(0,1) pipe end reflection with increasing temperature can be observed, indicating changes in material properties and wave velocities, as well as transducer performance. Additionally, the change in the coherent noise component does not follow a consistent pattern with increasing temperature, potentially leading to high residual signals for damage detection even with temperature compensation techniques.

4.3.1.2 Estimation of material properties

The shear wave velocity and longitudinal wave velocity estimated at varying temperatures are presented in Figure 4.10, along with the corresponding linear regression fits that describe the relationship between temperature and

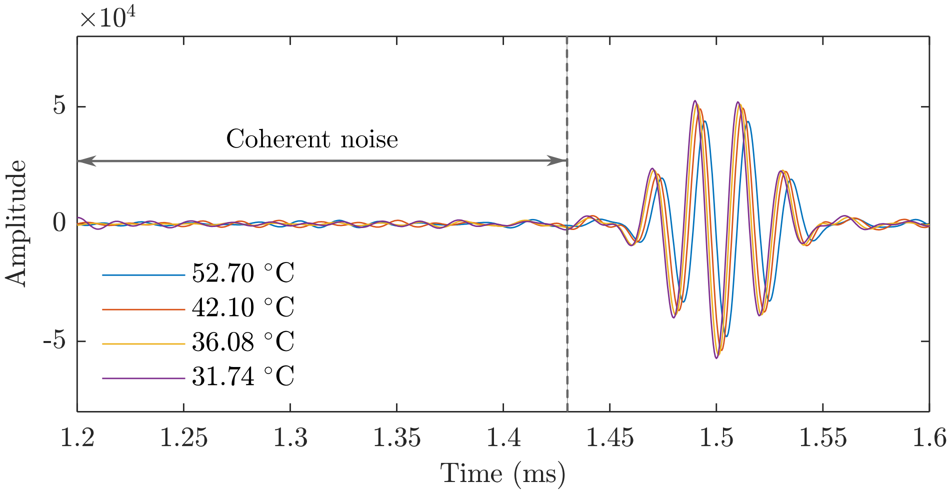

Figure 4.9: Four typical T(0,1) time trace signals collected at four different temperatures, with amplitudes on a comparable arbitrary scale.

wave velocities. The change in shear wave velocities with temperature is approximately 0.48 m/s/°C, which is close to the value reported in [55]. The estimation of shear wave velocity shows a small prediction interval and narrow confidence bounds, whereas the estimation of longitudinal wave velocity exhibits larger variations, as indicated by a broader prediction interval and wider confidence bounds. As discussed in Section 4.2.2.1, the wave packets used for estimating longitudinal wave velocity are likely to be mixed with different wave modes due to mode conversions and reverberations of flexural modes, leading to a larger error in the estimation of longitudinal wave velocities. Additionally, the amplitude of the wave packets used for shear wave velocity and longitudinal wave velocity estimation can be compared from Figures 4.2a and 4.4a, respectively, which are extracted from the same full-matrix data set. The amplitude of the wave packets for shear wave velocity estimation in Figure 4.2a is significantly higher than that for longitudinal wave velocity estimation in Figure 4.4a, resulting in a higher SNR and consequently more accurate wave velocity estimation.

To evaluate the accuracy of longitudinal wave velocity estimation, the es-

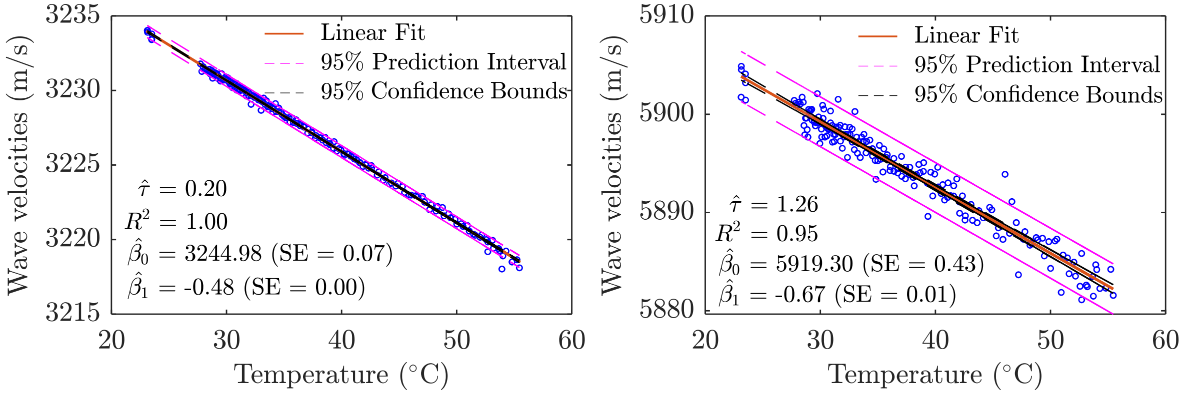

(a) (b)

Figure 4.10: The estimated shear wave velocity and longitudinal wave velocity at varying temperatures, along with the corresponding linear regression fits that describe the relationship between temperature and wave velocities. (a) Estimated shear wave velocities based on the T(0,1) mode. (b) Estimated longitudinal wave velocities based on the F(2,3) mode. Key regression parameters are displayed in the figure, including slope ($\hat{\beta}_1$), intercept ($\hat{\beta}_0$), standard error (SE), residual error ($\hat{\tau}$), and coefficient of determination (R^2).

timation based on L(0,2) mode signals is used for validation. As shown in Figure 2.2, the L(0,2) wave is nearly non-dispersive, and its phase velocity is primarily determined by the longitudinal wave velocity. L(0,2) waves were excited and collected at different temperatures by adjusting the alignment of the transducer elements from the circumferential direction to the axial direction. With this excitation configuration, only L(0,1) and L(0,2) modes propagate in the axial direction of the pipe, each with distinct group wave velocities that allow L(0,2) to be easily separated in the time domain with high purity. Figure 4.11a presents an example of L(0,n) family waves from the simulation. For the estimation of longitudinal wave velocity, the first and third L(0,2) pipe end reflections were windowed using a Tukey window. The higher amplitude of L(0,2) wave packets compared to those of the F(2,3) mode, as shown in Figure 4.4a, ensures a better SNR, thereby resulting in

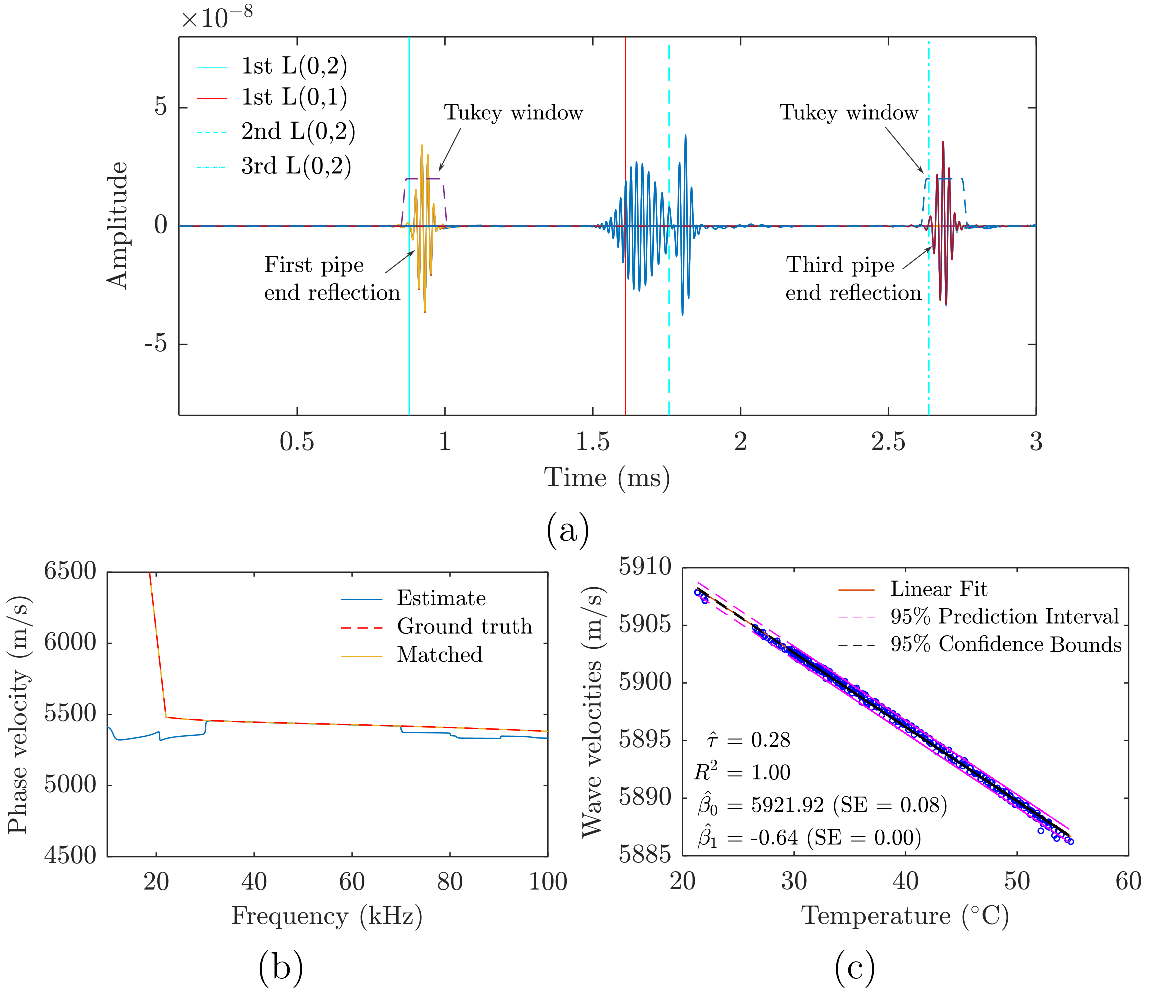

(a)

(b)

(c)

Figure 4.11: Estimation of the longitudinal wave velocity based on the L(0,2) wave packets reflected from a pipe feature. (a) The first and third L(0,2) pipe end reflections, windowed using a Tukey window for the estimation of the L(0,2) dispersion curve. (b) Comparison between the estimated L(0,2) dispersion curve (blue line), the matched dispersion curve determined by the interaction, and the dispersion curve calculated using the ground truth longitudinal wave velocity. (c) The longitudinal wave velocity estimated at varying temperatures, along with the corresponding linear regression fits.

higher accuracy in longitudinal wave velocity estimation.

The same interaction procedure described in Section 4.2.2.1 was used to determine the longitudinal wave velocity from the dispersion curve of the L(0,2) wave mode, estimated based on the extracted L(0,2) wave packets. Figure 4.11b presents the estimated L(0,2) dispersion curve (blue line), which is compared to the matched dispersion curve determined by the interaction and the dispersion curve calculated using the ground truth longitudinal wave velocity. The iteration results closely align with the ground truth dispersion curve of the L(0,2) wave mode. In this case, the estimated longitudinal wave velocity is 5986.43 m/s with an error of 0.03%, compared to the ground truth longitudinal wave velocity of 5988.3 m/s. The longitudinal wave velocity estimated at varying temperatures, along with the corresponding linear regression fits, is presented in Figure 4.11c. The longitudinal wave velocity estimated at different temperatures predicted from the linear model based on the L(0,2) mode and the F(2,3) mode are compared in Table 4.1. It can be seen that the results predicted by the linear model regressed based on the F(2,3) mode have a very small error within 0.075% in the prediction of longitudinal wave velocity, although the original estimated longitudinal wave velocity data has large variability.

Table 4.1: The comparison of the longitudinal wave velocity estimated at different temperatures predicted from the linear model based on the L(0,2) mode and the F(2,3) mode.

Temperature (°C)	20	30	40	50	60
F(2,3)-based velocity estimation (m/s)	5905.90	5899.20	5892.50	5885.80	5879.10
L(0,2)-based velocity estimation (m/s)	5909.12	5902.72	5896.32	5889.92	5883.52
Error (%)	0.055	0.060	0.065	0.070	0.075

4.3.1.3 Estimation of transducer performance

The transducer performance at different temperatures was estimated based on the full-matrix dataset, where the signals were summed from the excitation side to form the CSM data. The transfer function of each individual transducer was then estimated following the procedure detailed in Section 4.2.2.2. The effect of temperature on transducer performance, particularly the frequency spectra of the transducer transfer functions at different temperatures, is presented in Figure 4.12. Figures 4.12a and 4.12b show the frequency response of two transducer channels, Channel 15 and Channel 30, out of 40 transducer channels. The graph colours represent the temperature, with measurements collected at higher temperatures plotted in yellow and those at lower temperatures in black. A gradual change in transducer performance with temperature is observed, corresponding to the gradual change in T(0,1) amplitude at different temperatures in the time domain, as shown in Figure 4.9. Additionally, for the same transducer, the frequency response maintains a similar spectrum, though variations are observed across different transducer channels, which indicates the imbalance of the transducer performance.

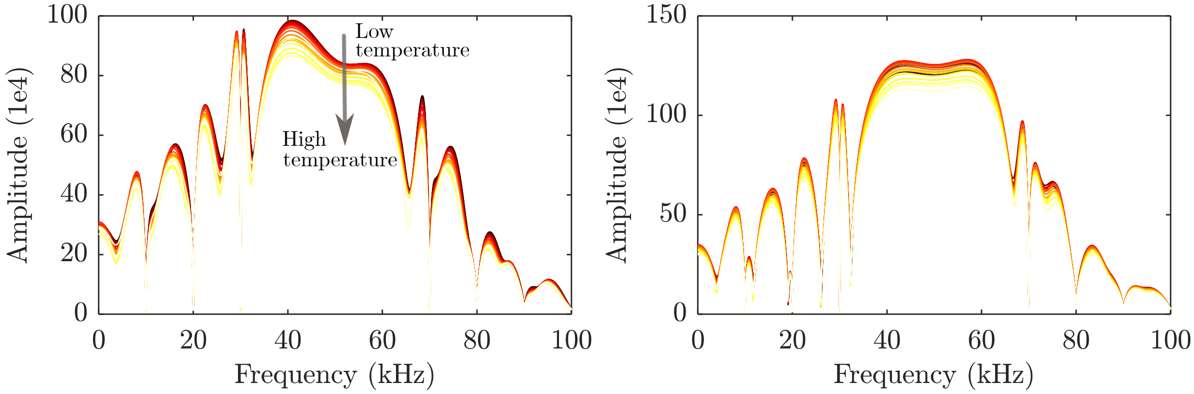

(a)

(b)

Figure 4.12: The effect of temperature on transducer performance, particularly the frequency spectra of the transducer transfer functions at different temperatures, which is shown on a comparable arbitrary scale. (a) Frequency response of transducer Channel 15. (b) Frequency response of transducer Channel 30.

The transducer performance of these two channels at frequencies around the central frequency, 50 kHz, is compared in Figure 4.13. For transducer Channel 15, the response at different frequencies decreases with increasing temperature, while for transducer Channel 30, the influence of temperature on the transducer response is not monotonic, reaching a peak response at around 37.5 °C. This may be due to changes in the coupling of the individual transducer with temperature variations. Additionally, temperature has a uniform influence on the response at different frequencies within the frequency range of interest.

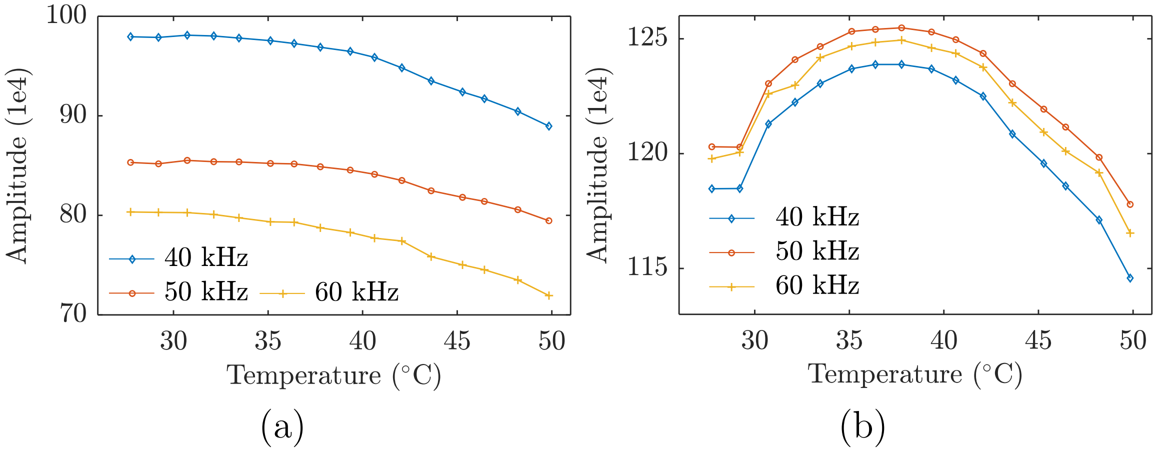

Figure 4.13: The influence of temperature on transducer performance at different frequencies (40 kHz, 50 kHz, and 60 kHz) around the central frequency of 50 kHz, which is shown on a comparable arbitrary scale. (a) Frequency response of transducer Channel 15. (b) Frequency response of transducer Channel 30.

4.3.1.4 Estimation of random noise

The characteristics of random noise at room temperature have been discussed in Section 2.3.2.3, showing that random noise can be modelled as Gaussian white noise with a limited bandwidth and that its RMS level is channel-dependent. In this section, the influence of temperature on the random noise level is analysed in terms of RMS and SNR. This analysis is based on the long-duration full-matrix dataset, where signals are summed from the excitation side to acquire the CSM data.

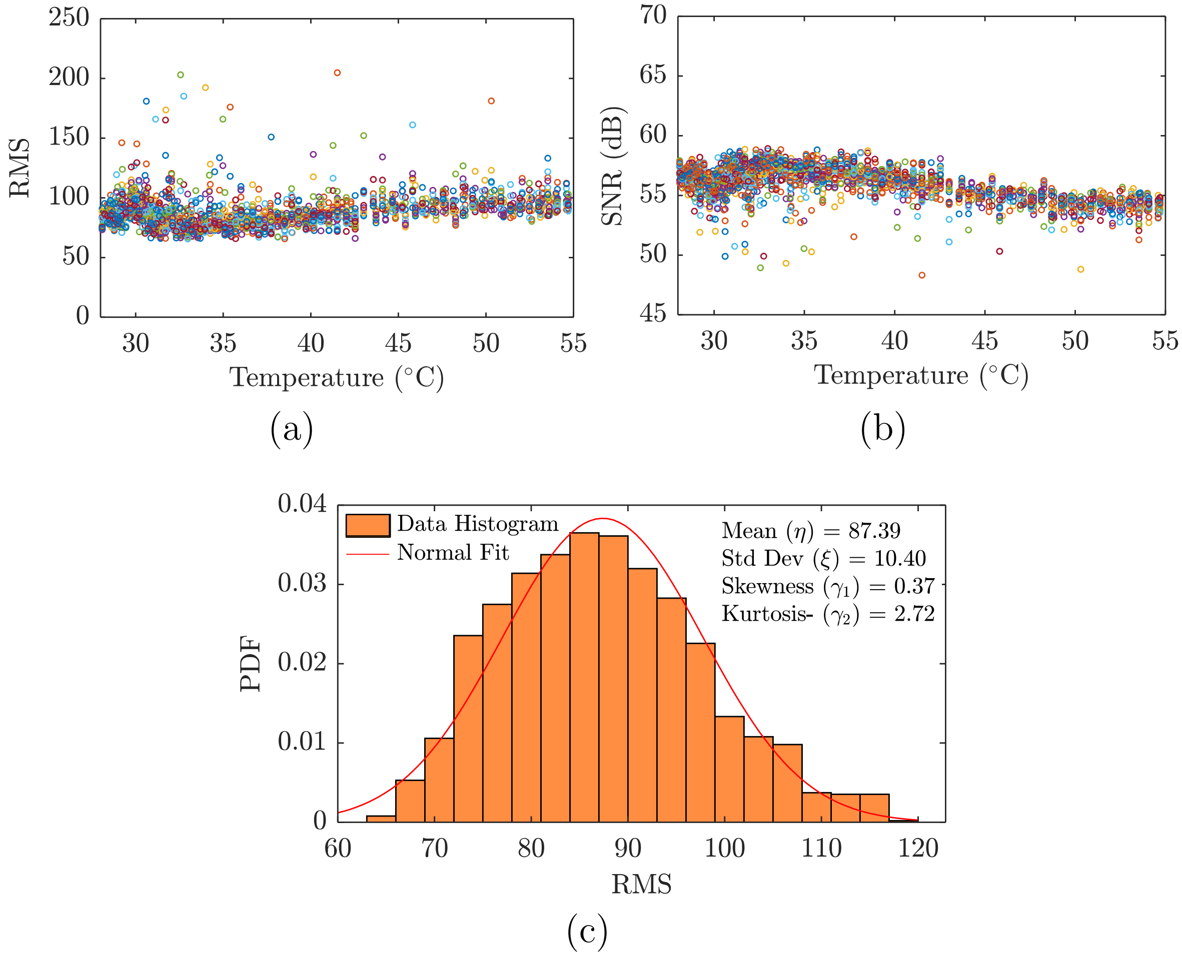

(a) (b)

(c)

Figure 4.14: The influence of temperature on random noise levels. (a) The scatter plot of RMS levels of random noise signals from 40 transducer channels at different temperatures. (b) The scatter plot of SNR levels of random noise signals. (c) Statistical distribution of the RMS level of random noise from all signals at different temperatures.

Figure 4.14 shows the scattering of the RMS and SNR levels of all random noise signals from 40 transducer channels at different temperatures. The RMS values represent the absolute amplitude of the random noise measured directly from the experimental signals, whereas the SNR values are calculated by comparing the RMS noise level to the peak amplitude of the corresponding T(0,1) wavepacket, similarly to Eq. 3.11. Since the T(0,1) peak amplitude is significantly higher (typically around 5.4×10^4) and varies with temperature, the SNR values appear higher than would be inferred directly from the noise RMS values alone.

In Figure 4.14a and Figure 4.14b, it can be seen that the RMS level of the random noise does not change with temperature, whereas the SNR level decreases with increasing temperature due to the decrease in T(0,1) signal amplitude. This result indicates that the random noise level, in terms of RMS, is unaffected by temperature. Consequently, when transducer performance degrades due to environmental conditions, the overall SNR level of the signal decreases, leading to worse performance in damage detection. This is important to consider when the degradation of transducer performance is significant. It should be noted that the full-matrix dataset used for random noise analysis here was not averaged for a clearer illustration of random noise. The SNR levels depicted in Figure 4.14b can be improved by $10 \log_{10} M$ dB through signal averaging, where M is the number of averages, as discussed earlier.

Figure 4.14c presents the statistical distribution of the RMS level of the random noise from all signals at different temperatures. The distribution is fitted with a normal distribution, and the corresponding fitting parameters are shown in the figure. Since the RMS level of random noise does not change with temperature, these statistical parameters of the RMS distribution are used to generate Gaussian white noise for each transducer channel in the digital twin model for the modelling of random noise.

4.3.1.5 Data generation

In this section, the performance of the established digital twin model is evaluated by comparing the digital twin-generated T(0,1) guided wave signals with experimental data. This comparison includes both undamaged signals at various temperatures and damaged signals at room temperature.

Undamaged cases with temperature variations

The material properties, transducer performance, and random noise levels at four distinct temperatures (29.26 °C, 35.76 °C, 40.22 °C, and 45.50 °C) are estimated based on previously discussed techniques. Corresponding digital twin models are then established to generate T(0,1) signals at these temperatures.

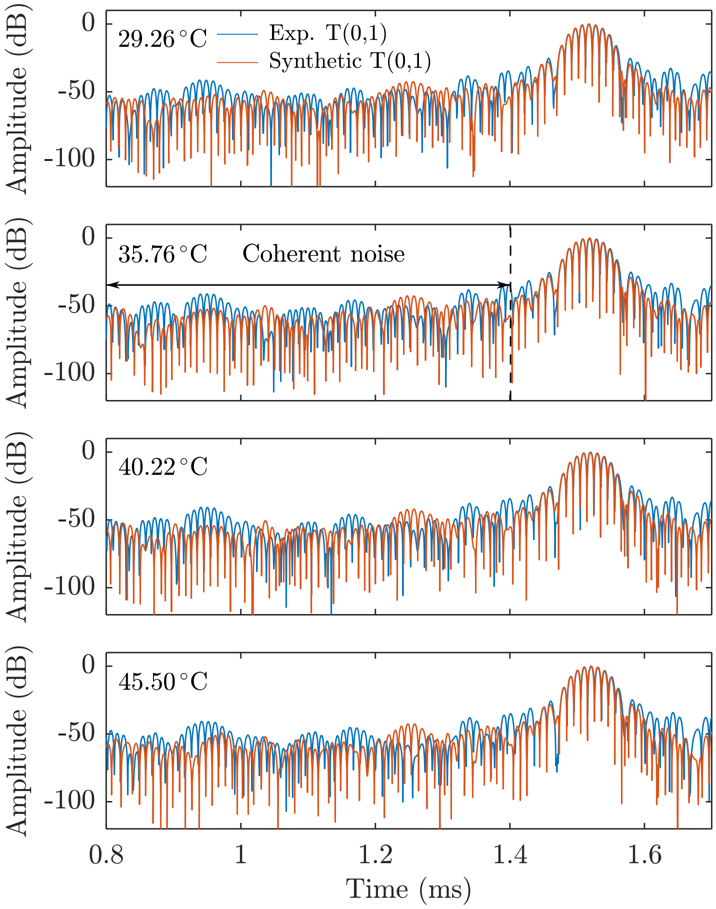

Figure 4.15: Comparison of the digital twin synthetic signals with experimental signals at different temperatures. The temperature at which the experimental data was acquired is shown at the top left corner of the plot.

Figure 4.15 compares the digital twin synthetic signals with experimental signals at different temperatures. The comparison shows a high level of agreement in both the ToF and the waveform of the T(0,1) pipe end reflection between simulation and experiment at each temperature, indicating that the model parameters were accurately estimated. The maximum time difference in the arrival of the T(0,1) wavepacket between the synthetic and experimental signals is within 0.001 ms across all cases. In terms of coherent noise level, the synthetic signals consistently exhibit values approximately 4 dB higher than the experimental ones across all temperatures. This difference is likely due to real-world imperfections not captured in the digital twin model, such as material anisotropy and geometric irregularities in the tested pipe, as discussed in Section 3.4.1.2. Nevertheless, the relative noise levels across different temperatures and key noise features are well represented, supporting the validity of the synthetic data for subsequent reliability estimation.

Defective cases at room temperature

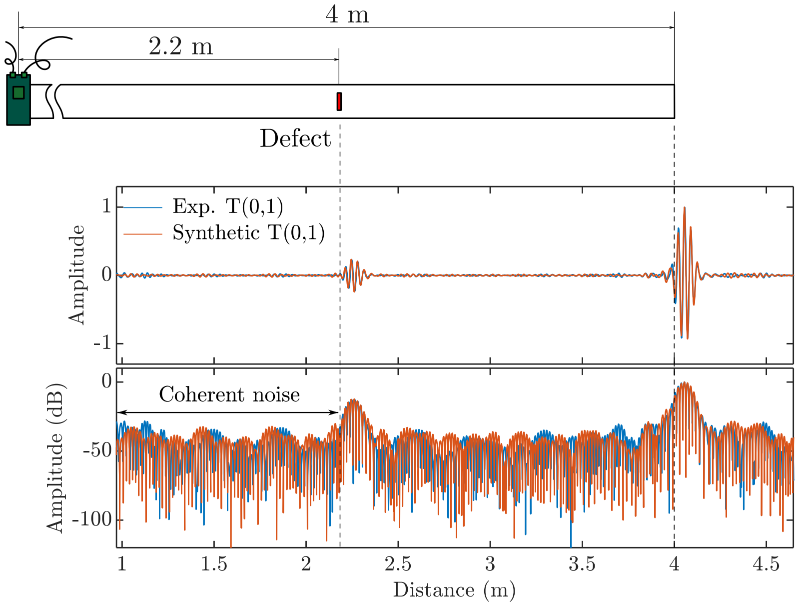

Figure 4.16: Schematic of the examined pipe with a defect and comparison between the digital twin synthetic signal and the experimental signal on both linear and logarithmic scales. The signals are normalised using the amplitude of the T(0,1) wave packet reflected from the pipe end.

Parameter	**Value**
Shear wave velocity (m/s)	3233.640
Longitudinal wave velocity (m/s)	5903.047
Elastic modulus (GPa)	211.05
Poisson's ratio	0.2856
Density (kg/m^3)	7850
Length (m)	4
Outer diameter (mm)	219.1
Inner diameter (mm)	198.48
Thickness (mm)	10.31
Notch location (centre to pipe end)	1800
Notch circumferential length (mm)	280
Notch width (mm)	4
Notch depth (mm)	5.3

Table 4.2: Geometrical dimensions of the examined pipe with a defect, including the location and size of the notch defect, and detailed material properties estimated from experimental measurements.

Defect modelling is an essential part of the digital twin model for POD analysis. To assess the digital twin model's accuracy in replicating scenarios with defects, experimental signals from a defective pipe were collected for comparison. As shown in Figure 4.16, an 8-inch Schedule 60 steel pipe with a length of 4 metres was used in the experiment. The geometrical dimensions of the pipe, the location and size of the notch defect, and the detailed material properties estimated from the experimental measurements are listed in Table 4.2.

The digital twin synthetic signal is compared with the experimental signal on both linear and logarithmic scales in Figure 4.16. The good agreement in the coherent noise level, the ToF and the waveform of the defect reflection and pipe end reflection indicate that the established digital twin model can generate signals for defective cases with high fidelity. This close match with the experimental measurements promises accurate reliability estimation based on the digital twin model.

4.3.2 Commercial transducer ring validation

In this section, the proposed method for establishing the digital twin model is tested on commercial-quality guided wave signals using a commercial transducer ring from GUL, which has been widely applied in the pipeline industry.

4.3.2.1 Experimental setup

The data was collected at GUL from a 6-metre length of 8-inch Schedule 40 carbon steel pipe, with a nominal external diameter of 219.1 mm and a wall thickness of 8.18 mm, as shown in Figure 4.17a. The pipe was heated using a heating element placed in its centre, and an insulation jacket was installed outside the pipe to maintain a more uniform temperature and slow down temperature decay. The pipe was heated up to 100 °C and then allowed to cool naturally, during which data was collected at 15-minute intervals.

In the experiment, eight thermocouple sensors were equally spaced around the pipe circumference to monitor the temperature distribution. According to the recorded temperature variations, the maximum temperature difference around the pipe circumference within the temperature range of interest (between room temperature and 60 °C) was approximately 4.8 °C. Unlike the laboratory setup, this setup did not have a temperature control system, and the thermocouples were installed at a single location next to the transducer ring on the pipe. Therefore, non-uniform temperature distribution may exist, potentially contributing to errors in the data analysis.

A commercial guided wave transducer ring, Permanently Installed Guided Wave Monitoring (gPIMS), shown in Figure 4.17b, was installed on the pipe 2 m from one of the pipe ends. In the experiments, two gPIMS were installed for other tests as shown in Figure 4.17a. For this study, the transducer

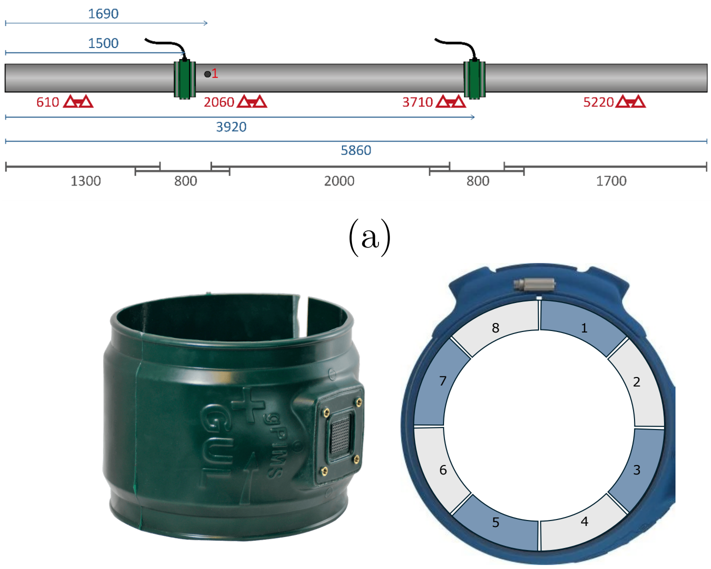

(a)

(b) (c)

Figure 4.17: Experimental setup to collect commercial-quality guided wave signals using a commercial guided wave transducer ring from GUL. (a) Schematic of the examined pipe and the installation of the transducer ring. (b) A commercial guided wave transducer ring, gPIMS, developed by GUL. (c) Transducer elements grouped into eight channels, with three or four transducer elements per channel.

ring on the right-hand side was used. Similar to the transducer ring used in the laboratory experiments, the gPIMS transducer ring consists of 26 transducer elements. However, in this commercial ring, the transducer elements are grouped into eight channels, with three or four transducer elements per channel, as shown in Figure 4.17c. This means that the input and output from several transducer elements are averaged, and therefore, transducer performance is estimated based on signals from individual channels.

Measurements were made using an 8-cycle Hann-windowed toneburst at five central frequencies: 17 kHz, 21 kHz, 25.5 kHz, 31 kHz, and 37 kHz, with a sampling frequency of 200 kHz. This study uses data with a central frequency of 37 kHz, as it is closer to the 50 kHz frequency used in laboratory experiments. The signals were processed with a bandpass filter with a lower frequency band of 10 kHz and an upper band of 90 kHz. Data was collected with four-time averaging. The gPIMS transducer ring consists of two rows of transducers for directional control, but in this study, only data from one row was analysed to align with the laboratory setup.

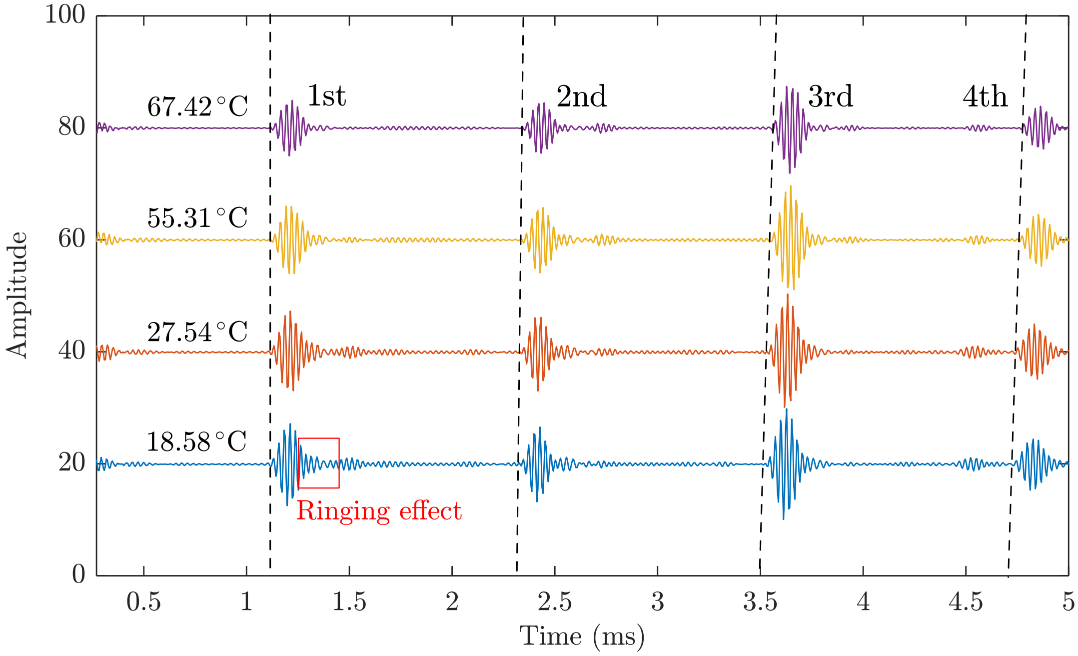

Figure 4.18: Four sample T(0,1) guided wave signals collected at different temperatures: 18.58 °C, 27.54 °C, 55.31 °C, and 67.42 °C. The signal amplitude is shown in arbitrary units and is comparable across the different temperatures.

Figure 4.18 shows four sample T(0,1) guided wave signals collected at different temperatures: 18.58 °C, 27.54 °C, 55.31 °C, and 67.42 °C. Since the gPIMS transducer ring used in this study was installed near the right-hand side pipe end, the first four wave packets shown in Figure 4.18 result from reflections and reverberations from the pipe ends. The signal amplitude is shown in arbitrary units but is comparable between signals collected at different temperatures.

The time delay of the T(0,1) arrivals due to temperature changes is observable, and these delays increase with the wave propagation distance. Additionally, the amplitude of T(0,1) reflections and reverberations decreases with increasing temperature, likely due to changes in the coupling condition of transducers and the adhesive layer bond of piezo elements. Notably, the tail of the T(0,1) wave packets and the high coherent noise level between two T(0,1) wave packets are more pronounced at lower temperatures. This effect, known as the ringing effect, is due to the resonance of the transducer ring when the system operates near its resonance frequency [34]. This phenomenon was also reported in a study by Heinlein et al. [157] using a similar gPIMS transducer from GUL, where the resonance of the transducer ring shifted away from 37 kHz as the temperature increased from 25 °C (room temperature) to 50 °C. This explains why the ringing effect is less pronounced at higher temperatures, resulting in a less obvious tail after the T(0,1) wave packets.

4.3.2.2 Estimation of material properties

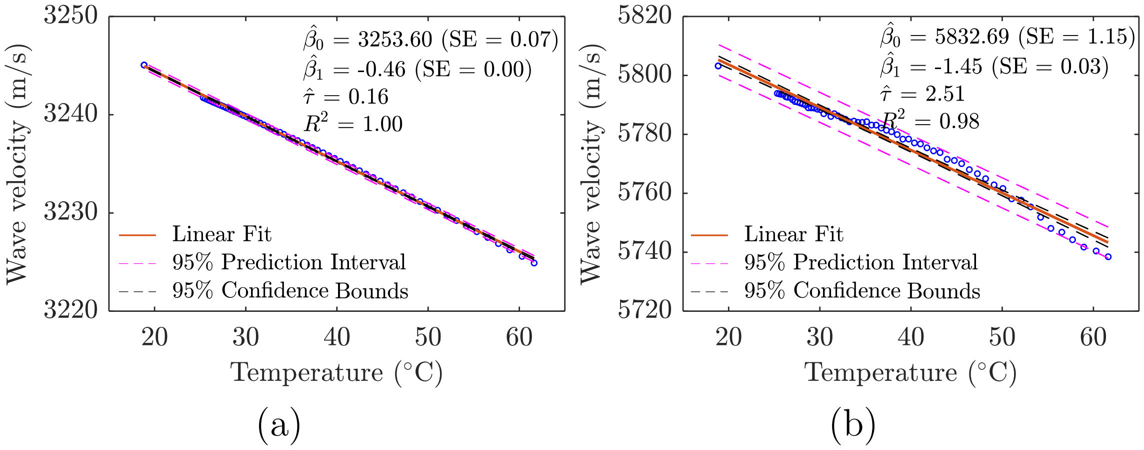

(a) (b)

Figure 4.19: Estimated shear wave velocity and longitudinal wave velocity from 18.58 °C to around 60 °C, along with the corresponding linear regression parameters. (a) Estimated shear wave velocities. (b) Estimated longitudinal wave velocities.

Following the steps to establish the digital twin model, the material properties of the examined pipe were first estimated based on the experimental data collected at different temperatures using the commercial transducer ring. Figure 4.19 presents the estimated shear wave velocity and longitudinal wave velocity from 18.58 °C to around 60 °C, along with the corresponding linear regression parameters. It can be observed that the relationship between wave velocities and temperature follows a linear trend within the temperature range of interest, consistent with the laboratory tests. The rates of change for shear wave velocity and longitudinal wave velocity with temperature are -0.46 m/s/°C and -1.45 m/s/°C, respectively. These values differ slightly from the measurements obtained from the pipe used in the laboratory experiments, which are -0.48 m/s/°C and -0.67 m/s/°C. This difference in the coefficients may be attributed to material variations due to the different manufacturing processes of the examined pipes.

4.3.2.3 Estimation of transducer performance

Once the material properties are estimated at each temperature, the transducer performance is analysed based on the signals from each channel, which correspond to three or four transducer elements wired together, following the procedure detailed in Section 4.2.2.2. The transducer performance in the frequency domain at different temperatures from channel 4 and channel 8 are compared in Figure 4.20. The temperature of the collected data is indicated by different colours, with black representing lower temperatures and yellow representing higher temperatures.

It can be observed that the differences in the frequency spectrum between transducer channels are smaller than those from the laboratory data collection, as shown in Figure 4.12. This may be due to the fact that the data collected from a single channel are the averaged signals from several transducer elements, thus reflecting less variation in the performance of individual transducers.

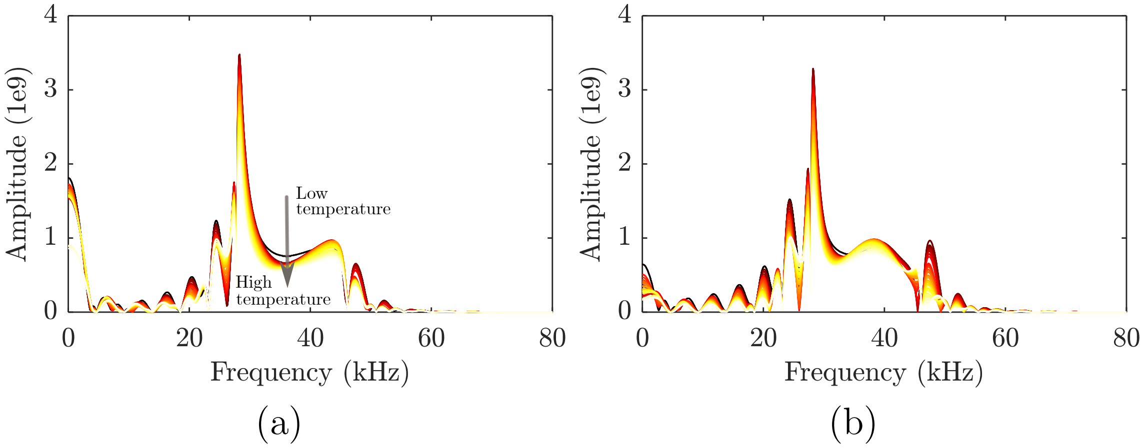

Figure 4.20: Transducer performance in the frequency domain at different temperatures for channels 4 and 8. (a) Transducer performance from channel 4 at varying temperatures. (b) Transducer performance from channel 8 at varying temperatures.

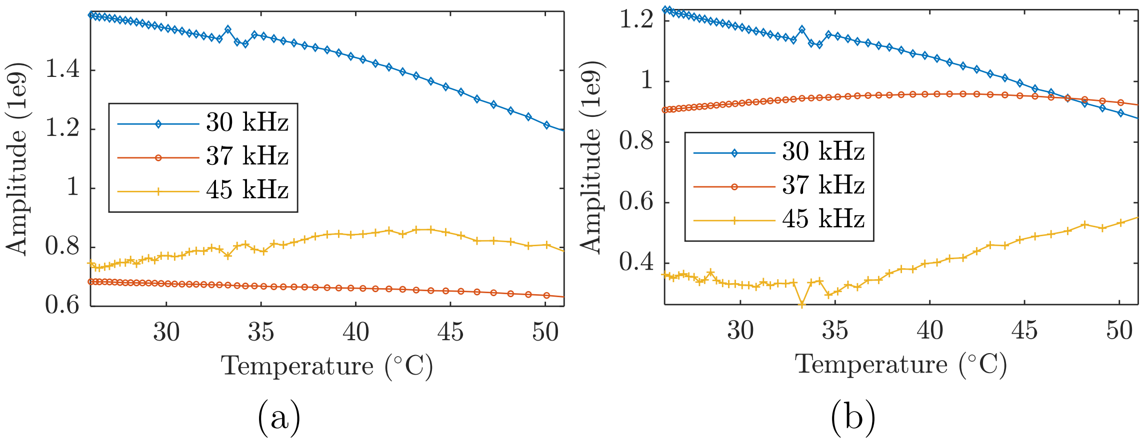

Figure 4.21: Changes in the transducer performance with temperature at three frequencies around the central frequency of 37 kHz. (a) Transducer performance of channel 4. (b) Transducer performance of channel 8.

Additionally, the change in the transducer performance with temperature at three frequencies around the central frequency of 37 kHz is compared in Figure 4.21 for transducer channels 4 and 8. Unlike the case for the transducer ring used in the laboratory experiments shown in Figure 4.13, temperature variations have different effects on the signal at different frequency components. This may be due to the shift in the resonance frequency when temperature changes, as reported in Heinlein's thesis (Figure 7.13, page 119 [157]) on a similar gPIMS transducer ring. In the data collected from the transducer ring used in the laboratory environment, the frequency spectrum of the transducer performance was only tested within the frequency range near the central frequency of 50 kHz. Within this frequency range, no resonance of the transducer ring was observed, and the influence of temperature variations on transducer performance was consistent for all frequency components of interest.

4.3.2.4 Estimation of random noise

In the dataset collected from the gPIMS transducer ring, random noise was recorded from the transducer channels when there was no excitation. The RMS of the random noise at different excitation frequencies and various temperatures is shown in Figure 4.22a, with the scatter colour representing data from datasets with different excitation frequencies. It can be observed that the random noise level varies within a certain range but is not affected by temperature and remains consistent across all datasets.

Similarly to the random noise collected from the transducer ring used in the laboratory environment, the statistical characteristics of the RMS of the random noise were analysed for modelling the random noise in the digital twin model. Figure 4.22b shows the distribution of the RMS level of the random noise, fitted with a normal distribution. The corresponding estimated normal distribution parameters are displayed in the figure, showing a mean value of 1.95×10^{-4} and a standard deviation of 0.13×10^{-4}. Additionally, the skewness and kurtosis are calculated as -0.11 and 2.64, respectively. These estimated parameters of the RMS distribution of the random noise were used to generate Gaussian white noise in the digital twin model.

4.3.2.5 Data generation

Based on the estimated model parameters, including material properties, transducer performance, and random noise, a digital twin simulation model was established. This model allows the generation of T(0,1) guided wave signals at different temperatures. Figure 4.23 shows the T(0,1) signals corresponding to four temperatures. Similar to Figure 4.18, the amplitude of the signal is shown in arbitrary units, and the decay of the signal amplitude with increasing temperature can be observed from the digital twin-generated signals. Additionally, the time delay between the T(0,1) wave packets is consistent with that in the experimental signals shown in Figure 4.18. Co-

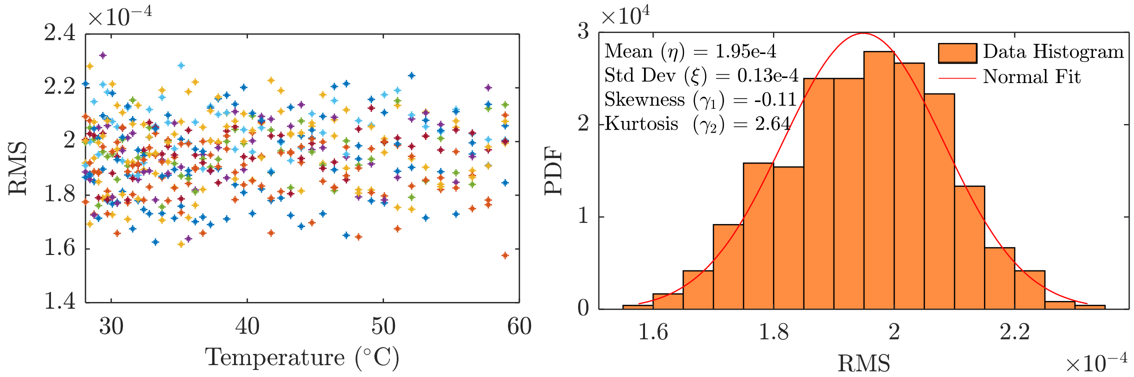

(a) (b)

Figure 4.22: Random noise analysis of the guided wave signals collected from the gPIMS transducer ring at varying temperatures. (a) RMS of the random noise at different excitation frequencies and various temperatures, with scatter colour representing data from datasets with different excitation frequencies. (b) Distribution of the RMS level of random noise, along with a normal distribution fitting and corresponding estimated parameters.

herent noise resulting from the imbalance of the transducer performance is also visible in the digital twin-generated data.

Compared with experimental data collection, the coherent noise level is lower in the digital twin-generated data for several reasons. In the experiments using the gPIMS transducer ring, several transducer elements are wired together, which reduces the accuracy in estimating the transducer performance due to individual coupling conditions. Furthermore, in the experimental data, part of the coherent noise between two T(0,1) wave packets is caused by reverberations between the installed transducers, supports, and pipe ends. However, for simplicity, the installed transducer rings and supports are not modelled in the digital twin. Additionally, the ringing effect due to the resonance of the transducer ring is not included in the digital twin model. Therefore, the T(0,1) wave packets at lower temperatures are less comparable to experimental signals than those at higher temperatures due to a strong

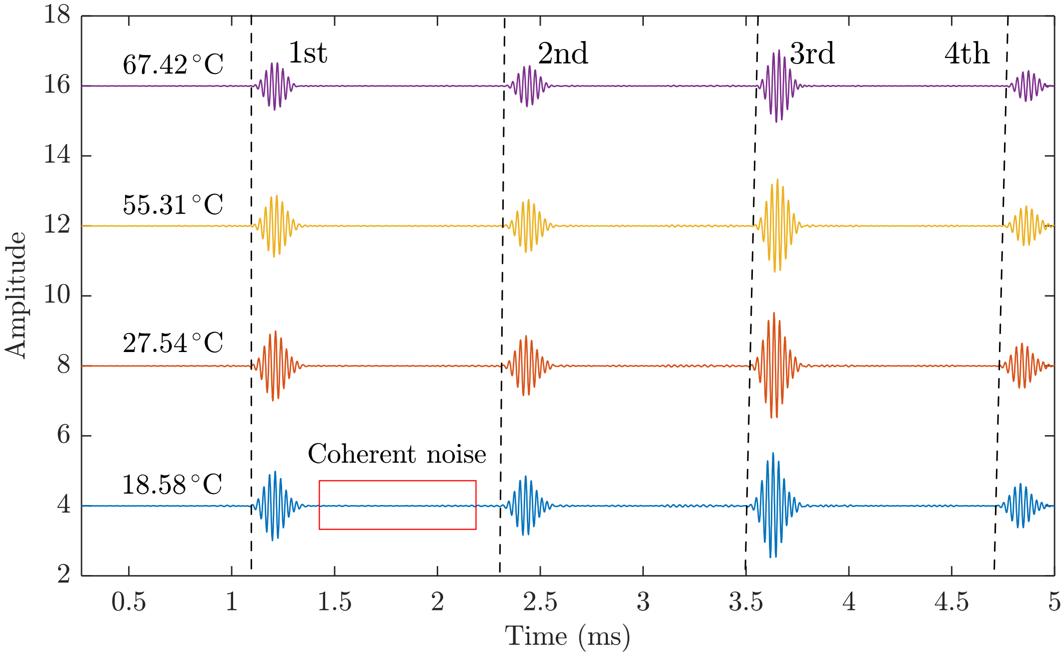

Figure 4.23: Digital twin-generated T(0,1) signals corresponding to four different temperatures.

ringing effect in the experimental signals at lower temperatures.

4.4 Validation of reliability estimation

In this section, the reliability estimation method based on the digital twin model is validated by comparing the POD analysis with that based on the superposition method proposed by Liu et al. [35] and validated by Heinlein et al. [142]. Specifically, two sets of synthetic data with varying flaw sizes, random temperature variations, and random defect locations are generated for POD analysis, according to the same experimental datasets collected in the laboratory environment, as detailed in Section 4.3.1. Additionally, the characteristics of the digital twin-generated data, in terms of damage signature and residual noise, are analysed.

4.4.1 Validation procedure

A general procedure for performing the POD analysis based on the synthetic data is presented in Figure 4.24, which includes four steps: data generation, temperature compensation, baseline subtraction, and statistical analysis.

Step 1 involves data generation, which is the creation of synthetic datasets that simulate real-world scenarios. Data generation is achieved by the proposed digital twin model and the superposition method, respectively. Various real-world variabilities can be incorporated in this step. In this study, three common and representative variables of interest are incorporated: varying flaw sizes, randomly located defects, and random temperature variations. The configurations of these variables are kept the same for both data generation methods for a fair comparison. In each dataset, three sets of guided wave signals are generated for further analysis: baseline signals, damage signals,

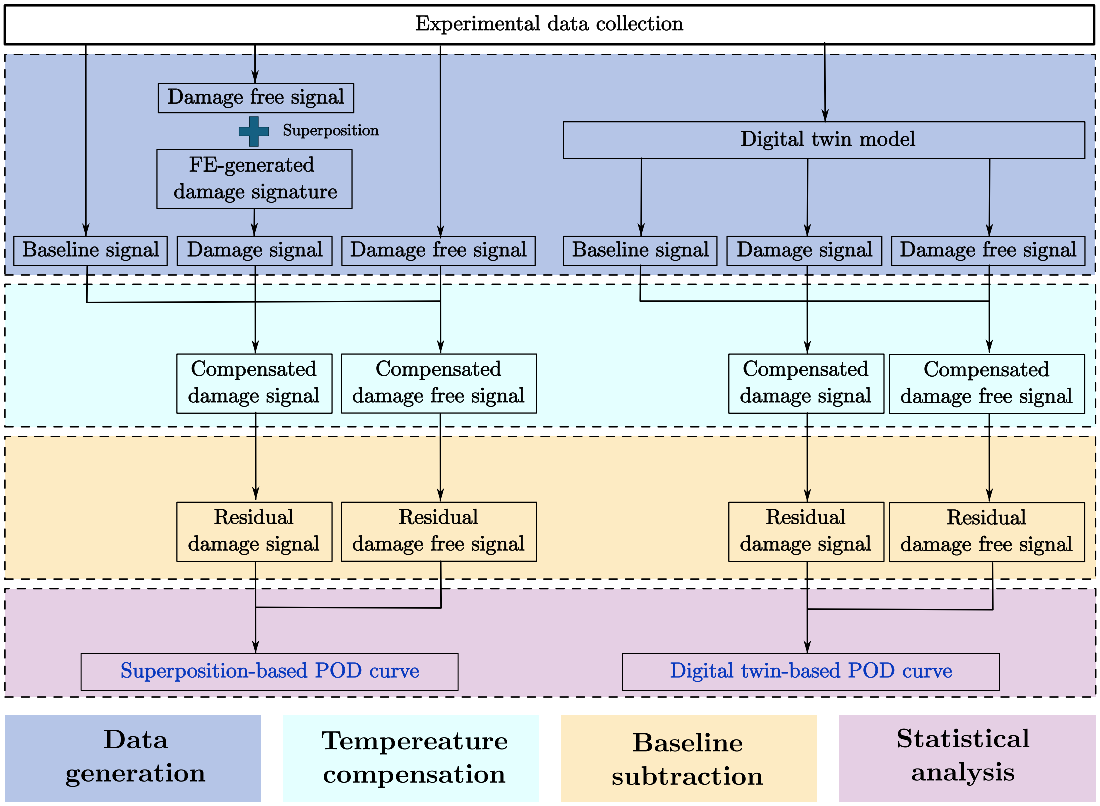

Figure 4.24: A general procedure for performing the POD analysis based on the synthetic data.

and damage-free signals. The temperature is randomly chosen from within the experimental range, from 25 °C (room temperature) to 50 °C. A through-thickness defect with varying circumferential extension is modelled for each case, and its locations are randomly chosen between 1.29 m and 1.94 m to avoid the near field in the experimental signal and overlap with the reflection from the pipe end. The CSC of the defects varies from 0.31% to 3.13%.

In the second step, the damage signals and damage-free signals are processed using the BSS method to eliminate the influence of temperature variations. In the third step, the compensated damage and damage-free signals are subtracted from the baseline signals to obtain the residual damage and damage-free signals, based on which the damage response and the noise level are calculated, respectively. In the last step, the signal response of the residual signals with regard to the flaw size is analysed for further quantitative POD analysis, based on the procedures detailed in Section 4.2.2.5. The POD analysis is then quantitatively compared between the data generated from the proposed digital twin model and that from the verified superposition method.

4.4.1.1 Data generation using superposition

The data generation method based on superposition is detailed in [35]. In this study, the experimental data collected in Section 4.3.1 at different temperatures serve as the undamaged monitoring signals, to which damage signatures are superposed. The damage signatures are generated by FE simulations, where the size and location of the defects are varied to account for the location dependence of the system's damage detection performance. The FE-generated damage feature is normalised by the amplitude of the T(0,1) pipe end reflection in the damage-free case and scaled according to the experimental T(0,1) pipe end reflection onto which it is superposed. In total, 50 sets of datasets are generated, and in each dataset, the flaw size varied from 0.31% to 3.13% with different temperature histories. Figure 4.25a shows an example of synthetic signals with varying flaw sizes at the same location. It can be seen that the defect only affects the area where the damage signature is added, and no reverberations are considered here. For the calculation of the damage signal response, a window with a length of 5-cycle toneburst is applied to the location where the damage is added to extract the signal amplitude.

4.4.1.2 Data generation using digital twin model

To generate synthetic data from the established digital twin model, a random temperature is selected within the range of interest (25 °C to 50 °C).

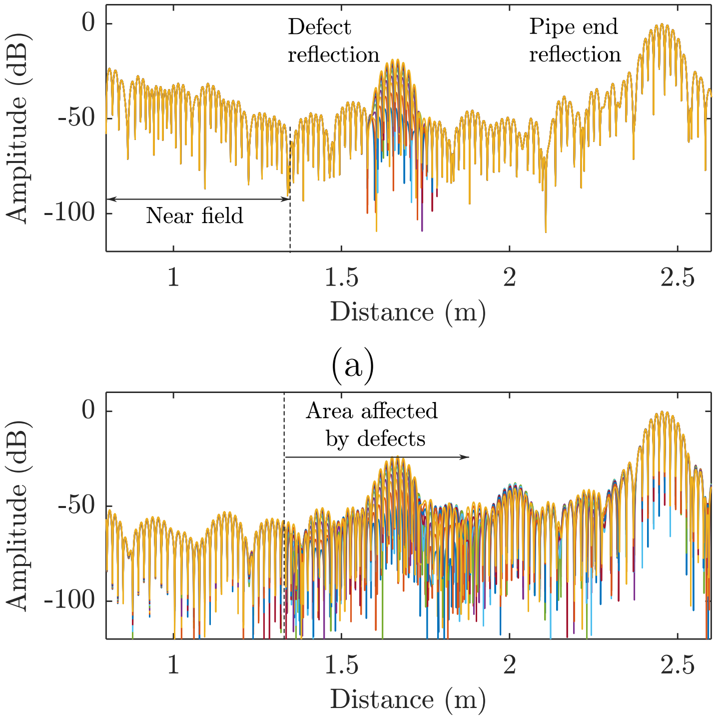

(a)

(b)

Figure 4.25: Synthetic guided wave signals generated at the same temperature but with different flaw sizes, ranging from 0.94% CSC to 10% CSC, at the same location. (a) Signals generated by the superposition method. (b) Signals generated by the digital twin model.

The corresponding material properties, transducer performance, and random noise level are then updated in the digital twin model for different sizes of defects at various locations. Similarly, 50 datasets are generated with varying defect sizes, and in each dataset, the temperature history with increasing defect sizes is different to ensure independence between the datasets.

Figure 4.25b shows the synthetic guided wave signals generated at the same temperature but with different flaw sizes at the same location. It can be seen that the presence of the defect affects a much larger area in the synthetic guided wave signals, which may lead to high residuals over this area. This could potentially result in the misidentification of the damage signal when the location of the defect is unknown.

4.4.2 Reliability estimation comparison

The POD analysis was performed on the synthetic dataset following the procedure detailed in Section 4.2.1. First, the residual signals in the absence of defects were analysed to establish a detection threshold. Figure 4.26 shows the distribution of the residual signal response in the absence of defects using data from the superposition method and the digital twin model, respectively. The residual signal response from the superposition method follows a lognormal distribution, and the threshold corresponding to the 1% PFA is determined from the fitting distribution to be 0.4%. In contrast, the residual signal response generated by the digital twin model fits a normal distribution, with a threshold of 0.2% corresponding to the 1% PFA.

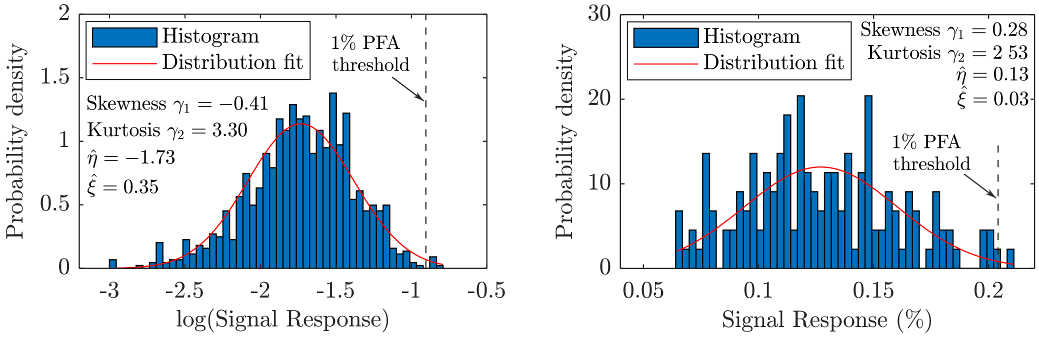

(a) (b)

Figure 4.26: The distribution of the residual signal response in the absence of defects using data from the superposition method and the digital twin model, respectively. (a) Analysis based on data generated by the superposition method. (b) Analysis based on data generated by the digital twin model.

The deviation in the detection thresholds arises from the different distributions of the residual signal responses, which are primarily contributed by coherent noise, imperfect temperature compensation, and random noise. Specifically, the superposition data, which is exactly the original experimental data without any defect signal added, exhibited more uncertainties not accounted for in the digital twin model. Consequently, temperature compensation was less effective for the superposition data, leading to higher residual signal values compared to those from the digital twin-generated data. This deviation in signal response between the superposition and digital twin-based data is consistent across all datasets, both in scenarios with and without defects. Referring to the formula for POD in Eq. (3.18), this deviation exists both in $\hat{a}_0$ and $(\beta_0 + \beta_1 a_i)$; therefore, it does do not affect the calculation of POD.

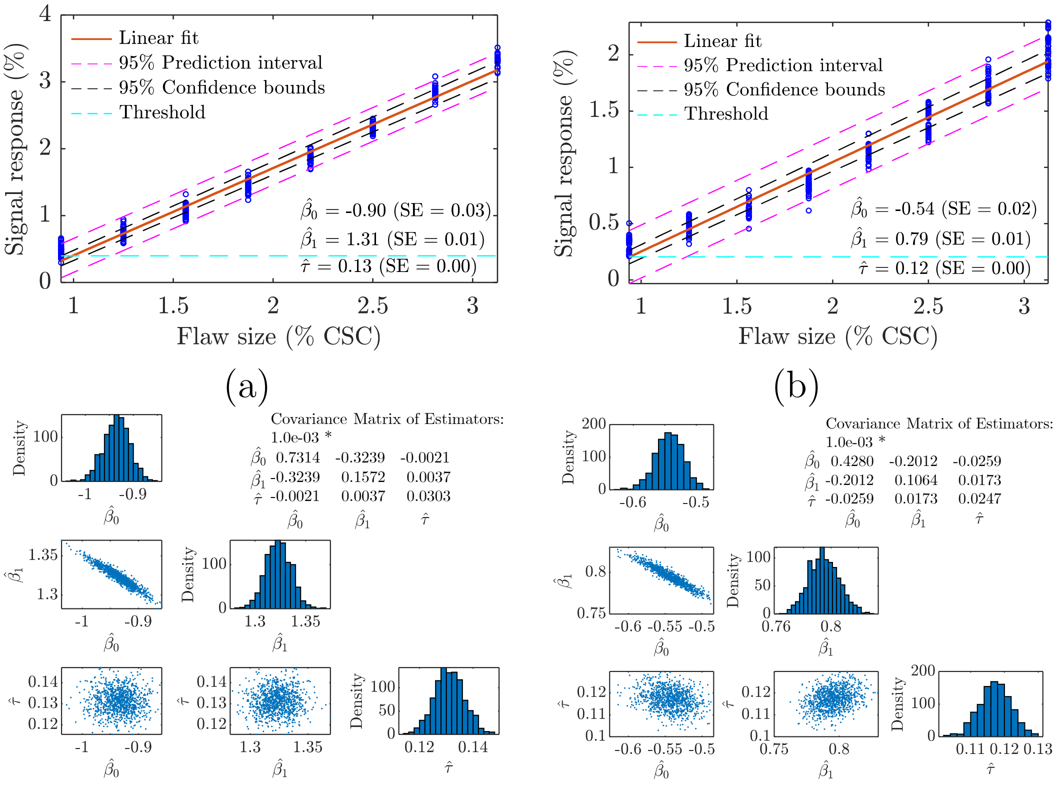

(a) (b)

(c) (d)

Figure 4.27: Linear regression and parameter estimation based on the Bootstrap method. (a) Linear regression using data generated by the superposition method. (b) Linear regression using data generated by the digital twin model. (c) Distribution of the estimated parameters and the covariance matrix of estimators based on data generated by the superposition method. (d) Distribution of the estimated parameters and the covariance matrix of estimators based on data generated by the digital twin model.

The relationship between damage response and varying flaw sizes was analysed using the bootstrapping method, with the results and estimated parameters displayed in Figure 4.27. This analysis confirmed the linear relationship between the damage response and flaw sizes, supporting the linearity assumption in POD analysis. Additionally, scatter plots of the estimated parameter pairs — slope ($\hat{\beta}_1$) and residual error ($\hat{\tau}$), intercept ($\hat{\beta}_0$) and residual error ($\hat{\tau}$) — along with the low covariance matrix values $\sigma_{\beta_0\tau}$ (element $(3,1)$) and $\sigma_{\beta_1\tau}$ (element $(3,2)$), confirmed the independence of the data generated in both cases.

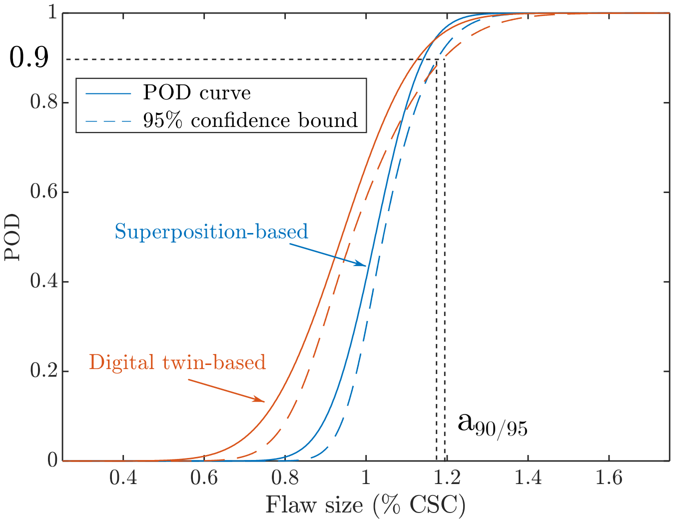

Figure 4.28: Comparison of the POD curves and the corresponding 95% confidence intervals calculated from data generated by the superposition method and the digital twin model.

Figure 4.28 compares the POD curves and the corresponding 95% confidence bounds calculated from the two sets of data. The slight differences in the scale of the POD curves are due to variations in the estimated parameters. The parameter β_1 describes how the signal response changes with increasing flaw sizes. The estimated β_1 from the digital twin data is lower than that from the superposition data, indicating a lower overall response from defects in the digital twin-generated data. This discrepancy is primarily due to imbalances in transducer performance during excitation and reception, where part of the energy generates flexural wave modes, contributing to coherent noise.

Consequently, the T(0,1) wave mode reflected from the defect and received by the transducers is diminished. Additionally, the threshold value determines the location of the POD curve, and the slight difference between the two detection thresholds leads to differences in the POD curve locations.

As mentioned earlier, in POD analysis, the $a_{90/95}$ value quantifies the flaw size at which the system has 90% POD with 95% confidence, which is of particular interest for quantitative comparison between the POD curves. The $a_{90/95}$ value for the superposition method is 1.18% CSC, while for the digital twin-based data, it is 1.19% CSC. The close proximity of these two estimated $a_{90/95}$ values suggests that the POD analysis based on the digital twin-generated data performs similarly to that based on the data generated by the superposition method.

4.4.3 Discussion

This section discusses the differences between superposition-generated and digital twin-generated guided wave data, with a focus on their respective impacts on the reliability estimation of an SHM system. Particular attention is given to how each method captures wave interactions, especially reverberations caused by co-existing defects, and how these interactions influence the detection of another defects.

Figure 4.29 compares the raw and residual T(0,1) signals produced by both methods. The defect, with a flaw size of 3.125% CSC, is located at the same position in both cases, with the current signal and baseline temperatures set at 37.71 °C and 44.33 °C, respectively. The residual signal is obtained by subtracting the temperature-compensated baseline signal from the current signal. As shown in Figure 4.29a, the reflection from the defect is smaller in the digital twin case due to the presence of coherent noise and reverberations. In the residual signals shown in Figure 4.29b, the region around the

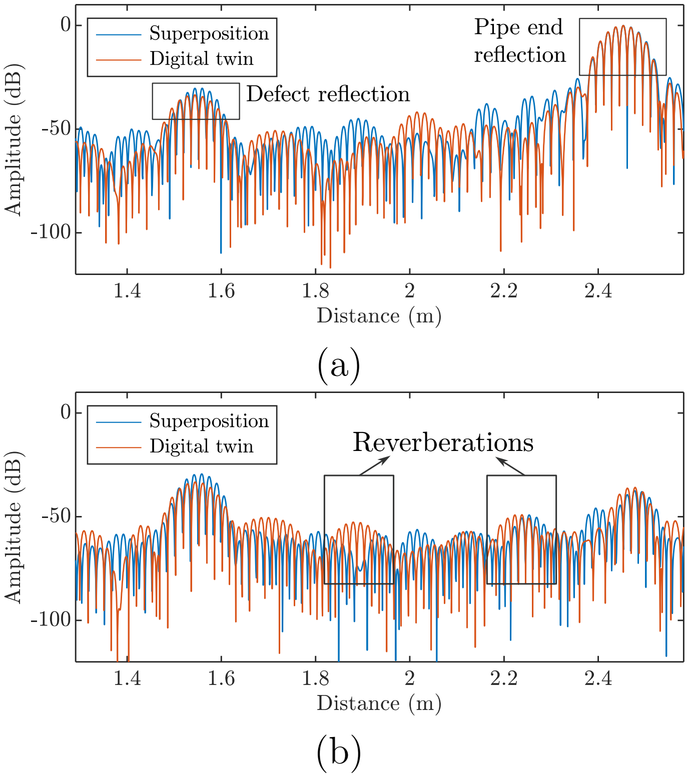

Figure 4.29: Comparison of superposition-generated signals and digital twin model-generated signals, focusing on raw T(0,1) signals and residual signals after baseline subtraction on a logarithmic scale. (a) Raw T(0,1) signals. (b) Residual signals.

defect reflection is defined as the defect response, while the segment between the defect and the pipe-end reflection is used to estimate the residual noise. The residual noise in the digital twin case is noticeably higher than in the superposition case, as the digital twin captures reverberations arising from wave interactions with the defect. These reverberations are not accounted for in the superposition approach, which locally adds defect signals to the pre-collected undamaged signals. In practice, such reverberations may contribute to false positives or mask weaker damage signals, making it essential to model them accurately.

To further explore this effect, the distributions of residual noise and defect response are analysed in the presence of co-existing defects of varying sizes.

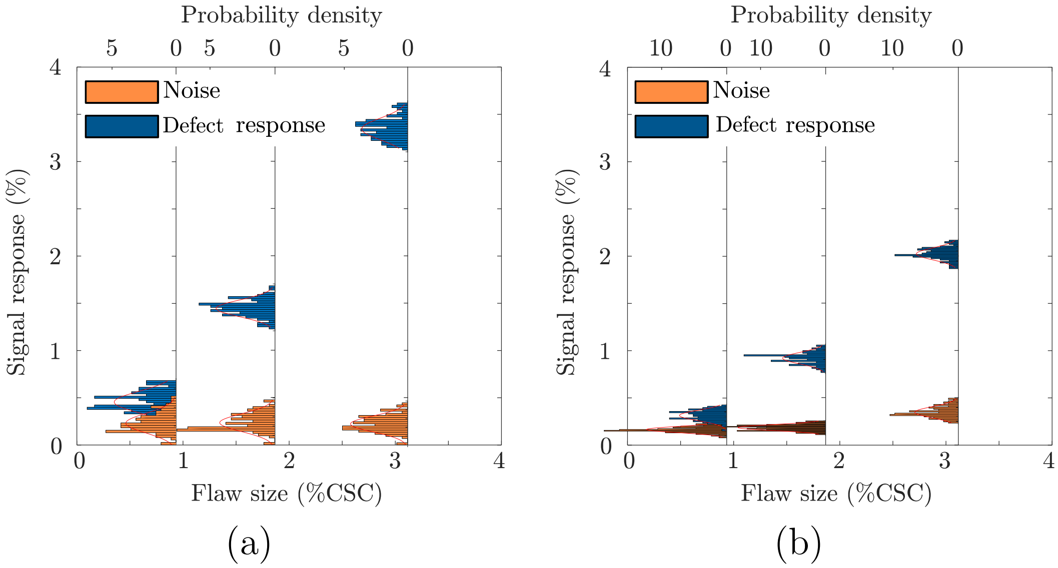

Figure 4.30: Comparison of the distribution of the residual noise and the signal response as the defect size varies. (a) Data generated by the superposition method. (b) Data generated by the digital twin model.

Figure 4.30 presents the statistical distributions for co-existing defect sizes of 0.94%, 1.88%, and 3.12% CSC. In the superposition case, the residual noise distribution remains relatively constant across all sizes, as wave interactions are not modelled. The defect response increases with flaw size, as expected. In contrast, the digital twin model shows an increase in both defect response and residual noise with larger co-existing defects, due to the reverberations captured by the full-physics model. The reliability of an SHM system depends on its ability to distinguish the defect signal from the background noise. When the co-existing defect reaches 3.12% CSC, the residual noise level becomes comparable to the signal response of the 0.94% CSC defect, significantly reducing its detectability.

To quantify this degradation in performance, Figure 4.31 presents Receiver Operating Characteristic (ROC) curves comparing the detectability of the 0.94% CSC defect in the presence of different co-existing defect sizes. The PFA is calculated from the residual noise distribution in each case, while the

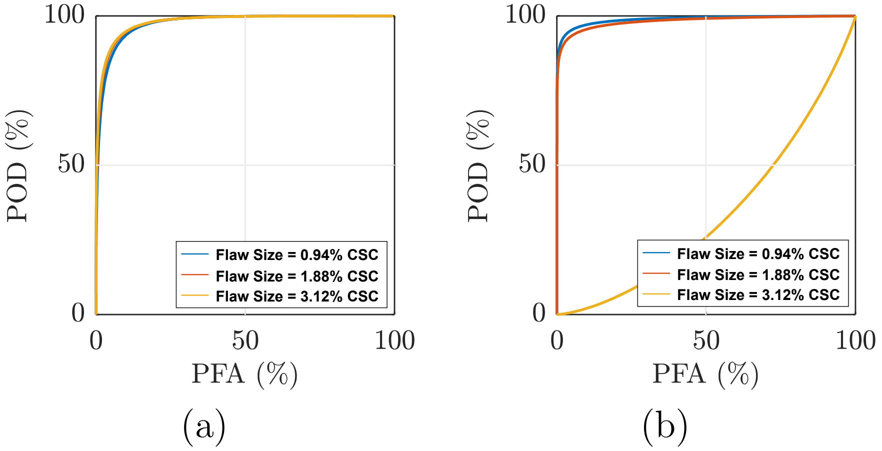

Figure 4.31: Comparison of the ROC curves for detecting a smaller defect with a flaw size of 0.94% in the presence of a pre-existing defect. (a) Data generated by the superposition method. (b) Data generated by the digital twin model.

POD is based on the 0.94% CSC defect response. In the superposition case (Figure 4.31a), the ROC curves remain consistent, as the residual noise level remains largely unchanged. However, in the digital twin case (Figure 4.31b), reverberations from larger co-existing defects increase the residual noise, shifting the ROC curve downward. When the co-existing defect is 3.12% CSC, the curve moves into a region where the PFA becomes unacceptably high, and reliable detection of the smaller defect is no longer feasible. This effect is only captured by the digital twin model, highlighting its advantage in simulating realistic wave interactions.

These findings have practical implications for SHM system deployment, where the condition of the structure is often unknown and multiple defects may exist simultaneously. In such scenarios, the ability to detect smaller defects can be compromised by the presence of reverberations from larger ones. The digital twin model provides a more accurate and conservative framework for estimating system performance in the presence of co-existing damage.

4.5 Digital twin-based long-term reliability estimation

The establishment of the digital twin model, updated based on in-situ experimental data collection, aims to provide timely reliability estimation of system performance throughout the entire life-cycle, considering the degradation of transducer performance and variations in environmental conditions. This section presents an illustration based on experimental data collected under laboratory conditions and compares it with the common practice of MAPOD used for SHM reliability estimation.

4.5.1 Long-term data collection

The long-term data of an SHM system was generated using experimental data with temperature variations collected in Section 4.3.1 in a laboratory environment, taking into account transducer performance degradation over time. Specifically, a degradation model for piezoelectric transducers was used to describe degradation over ten years [158], expressed as:

$$D(t) = \varrho t^{\eta} + \upsilon B(t^{\eta}) + K, \tag{4.7}$$

where $D(t)$ is the degradation level of a transducer, ϱ is the drift coefficient accounting for individual differences among transducers, υ is the diffusion coefficient that quantifies the random fluctuation or variability in the degradation process over time, $B(t^{\eta})$ is the standard Brownian motion, η is the time transformation factor, and K is a shift factor used to adjust the degradation level of all transducers. The coefficients of the degradation model are derived from accelerated degradation experiment estimations in [158] and adjusted using the coefficient K to fit the purpose of this study. The values are: $\varrho = 0.1773$, $\eta = 0.1717$, $\upsilon = 0.1706$, and $K = -0.4$.

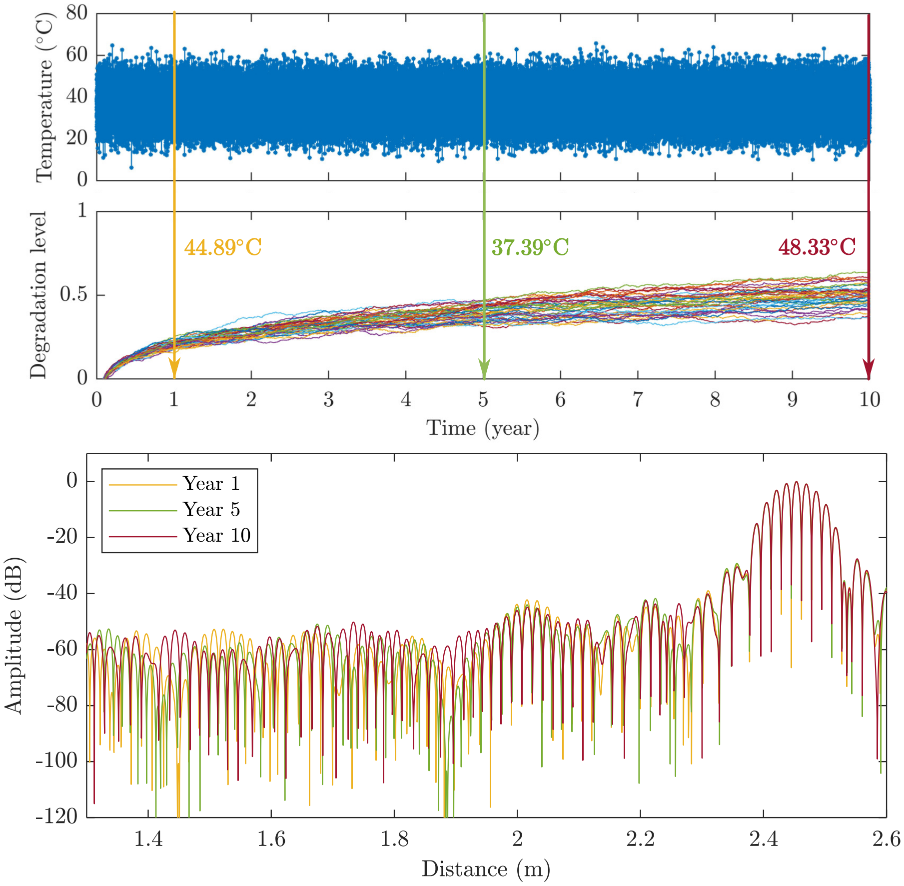

Figure 4.32: Temperature record and degradation data for forty transducers over ten years, along with the corresponding T(0,1) guided wave signals at three life points: 1 year, 5 years, and 10 years.

Figure 4.32 presents a comprehensive view of the data collected over a ten-year period. The upper part of the figure displays the temperature records alongside the degradation data for forty transducers. This study specifically analysed three critical life points: Year 1, Year 5, and Year 10. The recorded temperatures at these points were 44.89 °C, 37.39 °C, and 48.33 °C, respectively. The lower part of Figure 4.32 illustrates the guided wave signals corresponding to these three life points. These signals were generated by applying the degradation coefficient of each transducer to the full-matrix signal on both the excitation and reception sides, with an addition of random noise. The RMS level of this random noise was maintained consistent with levels observed in conditions without degradation, assuming constant random noise throughout the lifecycle of the SHM system. The SNRs for these three signals are 55.44 dB, 54.54 dB, and 52.60 dB, respectively. A quantitative increase in the noise level is evident, primarily due to increased coherent noise and decreased T(0,1) amplitude caused by transducer degradation over time, although the rise in noise amplitude is not consistent throughout the entire signal.

4.5.2 Digital twin-based MAPOD

Based on the digital twin framework, material properties, transducer performance, and random noise levels are estimated using in-situ data collected at three time points. Defects are then modelled in the digital twin to generate data with varying representative flaw sizes, ranging from 0.31% CSC to 3.13% CSC. The random noise level is kept consistent over the lifetime, with its distribution shown in Figure 4.33. This figure illustrates changes in signal levels at different stages through variations in SNRs, assuming the same RMS level of random noise. Similar to previous cases, 50 sets of data are generated for each scenario to ensure data independence. The defect location is randomly placed between 1.2 m and 1.9 m from the pipe end.

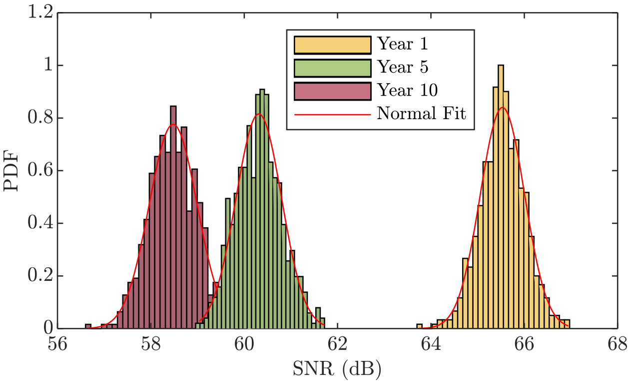

Figure 4.33: SNR distribution of the random noise level over the transducer's lifetime as modelled in the digital twin framework.

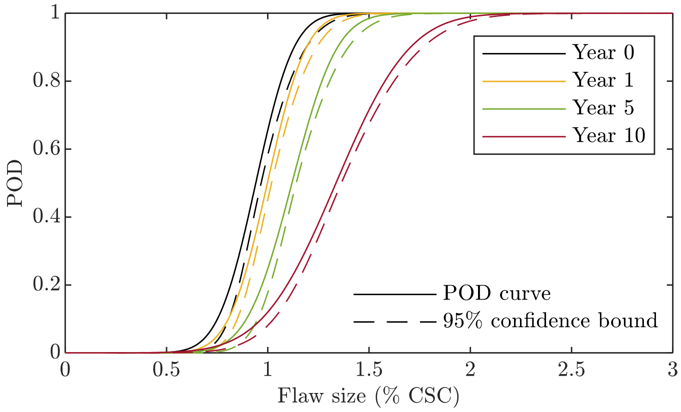

Figure 4.34: Comparison of POD curves at various stages against the baseline case at Year 0 with no degradation.

The POD curves at three life points, calculated based on the digital twin-based framework, are compared in Figure 4.34 against the baseline case at Year 0 with no degradation. Although the original time-trace signals at these three points in Figure 4.32 show visually similar noise levels, the POD curves reveal significant differences, with curves shifting rightward as the system's service years increase. The confidence level remains consistent across all cases due to the uniform sampling size for each scenario. Quantitatively, the $a_{90/95}$ values at these life points are 1.24% CSC, 1.40% CSC, and 1.77% CSC, indicating a degradation in the system's ability to detect the smallest defects with 95% confidence as service years increase.

4.5.3 Common practice MAPOD

Traditionally, the performance estimation of SHM systems involves assigning assumed distributions to the inputs of the simulation model to account for all possible situations throughout the system's life cycle. In this study, the procedure detailed in [159] is followed to estimate the performance of an SHM system over its entire life cycle and compare it with that derived from the digital twin-based framework. The data are computed using the following input variable distributions:

- **Defect position**: Randomly located between 1.2 m and 1.9 m from one of the pipe ends.
- **Defect size**: Varies from 0.31% CSC to 3.13% CSC.
- **Temperature variations**: Follows a normal distribution calculated from the temperature records shown in Figure 4.32, with the sampled temperatures shown in Figure 4.35a.
- **Remaining transducer performance $(1 - D(t))$**: Follows a log-normal distribution, with the sampled levels shown in Figure 4.35b.
- **Random noise level**: Follows a normal distribution wide enough to encompass the entire life-cycle random noise changes shown in Figure 4.33, with the sampled SNR distribution depicted in Figure 4.35c.

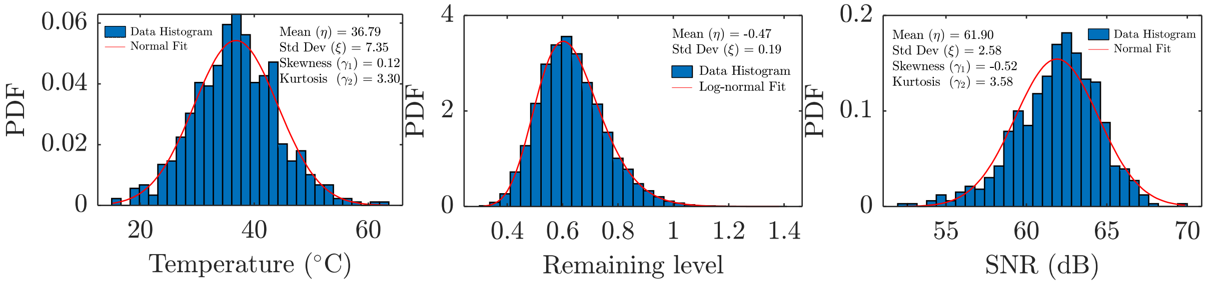

(a) (b) (c)

Figure 4.35: Distributions of the input variables in the simulation model: (a) Distribution of sampled temperatures, (b) distribution of sampled remaining transducer performance, and (c) distribution of random noise SNR levels.

Figure 4.36 shows the corresponding POD curve calculated using the conventional MAPOD method. Compared to the POD curves in Figure 4.34, which are derived using the proposed framework, the POD curve from the traditional MAPOD method closely resembles the Year 10 POD curve. This represents the worst-case scenario in the SHM system's life cycle. The wide variability in signal response, due to the consideration of a broad range of variables, leads to a conservative POD estimation. In addition, this approach provides no information about the evolution of the SHM system's performance throughout its entire life cycle.

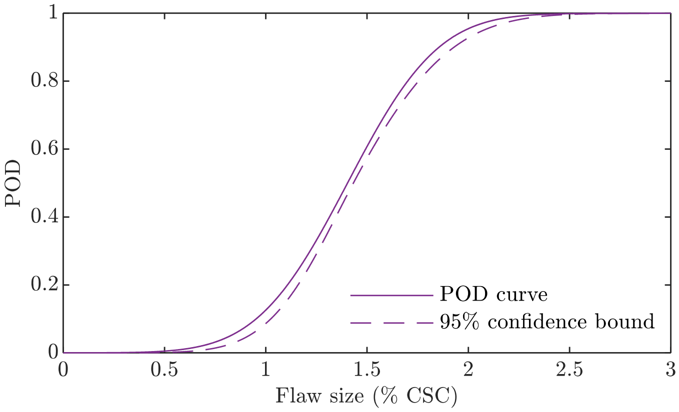

Figure 4.36: POD curve calculated using the traditional MAPOD method.

4.5.4 Discussion

The differences in the estimated POD curves based on the two methods are analysed by examining the signal responses for varying flaw sizes. Figure 4.37 illustrates the signal responses relative to flaw sizes generated by the digital twin model at Year 1, Year 5, and Year 10 of degradation, compared with those generated by the traditional MAPOD method based on input distributions. It can be observed that, as service years increase, the variance of the signal response for a given flaw size increases, leading to a larger τ in Eq. (3.18), and consequently, a less sharp POD curve. Additionally, the residual noise in the absence of defects exhibits a wider distribution, resulting in a higher threshold and a rightward shift of the POD curve. These factors collectively contribute to a larger $a_{90/95}$ value as service years progress.

In contrast, the traditional MAPOD case exhibits greater signal response scattering due to the consideration of a wide range of variables for the entire life cycle. This results in a larger threshold and greater standard deviation, τ, in the estimation of POD parameters. Consequently, the POD curve shifts rightward, leading to a conservative estimation of the $a_{90/95}$ value. The proposed digital twin-based framework, however, provides a reliability estimation specific to a given service time. This approach offers a more timely and accurate assessment of the system's performance, enabling more informed decisions for subsequent inspection and maintenance planning in practical applications.

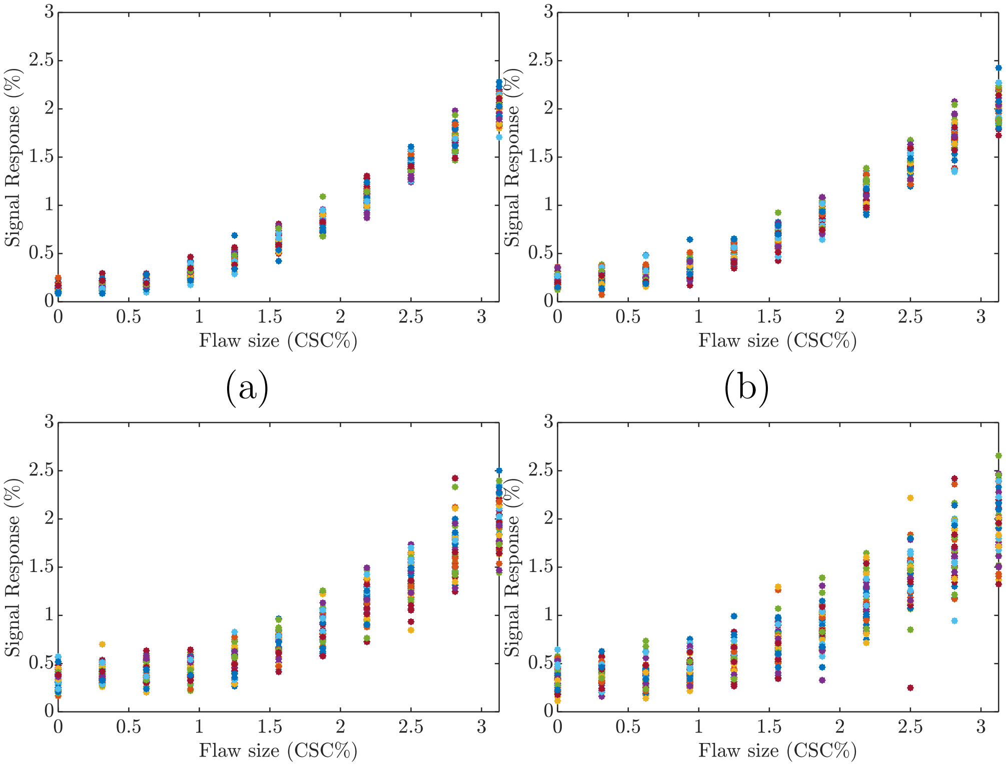

(a) (b)

(c) (d)

Figure 4.37: Signal responses for different flaw sizes generated by the digital twin model with Year 1, Year 5, and Year 10 degradation, compared with those generated by the traditional MAPOD method based on input distributions. (a) Year 1, (b) Year 5, (c) Year 10, and (d) data generated based on the traditional MAPOD method.

4.6 Summary

In this chapter, a digital twin-based reliability estimation framework is proposed and validated to provide specific reliability estimations tailored to measurement systems, environmental conditions, and examined structures. The primary goal is to offer a timely reliability estimation method throughout the entire lifecycle of an SHM system. The proposed framework establishes a digital twin model representing real-time measurement conditions based on a set of in-situ measurements. Key simulation parameters, including material properties, transducer performance, and random noise levels, are estimated from this model. The digital twin model makes it possible to model defect responses specific to current measurement conditions, allowing for timely and quantitative reliability estimations based on POD analysis.

The proposed digital twin model and related techniques for estimating material properties, transducer performance, and random noise are validated through laboratory measurements and tests using a commercial transducer ring setup. The fidelity of the digital twin model is demonstrated by comparing the digital twin-generated data with experimental data collected in a controlled environment with temperature variations. The results show that the established digital twin model can generate high-fidelity T(0,1) signals comparable to the experimental signals for both intact and defect cases, effectively capturing temperature effects and coherent noise levels. However, the performance of the digital twin model is less satisfactory when applied to a commercial transducer ring due to the absence of modelling complex effects, such as resonance and reflections from the installed transducer ring itself.

For validating the proposed framework in estimating SHM system performance, the POD analysis based on digital twin-generated data is compared with that generated by a well-verified data generation method based on superposition. The good agreement between the $a_{90/95}$ values derived from these two methods suggests that the proposed digital twin-based reliability estimation framework can provide reliable estimations that represent the actual performance of the system under real measurement conditions. Additionally, considering the influence of reverberations on threshold determination when multiple defects are present, the digital twin-based method can provide a more accurate estimation in guided wave pipe monitoring, considering the PFA.

Finally, the performance of the proposed digital twin-based framework is demonstrated through an application assessing the performance of an SHM system considering transducer degradation. Compared to the traditional MAPOD method, which relies on a wide range of variables to account for all possible measurement conditions throughout the lifecycle of an SHM system, the digital twin-based reliability estimation framework focuses on using parameters that are specific to the measurement conditions at the moment of interest, providing a more accurate and progressive quantitative assessment of system performance at any given moment throughout the entire lifecycle of an SHM system. This enables more informed decision-making for subsequent maintenance and inspection actions.

Chapter 5

Geometric imperfections in guided wave pipe monitoring

5.1 Introduction

Previous chapters discussed practical factors in guided wave monitoring, including random noise, coherent noise contributed by transducer performance imbalance, and temperature variations, with the aim of establishing a high-fidelity digital twin model for reliability assessment. These factors contribute to guided wave signals that do not originate from defects. Although the established digital twin model satisfactorily represents the noise level of real guided wave signals, duplicating coherent noise wavepackets remains challenging due to additional practical factors, such as geometric imperfections from imperfect manufacturing and operating conditions. Therefore, understanding the contribution of these factors to guided wave signals and identifying the significance of incorporating them into the digital twin model is crucial for accurate reliability estimation.

Seamless steel pipes are widely used in many oil and gas industrial applications due to their superior strength and high corrosion resistance. The manufacturing procedure for seamless pipes varies according to their diameters and diameter-to-wall thickness ratios [160]. Hot rolling methods remain the most widely used manufacturing techniques for making seamless pipes [161], with the cross-rolling method and the extrusion method being two typical examples [162]. Typically, a seamless pipe is formed from a cylindrical steel bar known as a billet, which is heated to a high temperature and then pierced to create a hollow tube using a piercing mandrel or punch. In the cross-rolling process, the hollow tube is transferred to a series of rollers where it is elongated and sized to the specified diameter and wall thickness [162]. In the extrusion process, the hollow tube is forced through a die by a hydraulic ram to shape the pipe to the prescribed outer diameter and wall thickness [163].

Although all manufacturing processes aim to achieve targeted dimensions [164], variations exist in pipe geometry due to uncertainties in the manufacturing process, where seamless pipes typically undergo extreme forces and heat treatment. These variations generally result from uneven heating, inconsistent pressure distribution, positioning variations, and tool wear [165]. For example, in the cross-rolling process, uneven heating of the steel billet, misalignment of the mandrel, and improper arrangement of the sizing mill can lead to deviations from the designed pipe dimensions [164,166]. Similarly, in the extrusion process, fluctuations in extrusion speed, temperature variations, and die wear can contribute to thickness variations in the pipe wall. Additionally, the cooling rate after the forming process can introduce residual stresses and further affect the dimensional accuracy of the seamless pipe [167]. Generally, the extrusion process is more suitable for smaller to medium-sized pipes. Extruded seamless pipes exhibit higher dimensional accuracy compared to those produced by the cross-rolling process, owing to the more controlled deformation and the use of precision dies in extrusion. Consequently, the extrusion method is widely used in demanding applications such as nuclear power and aerospace industries, where precision and consistency are paramount.

One typical geometric imperfection of seamless pipes is variation in wall thickness, the pattern of which varies according to different causative factors [100]. For example, in the cross-rolling process, misalignment of the piercing mandrel with the billet centre can result in an eccentric pipe, while the rotary motion of rollers in the sizing mill can introduce a twisting pattern in the pipe wall thickness along the length of the pipe [168, 169]. An example wall thickness variation map of a seamless pipe is presented in [170], showing a combination of axial and spiralling thickness variations. [171] presents a series of wall thickness measurements along the length of a seamless carbon steel pipe over 16 m using a conventional ultrasonic thickness gauge, demonstrating that the maximum deviation of the wall thickness is about 5.5% for the inspected pipe with a mean thickness of 3.14 mm. In contrast to welded pipes, which typically have more uniform wall thickness distributions due to being manufactured from plates, seamless pipes exhibit these more complicated wall thickness variation patterns; therefore, this study focuses on seamless pipes.

Several methods exist to quantitatively characterise variations in pipe wall thickness. One common approach utilises statistical measures and distribution analyses calculated from a large set of point-by-point thickness measurements, such as mean, coefficient of variation, and best-fit distributions [36]. While this method effectively describes the extent of variability in wall thickness, it does not account for spatial relationships among these variations.

Another approach describes pipe wall thickness variations based on harmonic analysis of the circumferential wall thickness of a cross-section, assuming uniform wall thickness along the pipe length. Specifically, the wall thickness along the pipe circumference is approximated by Fourier analysis, assuming higher-order variations are negligible [165, 168], and the wall thickness variation can be described by a series of complex Fourier coefficients. Although this method describes both the variability and spatial correlation of pipe wall thickness, it has limitations. Even ignoring higher orders of periodicity in Fourier analysis, a high number of Fourier coefficients are needed to describe the spatial correlation of wall thickness variations with high resolution, making it inconvenient to obtain a generic rule for describing the influence of wall thickness variations on guided wave behaviours. Additionally, the assumption of uniform wall thickness along the pipe length might not always hold true, especially for pipes manufactured by the cross-rolling method.

Alternatively, pipe wall thickness variation can be treated as a random process as a function of space, similar to the characterisation of rough surfaces [172, 173]. Wall thickness variations usually have similar statistical characteristics to pipe roughness but at a larger scale. Assuming the deviation of pipe wall thickness from the nominal wall thickness is a random process, it can be described by a thickness variation function $h(z, \theta)$, commonly assumed to follow a Gaussian distribution with a mean value of zero, supported by field measurements of pipe wall thickness variations in literature [36]. Therefore, the PDF of the thickness variation function can be expressed as:

$$pdf(h) = \frac{1}{\sigma\sqrt{2\pi}} \exp\left(-\frac{h^2}{2\sigma^2}\right), \tag{5.1}$$

where σ is the standard deviation, which describes the extent of wall thickness variability. This standard deviation can be estimated by:

$$\sigma = \sqrt{< h >^2}, \tag{5.2}$$

where $<>$ denotes the ensemble averaging of wall thickness variations over the whole pipe.

The spatial relation of wall thickness variations is described by the correlation function of $h(z, \theta)$:

$$C(\mathbf{R}) = \frac{h(\mathbf{r})h(\mathbf{r}+\mathbf{R})}{\sigma^2}, \tag{5.3}$$

when the pipe is unwrapped into a plate, mapping the circumferential (θ) and axial (z) coordinates to Cartesian x and y coordinates, respectively. Here, $\mathbf{r}$ is the position of one measurement point, and $\mathbf{R}$ is the position vector, that is, the separation distance between two measurement points. The correlation function describes how two measurement points with a separation of $\mathbf{R}$ correlate. Commonly, the correlation function is assumed to follow a Gaussian function [173]:

$$C(\mathbf{R}) = \exp\left(-\left(\frac{x^2}{\lambda_x^2} + \frac{y^2}{\lambda_y^2}\right)\right), \tag{5.4}$$

where λ_x and λ_y are the correlation lengths in the pipe axial and circumferential directions, respectively, defined as the distance over which the correlation function $C(\mathbf{R})$ drops to 1/e from its initial value. Thus, this method describes pipe wall thickness variations using three parameters: standard deviation σ, axial correlation length λ_x, and circumferential correlation length λ_y.

In the pipe production industry, the tolerance of pipe geometry has been specified in several standards and codes, such as ASTM A106/A106M-19a [174] and API Specification 5L [175]. According to API Specification 5L, the tolerance for wall thickness variation of a seamless pipe with an outside diameter between 168.3 mm to 610 mm and a length between 4 mm and 25 mm ranges from -12.5% to 15% of the nominal pipe wall thickness. However, these specifications do not address the spatial variations of pipe wall thickness, despite their potentially significant influence on guided wave behaviours in pipes [176].

This chapter investigates the potential contribution of initial geometric imperfections in pipes, specifically wall thickness variations, to guided wave signals. The investigation begins with an examination of variation patterns in pipe wall thickness based on measurements from two seamless pipes used in previous chapters. Subsequently, FE models are developed for pipes with wall thickness variations within tolerance specifications, and the influence of these variations on guided wave signals is analysed in terms of coherent noise levels. Furthermore, the chapter discusses the mechanism by which wall thickness variations affect coherent noise levels, based on the analysis of different wave modes.

5.2 Experimental measurements

To investigate the characteristics of wall thickness variations in real pipes, the thickness of Pipe 1 and Pipe 2 listed in Table 2.1 was examined using an Electromagnetic Acoustic Transducer (EMAT) transducer exciting ultrasonic bulk shear waves. The pipe wall thickness was determined by measuring the ToF of wave reflections in pulse-echo mode [177]. Both pipes were manufactured under the API 5L specification, which permits a thickness variation of $-12.5\%/+15\%$ from the nominal pipe wall thickness (10.31 mm for Pipe 1 and 13.30 mm for Pipe 2).

For Pipe 1, measurements were taken at three cross-sections: one in the middle and two at the pipe ends. At each section, 20 equally spaced circumferential points were measured, totalling 60 points. The three selected cross-sections are located at critical points where variability is expected to be highest, according to industry insights [175]. This placement ensures both a comprehensive representation of the pipe's condition and adequate data granularity. Figure 5.1a presents the measurement points relative to a reference cross-section with nominal thickness. Deviations from the nominal pipe wall thickness are evident around the pipe circumference, with an average absolute difference of 0.43 mm and a maximum deviation of 1.15 mm, falling within specified tolerances. The thickness profiles at different axial locations show good consistency, indicating that circumferential thickness variation is much larger than axial variation. This is evident from the different average standard deviations: 0.35 mm circumferentially and 0.12 mm axially. These findings align with observations from several measurements of different seamless pipes in the literature [168, 178]. Such variations could originate from the sizing stage, where the angular arrangement of roller sets introduces star-shaped imperfections corresponding to roller locations. Based on circumferential thickness variations measured at three axial locations, the average circumferential correlation length is 0.0371 m.

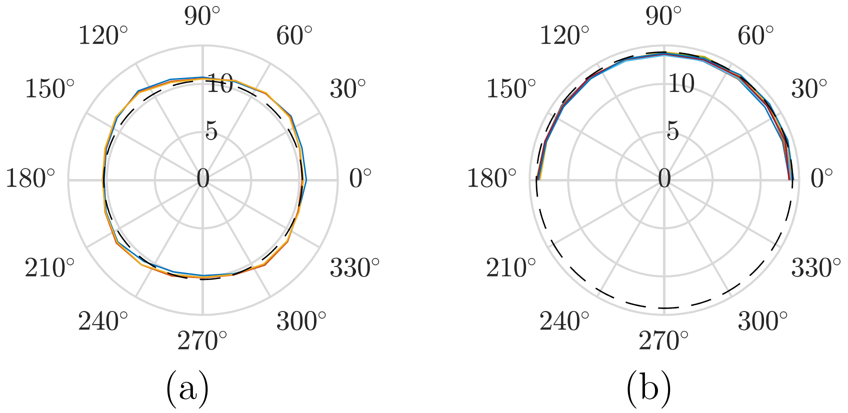

(a) (b)

Figure 5.1: Cross-sectional wall thickness measurements of Pipe 1 and Pipe 2 listed in Table 2.1. Measurements were taken at various axial and circumferential locations, with the nominal wall thickness shown as a dashed line for reference. (a) Measurements for Pipe 1 with a nominal wall thickness of 10.31 mm. (b) Measurements for Pipe 2 with a nominal wall thickness of 13.30 mm.

For Pipe 2, measurements were taken around half of the circumference at 8 axial locations with 200 mm intervals, totalling 88 points. Figure 5.1b compares the thickness profiles of cross-sections at different axial locations with the reference nominal thickness. Pipe 2 exhibits smaller wall thickness variations compared to Pipe 1, with an average absolute thickness difference of 0.18 mm and a maximum deviation of -0.44 mm. The average standard deviations of wall thickness variation are 0.12 mm circumferentially and 0.13 mm axially, indicating similar levels of non-uniformity in both directions. The differing characteristics of wall thickness variations between Pipe 1 and Pipe 2 may result from different manufacturing processes, details of which were not provided by the pipe manufacturer. Based on the thickness variation in the axial direction measured at 11 circumferential locations of Pipe 2, the average axial correlation length is 0.13 m, which corresponds to approximately 1/4 of the wavelength of the T(0,1) wave mode at a central frequency of 50 kHz.

5.3 FE modelling

To investigate the contribution of initial wall thickness variations on guided wave signals, specifically the coherent noise levels, FE models of pipes with various scales of wall thickness variations within the specified tolerance were developed. These models extend beyond the measurements performed on the limited pipes in the laboratory.

The FE simulation model was based on Pipe 1 listed in Table 2.1, with the configuration detailed in Section 3.3.1. For efficient simulation with satisfactory accuracy for statistical analysis, an element size of 2 mm was used, corresponding to approximately 30 elements per wavelength for the T(0,1) mode, adhering to principles for high-accuracy explicit dynamic simulation [99]. Pipe wall thickness variations were modelled by adjusting mesh node positions of the original pipe model with nominal wall thickness, specifically by compressing or extending the mesh in the pipe radial direction according to the wall thickness variations, minimising mesh distortion. In doing this the inner radius was maintained at the same position.

For practical consideration of coherent noise, the imbalance of transducer performance was incorporated into the simulation models. This was achieved by applying the transducer transfer functions on both the excitation and reception sides in the simulation. These transfer functions were estimated from the experimental data collected in Section 4.3.1 at room temperature. Figure 5.2a shows the amplitude of the transducer transfer functions at the central frequency of 50 kHz, representing the imbalance of the transducer performance. Figure 5.2b displays the Fourier analysis of these amplitude variations, indicating the potential excitation of different wave modes with various circumferential orders. The analysis reveals that with this transducer performance imbalance, the main wave mode excited is the fundamental order zero mode, with the flexural wave modes of the first order (F(1,m)) having the second largest amplitude.

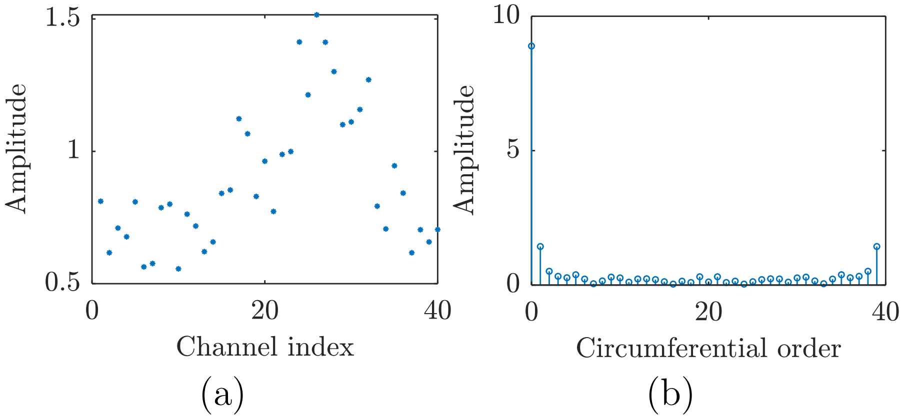

(a) (b)

Figure 5.2: Incorporation of transducer performance imbalance in the simulation. (a) Amplitudes of transducer transfer functions at the central frequency of 50 kHz. (b) Fourier analysis of the amplitude variations. Amplitudes are shown in a comparable arbitrary scale.

The pipe wall thickness variations were generated using a correlated two-dimensional (2D) random thickness variation map h. This map was created by performing a moving average window on an uncorrelated 2D random thickness variation map v, which follows a Gaussian distribution [172]. For given statistical parameters of the wall thickness variation (standard deviation σ and spatial correlation lengths λ_x and λ_y), the corresponding uncorrelated 2D random thickness variation map and the moving window can be determined.

The standard deviation of the uncorrelated 2D random thickness variation map is determined by:

$$\sigma_v^2 = \sigma^2 / \sum_{i=-I}^{I} \sum_{j=-J}^{J} w_{ij}^2, \tag{5.5}$$

where σ_v is the standard deviation of the uncorrelated 2D random thickness variation map v, and I and J are the extents of the kernel in axial (x) and circumferential (y) directions, respectively. w_{ij} is the moving window. For a pipe wall thickness variation with a Gaussian correlation function, the moving window can be expressed as:

$$w_{ij} = \exp\left[-2\frac{(i\Delta x)^2}{\lambda_x^2} - 2\frac{(j\Delta y)^2}{\lambda_y^2}\right], \tag{5.6}$$

where Δx and Δy are the uniform mesh sizes in axial and circumferential directions, respectively. Therefore, the correlated 2D random thickness variation map h is the convolution between the uncorrelated 2D random thickness variation map and the moving window, expressed as:

$$h_{pq} = \sum_{i=-I}^{I} \sum_{j=-J}^{J} w_{ij} v_{p+i,q+j}. \tag{5.7}$$

It should be noted that the actual statistical measures of the generated wall thickness variation map may deviate from the nominal statistical parameters due to the finite geometrical size of the pipe. This discrepancy arises because the correlation length represents the distance over which the properties of thickness variation repeat themselves. A statistical description of a thickness variation map becomes meaningful only if the size of the pipe spans significantly beyond several multiples of the correlation length [172]. As the experimental measurements of the wall thickness variations in Section 5.2 suggest, the correlation length in the circumferential and axial directions can vary over a large range. For example, in cases where the pipe wall thickness has uniform variations along the pipe axis, the correlation length in the pipe axial direction is infinite, and the statistical measures of the generated wall thickness variation map deviate significantly from the nominal designated statistical parameters. Therefore, the actual statistical measures of the generated wall thickness variation map should be calculated and used in the analysis.

In this study, wall thickness variations within the pipe industry specification are of interest. The variations are within the range of $[-12.5\%, +15\%]$ of the nominal pipe wall thickness, and the standard deviation of all generated wall thickness variation maps follows a normal distribution with a mean value of 4% and a standard deviation of 1%. The wave scattering from a surface with stochastic fluctuations can be classified into three distinct categories based on the relationship between standard deviation, correlation length, and wavelength: Rayleigh (long wavelength), stochastic (medium wavelength), and geometric (short wavelength) [179]. Given the standard deviation modelled in this study, which is significantly smaller than the T(0,1) wavelength, the behaviour of wave scattering from the pipe wall thickness variations falls primarily within the Rayleigh and stochastic categories. Furthermore, considering the initial wall thickness variation patterns that may exist in a seamless pipe induced in the manufacturing process, the spatial correlation of the wall thickness variations investigated in this study is categorised into three different regimes:

- Regime 1: Wall thickness variations have similar small levels in both pipe axial and circumferential directions.
- Regime 2: Wall thickness variations have a small correlation length in the circumferential direction but an increasing correlation length in the axial direction.
- Regime 3: Wall thickness variations have a large correlation length in both pipe axial and circumferential directions.

Due to the random nature of the wall thickness variations, Monte Carlo simulations were performed with multiple simulation realisations for each case with similar nominal statistical parameters. In total, 500 realisations of FE simulations of pipes with wall thickness variations across all three regimes were conducted for statistical analysis. This number was chosen based on a balance between computational feasibility and the need for adequate data granularity to capture the inherent variability in the simulations [173].

Figure 5.3 illustrates typical generated wall thickness variation maps of an unwrapped pipe with spatial correlations in these three regimes. The correlation lengths are normalised by the wavelength of the T(0,1) mode at 50 kHz. Figures 5(a)-5(c) depict wall thickness variations with spatial correlations in Regime 1, characterised by relatively shorter correlation lengths in both circumferential and axial directions. Figures 5(d)-5(f) show wall thickness variations with spatial correlations in Regime 2, where circumferential correlation lengths remain short, but axial correlation lengths increase from small to large, approaching uniform variation along the pipe axis. Wall thickness

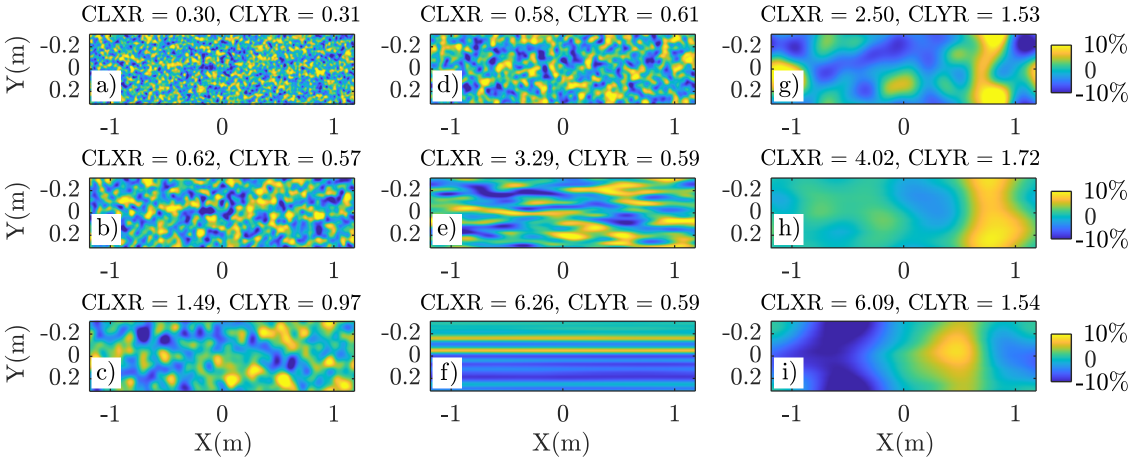

Figure 5.3: Typical generated wall thickness variation maps of an unwrapped pipe with spatial correlations in three regimes. The colour represents wall thickness variation values. Correlation lengths are normalised by the wavelength of the T(0,1) mode at 50 kHz. CLXR and CLYR denote the normalised correlation lengths in pipe axial and circumferential directions, respectively. (a-c) Wall thickness variations with spatial correlations in Regime 1: short correlation lengths in both directions. (d-f) Regime 2: short circumferential correlation lengths with increasing axial correlation lengths. (g-i) Regime 3: larger circumferential correlation lengths with increasing axial correlation lengths.

variations with spatial correlations in Regime 3 are illustrated in Figures 5(g)-5(h), featuring increasing correlation lengths in the pipe axial direction and larger correlation lengths in the circumferential direction.

5.4 Results and discussion

Figure 5.4 presents the coherent noise level of all 500 realisations with different statistical measures. The coherent noise level is characterised by the SNR between the T(0,1) wave mode reflected from the pipe end and the coherent noise. The coherent noise is defined as the signal before the T(0,1) pipe end reflection, between 0.8 ms and 1.4 ms. The T(0,1) signal is similar to that shown in Figure 4.9 and is not shown here. In Figure 5.4, the colour of the dots represents the SNRs of the guided wave signals, compared to the reference case without wall thickness variations (54.17 dB). Lower SNR values correspond to higher coherent noise levels. Generally, wall thickness variations with smaller correlation lengths lead to higher coherent noise levels. The contribution of wall thickness variations to the coherent noise level is distributed due to the random nature of the wall thickness variation map.

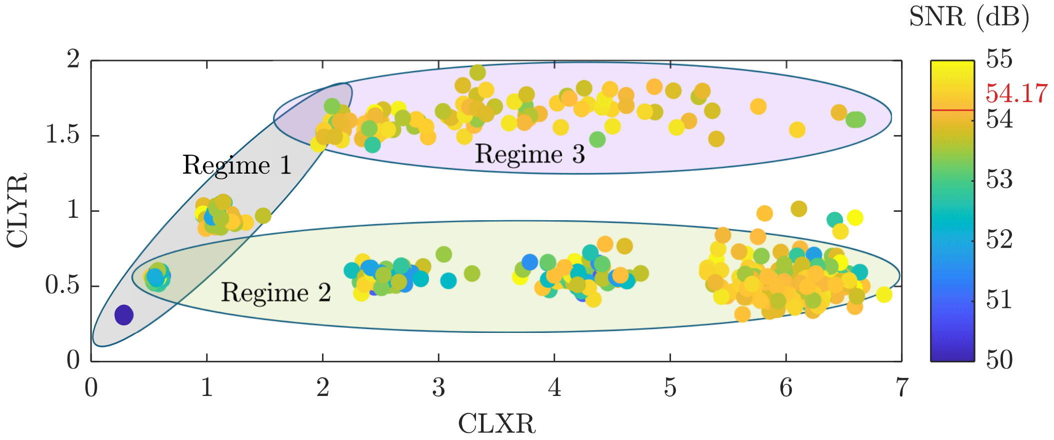

Figure 5.4: Coherent noise levels for 500 realisations with various statistical measures across three regimes. The colour of each dot represents the SNR of the guided wave signals, compared to the reference case without wall thickness variations (54.17 dB). Lower SNR values (cooler colours) indicate higher coherent noise levels.

The influence of wall thickness variations on coherent noise levels exhibits different behaviours across the regimes. In Regime 1, coherent noise level generally decreases with increasing correlation lengths. Regime 2 presents a more complex relationship between correlation length and coherent noise level, where the coherent noise level does not change monotonically with the axial correlation length when the circumferential correlation length remains similar. In Regime 3, wall thickness variations have a less significant influence on coherent noise levels compared to the other two regimes.

The coherent noise in guided wave signals is contributed by waves resulting from non-symmetric excitation conditions (due to transducer performance imbalance) and non-symmetric pipe structure (due to wall thickness variations). As discussed in Chapter 2, unwanted circumferential and flexural wave modes exist when there is an imbalance in the wave excitation of the T(0,1) wave mode. When thickness variations are present in the pipe wall, several phenomena contribute to the coherent noise. The T(0,1) wave mode can be scattered from the uneven pipe wall and captured as coherent noise in the guided wave signals. Additionally, the number of excited flexural wave modes and uncancelled circumferential wave modes may change due to non-symmetric pipe sections. These flexural and circumferential wave modes can also be scattered from the uneven pipe wall. Furthermore, mode conversions occur when different wave modes are scattered by the uneven pipe wall. All these effects collectively contribute to the coherent noise observed in guided wave signals. To investigate the influence of pipe wall thickness variations on coherent noise levels and how they affect guided wave behaviours, the guided wave signals from all realisations with different statistical measures are analysed in the three regimes in the following sections.

5.4.1 Regime 1

In Regime 1, the correlation lengths are similar in the axial and circumferential directions. Figure 5.5a illustrates the change in coherent noise levels with increasing correlation length in the pipe axial direction. When the correlation length of wall thickness variations is small (approximately 1/4 wavelength), the coherent noise level increases significantly. As the correlation length increases to about 0.6 wavelengths or larger, the wall thickness variations contribute less to the coherent noise levels, within a 5 dB range. The random nature of the generated wall thickness variations results in a distribution of coherent noise levels. For each correlation length measure, this

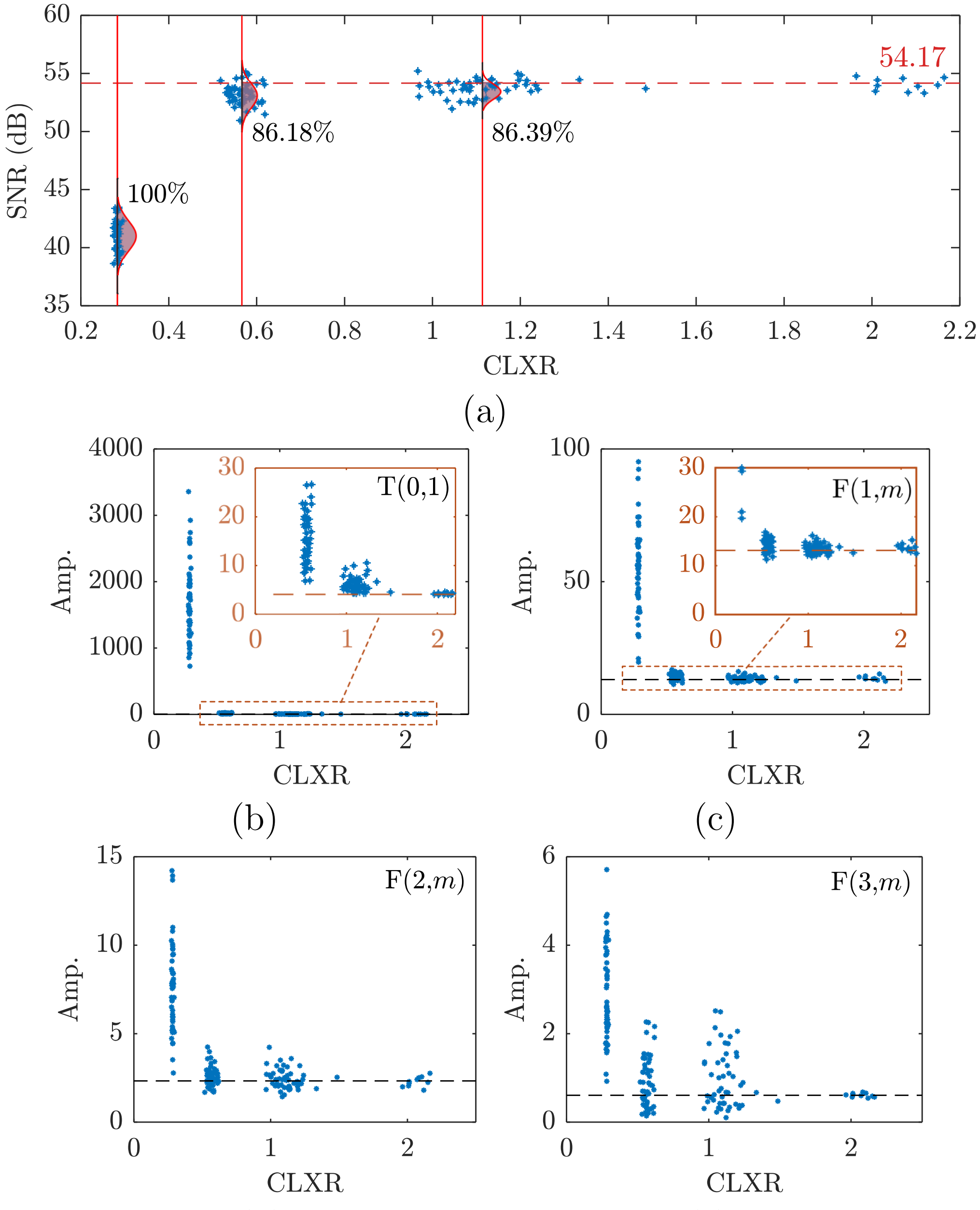

(a)

(b)

(c)

(d)

(e)

Figure 5.5: Analysis of pipe wall thickness variations in Regime 1 and their impact on coherent noise levels. (a) Coherent noise levels as a function of normalised axial correlation length, with the reference case (uniform nominal wall thickness) shown as a dashed line. (b-e) Amplitudes of various wave modes at the central frequency of 50 kHz: (b) T(0,1), (c) F(1,m), (d) F(2,m), and (e) F(3,m). The dashed lines in (b-e) represent the corresponding amplitudes for the reference case.

distribution can be fitted by a normal distribution to quantify the probability that wall thickness variations with specific statistical measures increase the coherent noise levels of guided wave signals. The coherent noise level of the reference case with uniform nominal wall thickness serves as a threshold. The probability that wall thickness variations increase the coherent noise level is quantified by the area of the fitted probability density function below this threshold. Despite the relatively small amplitude increase in coherent noise levels compared to cases with small correlation lengths, the probability of wall thickness variations increasing coherent noise levels remains high (over 86%) when the axial correlation length reaches one wavelength.

To investigate the mechanism by which wall thickness variations contribute to coherent noise levels, different wave modes are extracted and their amplitudes at the central frequency of 50 kHz are compared in Figures 5.5b to 5.5e. The amplitude levels of different wave modes for the reference case without wall thickness variations are shown as dashed lines for comparison. For the T(0,1) wave mode (Figure 5.5b), components above the dashed line are attributed to T(0,1) wave mode scattering from uneven pipe wall thickness. This scattering decreases significantly when the axial correlation length increases to around one wavelength, approaching levels similar to other flexural wave modes. This indicates that wave scattering from the uneven pipe wall due to wall thickness variations becomes relatively weak when the axial correlation length reaches one wavelength.

In Regime 1, among the extracted flexural wave modes, the F(1,m) family exhibits the highest amplitude, followed by F(2,m), while F(3,m) wave modes have the lowest amplitude. This relative amplitude relationship among different wave modes aligns with the reference case of uniform nominal wall thickness, suggesting that wall thickness variations within this regime do not substantially alter the excitation of different wave modes. Thus, the coherent noise is primarily contributed by wave scattering from the uneven pipe wall, rather than additional excitation of flexural wave modes due to the non-symmetric pipe structure caused by wall thickness variations.

With wall thickness variations having an axial correlation length of approximately 1/4 wavelength, the T(0,1) wave mode shows significantly higher amplitude compared to other flexural wave modes. This suggests that coherent noise is predominantly contributed by T(0,1) wave mode scattering from the uneven pipe wall in this case. As the axial correlation length of wall thickness variation increases to half a wavelength, the amplitude of the T(0,1) wave mode becomes comparable to that of the F(1,m) wave modes. This implies that for guided wave signals collected from pipes with wall thickness variations at this scale, coherent noise is mainly contributed by both T(0,1) and F(1,m) wave modes. When the correlation length exceeds one wavelength, wave scattering from uneven pipe walls becomes relatively weak, and coherent noise in this case is dominated by F(1,m) wave modes.

5.4.2 Regime 2

As illustrated in Figure 5.4, Regime 2 exhibits a more complex relationship between wall thickness variations and coherent noise levels in guided wave signals. The coherent noise level does not change monotonically with increasing axial correlation length. In this regime, where the axial correlation length approaches or exceeds the pipe length, the correlation length calculated from the autocorrelation function of wall thickness variations becomes less accurate. To address this, an alternative metric is introduced: the averaged standard deviation of wall thickness variations along the pipe's axial direction. This metric is calculated by determining the standard deviation of wall thickness variations along the axial direction at each circumferential location and then averaging these values circumferentially.

Figure 5.6a demonstrates the impact of this averaged standard deviation (normalised by the T(0,1) wavelength at 50 kHz) on the coherent noise level of guided wave signals. Similar to Regime 1, the contribution of pipe wall thickness variations to coherent noise levels is quantified using a probability measure. This probability is represented by the area of the fitted normal distribution below the threshold set by the coherent noise in the reference case with uniform nominal wall thickness. The coherent noise level exhibits a wide variation around the reference level, ranging from 50 dB to 56 dB. Notably, scattered points above the reference SNR level correspond to cases where the

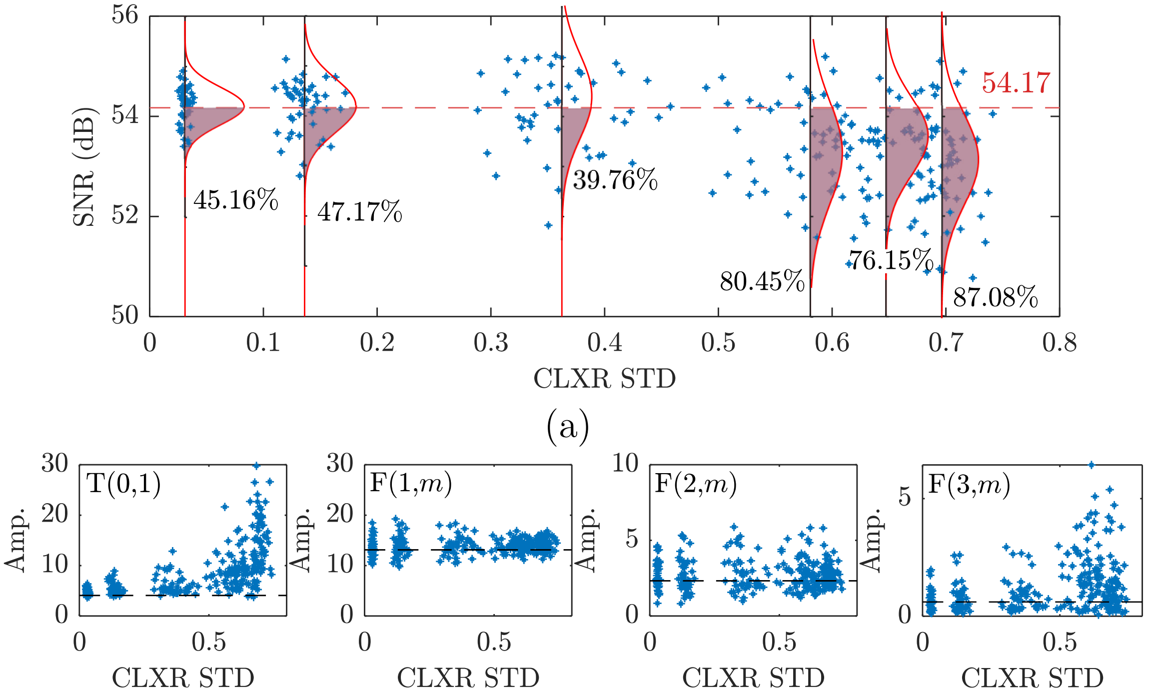

(a)

(b) (c) (d) (e)

Figure 5.6: Analysis of pipe wall thickness variations in Regime 2 and their impact on coherent noise levels. (a) Coherent noise levels versus normalised averaged standard deviation of axial wall thickness variations, with the reference case (uniform nominal wall thickness) shown as a dashed line. (b-e) Amplitudes of various wave modes at the central frequency of 50 kHz: (b) T(0,1), (c) F(1,m), (d) F(2,m), and (e) F(3,m). The dashed lines in (b-e) represent the corresponding amplitudes for the reference case.

coherent noise level is reduced, which can only occur when the excitation of flexural wave modes changes due to alterations in non-symmetric pipe sections. Furthermore, the probability of wall thickness variations increasing coherent noise levels rises with the averaged standard deviation in the pipe axial direction, confirming that this metric effectively measures wall thickness variations when their scales become comparable to the pipe's geometric size.

To investigate the contribution of different guided wave modes to coherent noise in Regime 2, various wave modes are extracted and analysed, similarly to the approach in Regime 1. Figures 5.6b to 5.6e present the amplitudes of different wave modes at the central frequency of 50 kHz, with the reference case (uniform nominal wall thickness) shown as a dashed line for comparison. The amplitude of the T(0,1) wave mode increases noticeably with the averaged standard deviation of wall thickness variations in the pipe axial direction. The F(3,m) family modes exhibit a similar trend, indicating stronger wave scattering from the uneven pipe wall as the averaged standard deviation increases. However, the amplitude of T(0,1) wave modes remains comparable to that of F(1,m) family wave modes, suggesting that wave scattering from the uneven pipe wall is considerably weaker than in Regime 1.

Interestingly, the amplitude of F(2,m) family wave modes remains relatively constant with increasing averaged standard deviation in the axial direction, while F(1,m) family wave modes show a slight decrease. This phenomenon suggests a change in the excitation of different wave modes as the pipe cross-section changes due to wall thickness variations. Consequently, it is possible for wave mode amplitudes to remain similar or even decrease when pipe wall thickness exhibits sharper spatial variations.

As previously discussed, wall thickness variations impact guided wave signals in two ways: by altering the excitation of different wave modes due to non-symmetric wave excitation conditions, and through wave scattering from the uneven pipe wall. In Regime 1, the latter effect dominates, resulting in increased amplitudes of different wave modes as wall thickness variations increase. Conversely, in Regime 2, wall thickness variations have a more significant influence on the excitation of different wave modes than on wave scattering. This explains why some wave modes, such as the F(1,m) family, exhibit smaller amplitudes as pipe wall thickness variations increase.

5.4.3 Regime 3

In Regime 3, pipe wall thickness variations exhibit larger correlation lengths in both circumferential and axial directions. Within this regime, the influence of wall thickness variations on coherent noise levels is generally smaller than in Regimes 1 and 2. Due to the large correlation lengths in both directions compared to the pipe's geometric size, wall thickness variations are characterised by the averaged standard deviation.

Figure 5.7a illustrates the relationship between coherent noise levels and the averaged standard deviation of wall thickness variations in the axial direction. The coherent noise levels are distributed around the reference level of 54.17 dB (corresponding to uniform nominal wall thickness) and range from 53 dB to 55 dB, a significantly smaller range compared to Regimes 1 and 2.

A wider distribution of coherent noise levels is observed when the normalised averaged standard deviation is around 0.6, suggesting that factors beyond the axial averaged standard deviation influence the coherent noise levels. Figure 5.7b presents colour-coded coherent noise levels as a function of averaged standard deviations in both axial and circumferential directions. The averaged standard deviation in the circumferential direction shows a larger value range when the normalised axial averaged standard deviation is around 0.6, consistent with the wider distribution of coherent noise levels at this

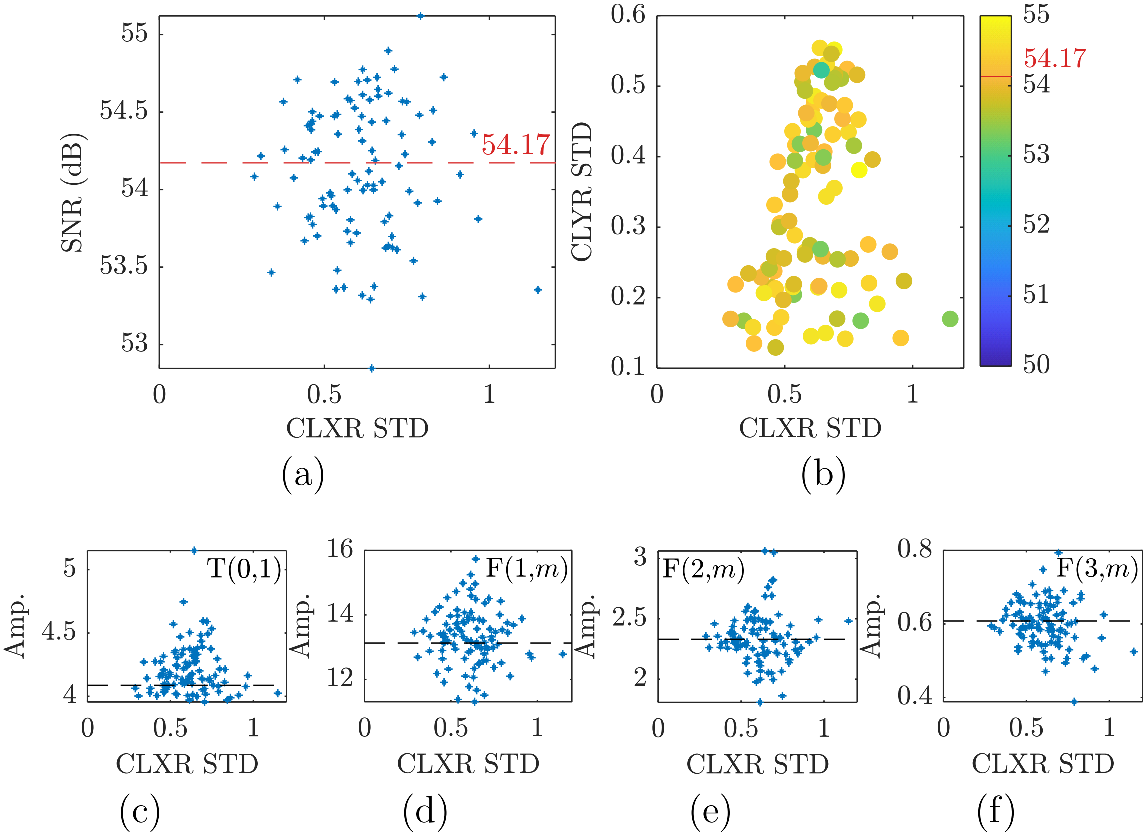

(a) (b)

(c) (d) (e) (f)

Figure 5.7: Analysis of pipe wall thickness variations in Regime 3 and their impact on coherent noise levels. (a) Coherent noise levels versus normalised averaged standard deviation of axial wall thickness variations. (b) Colour-coded coherent noise levels as a function of averaged standard deviations in axial and circumferential directions. (c-f) Amplitudes of various wave modes at the central frequency of 50 kHz: (c) T(0,1), (d) F(1,m), (e) F(2,m), and (f) F(3,m). Dashed lines indicate reference values for uniform nominal wall thickness.

point. Figures 5.7c to 5.7f depict the amplitudes of different wave modes in guided wave signals as a function of increasing averaged standard deviation of axial wall thickness variations. All guided wave modes exhibit a wider amplitude distribution when the normalised averaged standard deviation is around 0.6, indicating that in Regime 3, wall thickness variations in the circumferential direction have a more pronounced influence on coherent noise levels than those in the axial direction.

Notably, the amplitude of the T(0,1) wave mode in Regime 3 is smaller than that of the F(1,m) family wave modes, suggesting that the contribution of wave scattering from the uneven pipe wall to coherent noise levels has diminished significantly. Instead, changes in the non-symmetric pipe cross-section due to wall thickness variations have a more pronounced influence on the excitation of different wave modes. This results in a distributed range of amplitudes for different wave modes around the reference case amplitude, as illustrated in Figures 5.7d to 5.7f. This phenomenon aligns with the earlier observation that wall thickness variations in the circumferential direction have a greater impact on coherent noise levels than those in the axial direction within Regime 3. The combined evidence underscores the shift in dominant factors affecting wave propagation and coherent noise in this regime.

5.5 Summary

This chapter investigates the coherent noise features of guided wave signals collected from pipes with inherent wall thickness variations, for practical considerations in guided wave pipe monitoring. An examination of wall thickness variations in seamless pipes, based on two specimens used throughout this thesis, reveals that the variation patterns can differ significantly depending on the manufacturing process. This difference is quantitatively evident from the varying correlation lengths of wall thickness variations in the pipe's axial and circumferential directions. Realistic pipe structures with wall thickness variations within industry-specified tolerances are modelled in FE simulations with different spatial correlations. The impact of these wall thickness variations on guided wave signals is analysed across three distinct regimes, each characterised by specific statistical measures, to elucidate the underlying mechanisms influencing wave excitation and propagation.

Wall thickness variations impact guided wave signals in two primary aspects: altering the excitation of different wave modes due to non-symmetric conditions and causing wave scattering from uneven pipe walls. In Regime 1, where wall thickness variations have similar small correlation lengths in axial and circumferential directions, the probability of increased coherent noise levels decreases with the axial correlation length, with wave scattering from uneven pipe walls dominating the contribution to coherent noise. Regime 2 is characterised by small circumferential correlation lengths but increasing axial correlation lengths. Here, the average standard deviation of wall thickness variations becomes a more appropriate measure when the correlation length approaches the pipe's geometric size. In this regime, the probability of increased coherent noise levels correlates with the average standard deviation of axial wall thickness variations. The non-symmetric pipe cross-section resulting from these variations significantly influences the excitation of different wave modes, thereby affecting coherent noise levels. In Regime 3, featuring large correlation lengths in both circumferential and axial directions, circumferential spatial correlations exert a more pronounced influence on coherent noise levels than axial correlations. This is primarily due to the impact on wave mode excitation caused by non-symmetric pipe cross-sections. In this regime, wave scattering from uneven pipe walls contributes negligibly to coherent noise in guided wave signals.

This chapter provides novel insights into the influence of a pipe's initial geometric imperfections on guided wave signals and elucidates the mechanisms by which pipe wall thickness variations affect guided wave behaviours. From the perspective of high-fidelity digital twin modelling for guided wave pipe monitoring, it offers modelling methods and quantitative evidence. These findings guide decisions on whether to incorporate initial pipe conditions, resulting from either manufacturing processes or early-stage corrosion, into digital twin models for more accurate reliability estimation. The decision is based on the quantitative influence of these conditions on the coherent noise levels of guided wave signals.

Chapter 6

Conclusion

6.1 Thesis review

This thesis presents a realistic numerical framework, namely a digital twin, focusing on the reliability estimation of guided wave SHM systems used in pipe monitoring. Chapter 1 provides an overview of the background and motivations behind the development of this framework. The primary contributions include: (a) a methodology for analysing noise characteristics in real guided wave signals, with emphasis on coherent and random noise; (b) a novel numerical framework for generating realistic signals that incorporates both random noise and coherent noise induced by transducer performance imbalances; (c) a digital twin-based reliability estimation framework that enables time-evolving, structure-specific, and environment-specific performance evaluations of SHM systems; and (d) insights into the influence of wall thickness variations in pipes on the noisiness of guided wave signals and the mechanisms by which they affect guided wave behaviours.

Chapter 2 introduces a methodology for analysing random and coherent noise, which is based and executed on laboratory experimental signals. Coherent noise is examined through mode analysis, focusing on transducer performance imbalance. This noise is found to be contributed to by both circumferential and axial flexural wave modes. The primary contributing flexural wave modes are identified via a spatial Fourier transform of transducer performance variations within the transducer ring and mode analysis based on ToFs. Random noise is analysed using statistical methods, including moment analysis, spectrum analysis, and channel dependency analysis. It is found that random noise in guided wave signals collected in the laboratory can be effectively modelled as Gaussian white noise with limited bandwidth. This analysis forms the basis for modelling noise features in the realistic numerical model in subsequent chapters.

Chapter 3 develops a realistic numerical framework designed to generate data for the reliability estimation of SHM systems. A key component of this framework is the incorporation of random and coherent noise. Random noise is modelled based on its statistical characteristics, while coherent noise is addressed through the estimation of transfer functions of imbalanced transducers. The framework is initially tested on numerical data, demonstrating that the estimation of the transducer transfer functions using CSM data generally provides a good assessment of transducer performance, though larger deviations occur when variations in transducer response become too significant. The comparison of synthetic T(0,1) guided wave signals with experimental signals demonstrates that the framework effectively captures the noise features of real guided wave signals, achieving strong comparability in both the appearance and levels of coherent noise.

The proposed framework is applied to generate data for estimating the inspection range of an SHM system for pipe monitoring under practical conditions. This approach offers a more accurate estimation of system performance by incorporating noise features, compared to common industrial practices and traditional ideal simulations, which do not capture the more complex, yet important in terms of reliability estimation, phenomena discussed in this thesis. Additionally, it is demonstrated that an efficient coherent noise reduction in guided wave signals can be achieved by compensating for transducer performance imbalances, using the transducer transfer functions estimated in the proposed framework.

In Chapter 4, a digital twin-based reliability estimation framework is detailed to provide timely performance evaluations of SHM systems, considering dynamic environmental conditions throughout their lifecycle. The digital twin model is established by estimating key simulation parameters, such as material properties, transducer performance, and random noise features, from a single set of representative experimental data. The validity of this method is demonstrated using experimental data collected from both laboratory instruments and commercial transducer rings, accounting for temperature variations. The framework's performance in reliability estimation is verified by comparing the POD analysis with that based on the established superposition method. Finally, the chapter illustrates the framework's ability to offer a time-evolving performance evaluation of an SHM system, specifically addressing dynamic temperature and transducer degradation conditions over the entire lifecycle.

Chapter 5 investigates the impact of initial geometric imperfections, specifically wall thickness variations, on guided wave signals, thereby on the reliability of SHM systems in monitoring real-world pipes. The study examines the wall thickness variations of pipes used throughout this thesis, revealing significant differences in variation patterns depending on the manufacturing process, as evidenced by varying correlation lengths in the axial and circumferential directions. The impact of these variations on guided wave signals is analysed through FE simulations, with a focus on the coherent noise levels.

It is found that wall thickness variations affect coherent noise levels in guided wave signals through two main mechanisms: altering wave mode excitation and causing wave scattering. The relative contributions of these mechanisms depend on the spatial correlation characteristics of the wall thickness variations, which can be categorised into three regimes.

6.2 Main findings

Unlike traditional model-assisted methods in the NDE field, which rely on assumptions about a wide range of input parameters, the novel framework proposed in this thesis offers a feasible solution for aiding the reliability estimation of SHM systems via numerical modelling, by dynamic updating a digital twin model with timely in-situ experimental data. This approach reflects the evolving nature of an SHM system's performance throughout its lifecycle. This framework has been demonstrated to estimate the reliability of an SHM system over its entire lifecycle, taking into account temperature variations and transducer degradation.

This thesis also presents a noise analysis methodology to better understand random and coherent noise in practical guided wave signals. By collecting a representative guided wave signal from the SHM system, statistical analysis of random noise provides key parameters for modelling it in simulations, including statistical moments, spectral characteristics, and bandwidth limitations. Coherent noise analysis, considering transducer performance imbalances, reveals the contributions of circumferential and axial flexural waves in different modes to coherent noise. This understanding aids in modelling coherent noise features in simulations by incorporating transducer imbalance. Additionally, these insights offer potential solutions for noise reduction in guided wave signals, as demonstrated with experimental data in this thesis.

Modelling realistic guided wave signals has gained attention to address the data scarcity problem in the NDE and SHM community. This is often achieved by superimposing simulated defect features onto experimentally collected signals or adding Gaussian white noise to ideal simulation signals. Based on the noise features explored in this thesis, a more efficient and realistic solution is developed by incorporating random and coherent noise into a numerical framework. In the context of guided wave testing, an accurate method to estimate transducer performance using transfer functions has been formulated, enabling faithful modelling of coherent noise in simulations. The strong compatibility between the synthetic signals generated by the proposed framework and experimental signals ensures an accurate estimation of system performance by considering practical measurement conditions. For instance, when estimating the inspection range of an SHM system, the framework provides quantitative estimates through POD curves at various inspection locations. This offers more detailed and quantitative information compared to the single-value estimates typical in current industrial practice and reveals a more accurate location dependence of system performance compared to that based on traditional ideal simulations.

The performance of an SHM system is characterised by its evolution over time. It depends not only on the instrumentation itself but also on installation conditions, the structure under inspection, and environmental factors, all of which change throughout the system's lifecycle. To address this, the thesis introduces a digital twin-based reliability estimation framework that dynamically updates to provide timely assessments of system performance throughout its lifecycle. For the digital twin model, in addition to estimating noise features and transducer performance, this framework includes a method for assessing material properties using full matrix guided wave signals to account for temperature variations. This approach offers global wave velocity estimation without needing additional instrumentation or transducer configuration, compared to traditional high-frequency bulk wave methods. The proposed framework has demonstrated its accuracy in estimating SHM system performance under temperature variations compared to established superposition methods, while providing greater flexibility for various scenarios, such as investigating multiple defects. Furthermore, the framework offers a time-evolving reliability estimation throughout the system's lifecycle, as demonstrated with laboratory-collected data, considering temperature variations and transducer degradation.

Lastly, this thesis provides insights into how initial wall thickness variations of pipes affect guided wave behaviours and influence the coherent noise level of guided wave signals. The wall thickness variations are categorised into three regimes based on the correlation lengths in axial and circumferential directions. This categorisation allows for estimating the impact of these variations on coherent noise levels and the relative contributions of two primary mechanisms: altering wave mode excitation and causing wave scattering. These findings provide quantitative evidence to inform decisions on incorporating initial pipe conditions in the realistic modelling of guided wave signals, according to the significance of these conditions in contributing to coherent noise levels.

6.3 Future work

This thesis has demonstrated the promising potential of a realistic numerical framework to provide a solution for the reliability estimation of SHM systems under practical measurement conditions. The encouraging results presented have laid the groundwork for several potential future investigations, which are outlined below.

In this study, practical factors commonly encountered in guided wave monitoring, such as transducer performance imbalance and temperature variations, were investigated in a laboratory environment. The uncertainty in field testing is undoubtedly broader, and more factors should be incorporated for a more flexible implementation of the proposed framework across wider application scenarios. For example, many pipes of interest are used to carry fluid or are immersed in seawater, such as subsea pipelines [180, 181]. Therefore, incorporating the fluid component in the numerical model is essential, which is achievable using the fluid-solid simulation module in Pogo [182]. The current numerical framework can be adapted to include random and coherent noise in the simulation data. However, the components of coherent noise are more complex due to the leakage of flexural wave modes into the fluid and the presence of new wave modes [183], posing challenges in accurately estimating the transducer transfer function using the method proposed in this thesis, which relies on separating a pure wave mode. Thus, the transducer performance estimation method needs further improvement to handle cases where a pure wave mode is difficult to separate.

Another area worth exploring is the improvement of simulation efficiency, especially in the context of reliability estimation where large data sets are needed. Although Pogo has significantly reduced computation time, further reduction by leveraging the features of POD analysis is attractive, particularly when defects of interest are similar in shape and small in size compared to the entire structure under inspection. A hybrid method combining localised FE models and the theoretical boundary integral method, based on the reciprocity principle, has been successfully developed to improve simulation efficiency in modelling scattered high-frequency bulk waves [184]. For modelling guided wave scattering from small defects on large structures, the reciprocity principle [110] and Born approximation [185] can be utilised to calculate wave scattering from defects based on the wavefield of an intact structure. Furthermore, wave scattering from larger defects can be extrapolated from smaller defects, assuming the defects are small and the response is linear to changes in defect parameters. The efficient hybrid simulation model for reliability estimation is currently under investigation by the author, and some ideas will be implemented in future work.

Apart from the application in reliability estimation, the realistic digital twin model has the potential to address practical challenges in guided wave monitoring, such as environmental condition variations like temperature and humidity. Instead of compensating guided wave signals using traditional methods like BSS method for temperature compensation, a real-time baseline signal can be generated by the digital twin model to identify structural changes. This approach has been explored by the author to detect defects under temperature variations using a simple baseline subtraction method. However, a point-by-point subtraction in the time domain between the baseline signal and measurement data shows limited performance, especially with small defects, due to unavoidable discrepancies in coherent noise waveforms. For further exploration, a data-driven method, such as the ICA method [186], can be developed to better distinguish signal changes from defects versus benign environmental condition changes. The digital twin model can be effectively exploited to generate realistic data for this purpose, promising more robust and reliable performance.

The work presented in this thesis lays a strong foundation for extending the digital twin-based reliability estimation framework to industrial environments. This framework can be integrated into existing commercial systems, such as the gPIMS system developed by GUL, to provide a quantitative confidence level for defect detection throughout the lifecycle of SHM systems.

References

[1] Mordor Intelligence, “Non-destructive testing market size & share analysis - growth trends & forecasts (2025 - 2030).” `https://www.mordorintelligence.com/industry-reports/global-non-destructive-testing-market-industry`, 2024. Accessed: January 20, 2025.

[2] MarketsandMarkets, “Ultrasonic testing market size, share and trends.” `https://www.marketsandmarkets.com/Market-Reports/ultrasonic-testing-market-131229239.html`, November 2024. Accessed: April 20, 2025. Report Code: SE 4519. Forecast period: 2024–2029.

[3] J. Zhang, M. Sun, L. Qin, D. Lin, C. Liu, J. Li, C. Li, S. Wen, and C. Han, “In-line inspection methods and tools for oil and gas pipeline: A review,” *International Journal of Pressure Vessels and Piping*, vol. 214, p. 105409, 2025.

[4] J. Huang, P. Chen, R. Li, K. Fu, Y. Wang, J. Duan, and Z. Li, “Systematic evaluation of ultrasonic in-line inspection techniques for oil and gas pipeline defects based on bibliometric analysis,” *Sensors*, vol. 24, no. 9, p. 2699, 2024.

[5] W. M. Alobaidi, E. A. Alkuam, H. M. Al-Rizzo, and E. Sandgren, “Applications of ultrasonic techniques in oil and gas pipeline industries:

A review," *American Journal of Operations Research*, vol. 5, no. 4, pp. 274–287, 2015.

[6] J. Jodhani, A. Handa, A. Gautam, Ashwni, and R. Rana, "Ultrasonic non-destructive evaluation of composites: A review," *Materials Today: Proceedings*, vol. 78, pp. 627–632, 2023. 3rd Biennial International Conference on Future Learning Aspects of Mechanical Engineering (FLAME 2022).

[7] S. Gholizadeh, "A review of non-destructive testing methods of composite materials," *Procedia Structural Integrity*, vol. 1, pp. 50–57, 2016. XV Portugese Conference on Fracture, PCF 2016, 10-12 February 2016, Paco de Arcos, Portugal.

[8] M. E. Torbalı, A. Zolotas, and N. P. Avdelidis, "A state-of-the-art review of non-destructive testing image fusion and critical insights on the inspection of aerospace composites towards sustainable maintenance repair operations," *Applied Sciences*, vol. 13, no. 4, p. 2732, 2023.

[9] P. Cawley, "Guided waves in long-range nondestructive testing and structural health monitoring: Principles, history of applications and prospects," *NDT & E International*, vol. 142, no. 103026, 2023.

[10] P. Cawley, "Practical long range guided wave inspection—managing complexity," in *AIP Conference Proceedings*, vol. 657, pp. 22–40, American Institute of Physics, 2003.

[11] M. J. S. Lowe, D. N. Alleyne, and P. Cawley, "The Mode Conversion of a Guided Wave by a Part-Circumferential Notch in a Pipe," *Journal of Applied Mechanics*, vol. 65, pp. 649–656, 09 1998.

[12] R. Guan, Y. Lu, W. Duan, and X. Wang, "Guided waves for damage identification in pipeline structures: A review," *Structural control and*

health monitoring, vol. 24, no. 11, p. e2007, 2017.

[13] X. Zang, Z.-D. Xu, H. Lu, C. Zhu, and Z. Zhang, "Ultrasonic guided wave techniques and applications in pipeline defect detection: A review," *International Journal of Pressure Vessels and Piping*, p. 105033, 2023.

[14] M. El Mountassir, S. Yaacoubi, and F. Dahmene, "Reducing false alarms in guided waves structural health monitoring of pipelines: Review synthesis and debate," *International Journal of Pressure Vessels and Piping*, vol. 188, p. 104210, 2020.

[15] A. J. Croxford, P. D. Wilcox, B. W. Drinkwater, and G. Konstantinidis, "Strategies for guided-wave structural health monitoring," *Proceedings of the Royal Society A: Mathematical, Physical and Engineering Sciences*, vol. 463, no. 2087, pp. 2961–2981, 2007.

[16] P. Cawley, F. Cegla, and A. Galvagni, "Guided waves for NDT and permanently-installed monitoring," *Insight-Non-Destructive Testing and Condition Monitoring*, vol. 54, no. 11, pp. 594–601, 2012.

[17] S. Mariani, T. Vogt, S. Heinlein, and P. Cawley, "The performance of a guided wave pipe monitoring system over extended periods of field operation," *Materials Evaluation*, vol. 81, no. 8, 2023.

[18] V. Giurgiutiu and C. Soutis, "Guided wave methods for structural health monitoring," *Encyclopedia of aerospace engineering*, 2010.

[19] T. Vogt, S. Heinlein, J. Milewczyk, S. Mariani, R. Jones, and P. Cawley, "Guided wave monitoring of industrial pipework – improved sensitivity system and field experience," in *European Workshop on Structural Health Monitoring*, pp. 819–829, Springer International Publishing, 2021.

[20] P. Cawley, “Ultrasonic structural health monitoring - current applications and potential,” in *2019 IEEE International Ultrasonics Symposium (IUS)*, (Glasgow, UK), IEEE, October 2019. Date of Conference: 06-09 October 2019.

[21] P. Cawley, “A development strategy for structural health monitoring applications,” *Journal of Nondestructive Evaluation, Diagnostics and Prognostics of Engineering Systems*, vol. 4, no. 4, p. 041012, 2021.

[22] O. Mesnil, B. Chapuis, and T. Druet, “Guided waves for structural health monitoring,” in *56th Annual Conference of the British Institute of Non-Destructive Testing, NDT 2017*, British Institute of Non-Destructive Testing, 2017.

[23] U. D. of Defense, “Department of defense handbook: Nondestructive evaluation system reliability assessment,” Tech. Rep. MIL-HDBK-1823A, Department of Defense, United States, April 2009.

[24] Model-Assisted POD Working Group, “Model-assisted pod working group.” `https://static.cnde.iastate.edu/mapod`. Accessed: 15/09/2021.

[25] R. B. Thompson, L. J. Brasche, E. Lindgren, P. Swindell, and W. P. Winfree, “Recent advances in model-assisted probability of detection,” in *4th European-American workshop on reliability of NDE*, no. LF99-9094, 2009.

[26] X. Du and L. Leifsson, “Multifidelity model-assisted probability of detection via cokriging,” *NDT & E International*, vol. 108, p. 102156, 2019.

[27] B. Yilmaz, D. Smagulova, and E. Jasiuniene, “Model-assisted reliability assessment for adhesive bonding quality evaluation with ultrasonic

ndt," *NDT & E International*, vol. 126, p. 102596, 2022.

[28] P. Calmon, S. Sharma, O. Mesnil, and B. Chapuis, "Experimental validation of MAPOD methodology for SHM applied to the detection of growing cracks in a metallic part (Conference Presentation)," in *8th International Workshop on Reliability of NDT/NDE* (D. Kanzler and N. G. Meyendorf, eds.), vol. PC12491, p. PC1249105, International Society for Optics and Photonics, SPIE, 2023.

[29] F. Falcetelli, N. Yue, L. Rossi, G. Bolognini, F. Bastianini, D. Zarouchas, and R. Di Sante, "A model-assisted probability of detection framework for optical fiber sensors," *Sensors*, vol. 23, no. 10, p. 4813, 2023.

[30] P. Huthwaite, "Accelerated finite element elastodynamic simulations using the gpu," *Journal of Computational Physics*, vol. 257, pp. 687–707, 2014.

[31] J. B. Harley, C. Liu, I. J. Oppenheim, and J. M. Moura, "Managing complexity, uncertainty, and variability in guided wave structural health monitoring," *SICE Journal of Control, Measurement, and System Integration*, vol. 10, no. 5, pp. 325–336, 2017.

[32] A. J. Croxford, P. D. Wilcox, Y. Lu, J. Michaels, and B. W. Drinkwater, "Quantification of environmental compensation strategies for guided wave structural health monitoring," in *Health Monitoring of Structural and Biological Systems 2008*, vol. 6935, pp. 136–146, SPIE, 2008.

[33] Y. Lu and J. E. Michaels, "Feature extraction and sensor fusion for ultrasonic structural health monitoring under changing environmental conditions," *IEEE Sensors Journal*, vol. 9, no. 11, pp. 1462–1471, 2009.

[34] S. Mariani, S. Heinlein, and P. Cawley, "Location specific temperature

compensation of guided wave signals in structural health monitoring," *IEEE Transactions on Ultrasonics, Ferroelectrics, and Frequency Control*, vol. 67, no. 1, pp. 146–157, 2019.

[35] C. Liu, J. Dobson, and P. Cawley, "Efficient generation of receiver operating characteristics for the evaluation of damage detection in practical structural health monitoring applications," *Proceedings of the Royal Society A: Mathematical, Physical and Engineering Sciences*, vol. 473, no. 2199, p. 20160736, 2017.

[36] W. Zhou and J. Bao, "Uncertainty quantification of wall thickness of onshore gas transmission pipelines," *Canadian Journal of Civil Engineering*, vol. 48, no. 9, pp. 1206–1214, 2021.

[37] D. C. Gazis, "Three-dimensional investigation of the propagation of waves in hollow circular cylinders. i. analytical foundation," *The journal of the Acoustical Society of America*, vol. 31, no. 5, pp. 568–573, 1959.

[38] J. Zemanek Jr, "An experimental and theoretical investigation of elastic wave propagation in a cylinder," *The Journal of the Acoustical society of America*, vol. 51, no. 1B, pp. 265–283, 1972.

[39] J. L. Rose, *Ultrasonic guided waves in solid media.* Cambridge University Press, 2014.

[40] B. A. Auld, *Acoustic Fields and Waves in Solids.* Krieger Publishing Company, 1990.

[41] B. N. Pavlakovic, *Leaky Guided Ultrasonic Waves in NDT.* Phd thesis, Imperial College London, London, UK, 1999.

[42] B. Pavlakovic, M. Lowe, D. Alleyne, and P. Cawley, "Disperse: A general purpose program for creating dispersion curves," *Review of Progress*

in Quantitative Nondestructive Evaluation: Volume 16A, pp. 185–192, 1997.

[43] M. Silk and K. Bainton, "The propagation in metal tubing of ultrasonic wave modes equivalent to lamb waves," *Ultrasonics*, vol. 17, no. 1, pp. 11–19, 1979.

[44] The American Society of Mechanical Engineers, "B36.10M - Welded and Seamless Wrought Steel Pipe." PDF, Order No. M0311T, 2018. Available at: `https://www.asme.org/codes-standards/find-codes-standards/b36-10m-welded-seamless-wrought-steel-pipe/2018/pdf`.

[45] M. Lowe and P. Cawley, "Long range guided wave inspection usage – current commercial capabilities and research directions," tech. rep., Department of Mechanical Engineering, Imperial College London, March 2006.

[46] P. D. Wilcox, "Omni-directional guided wave transducer arrays for the rapid inspection of large areas of plate structures," *IEEE transactions on ultrasonics, ferroelectrics, and frequency control*, vol. 50, no. 6, pp. 699–709, 2003.

[47] R. H. Herrera, J. Nustes, D. Nguyen, and A. Elvers, "Interpolated plane wave imaging: Ipwi," *NDT.net*, 2023.

[48] G. Liu and J. Qu, "Guided circumferential waves in a circular annulus," *Journal of Applied Mechanics*, vol. 65, pp. 424–430, June 1998.

[49] E. C. Rodgers, S. Mariani, and P. Cawley, "The use of circumferential guided waves to monitor axial cracks in pipes," *Structural Health Monitoring*, vol. 22, no. 4, pp. 2609–2625, 2023.

[50] R. Howard and F. Cegla, “Detectability of corrosion damage with circumferential guided waves in reflection and transmission,” *NDT & E International*, vol. 91, pp. 108–119, 2017.

[51] M. Clough, M. Fleming, and S. Dixon, “Circumferential guided wave emat system for pipeline screening using shear horizontal ultrasound,” *Ndt & E International*, vol. 86, pp. 20–27, 2017.

[52] J. Fong and T. Pialucha, “Quantitative short range guided wave system,” in *15th Asia Pacific Conf. for Non-Destructive Testing*, 2017.

[53] X. Zhao and J. L. Rose, “Guided circumferential shear horizontal waves in an isotropic hollow cylinder,” *The Journal of the Acoustical Society of America*, vol. 115, no. 5, pp. 1912–1916, 2004.

[54] J. Davies, F. Simonetti, M. Lowe, and P. Cawley, “Review of synthetically focused guided wave imaging techniques with application to defect sizing,” in *AIP conference proceedings*, vol. 820, pp. 142–149, American Institute of Physics, 2006.

[55] S. Mariani, S. Heinlein, and P. Cawley, “Compensation for temperature-dependent phase and velocity of guided wave signals in baseline subtraction for structural health monitoring,” *Structural Health Monitoring*, vol. 19, no. 1, pp. 26–47, 2020.

[56] I. D. Khurjekar and J. B. Harley, “Accounting for physics uncertainty in ultrasonic wave propagation using deep learning,” *arXiv preprint arXiv:1911.02743*, 2019.

[57] C. Birnie, K. Chambers, D. Angus, and A. L. Stork, “Analysis and models of pre-injection surface seismic array noise recorded at the aquistore carbon storage site,” *Geophysical Journal International*, vol. 206, no. 2, pp. 1246–1260, 2016.

[58] W. L. Martinez and A. R. Martinez, *Computational Statistics Handbook with MATLAB*. Boca Raton, FL, USA: CRC Press, Taylor & Francis Group, 3rd ed., 2016.

[59] "MakeItFrom." `https://www.makeitfrom.com/material-properties/EN-1.0425-P265GH-Non-Alloy-Steel`. EN 1.0425 P265GH Non-Alloy Steel Material Properties.

[60] M. J. S. Lowe, D. N. Alleyne, and P. Cawley, "The mode conversion of a guided wave by a part-circumferential notch in a pipe," *Journal of Applied Mechanics*, vol. 65, pp. 649–656, 09 1998.

[61] P. Zuo and P. Huthwaite, "Quantitative mapping of thickness variations along a ray path using geometrical full waveform inversion and guided wave mode conversion," *Proceedings of the Royal Society A*, vol. 478, no. 2257, p. 20210602, 2022.

[62] I. D. Khurjekar and J. B. Harley, "Sim-to-real localization: Environment resilient deep ensemble learning for guided wave damage localization," *The Journal of the Acoustical Society of America*, vol. 151, no. 2, pp. 1325–1336, 2022.

[63] M. Bertovic and I. Virkkunen, "NDE 4.0: new paradigm for the nde inspection personnel," in *Handbook of Nondestructive Evaluation 4.0*, pp. 239–269, Springer, 2022.

[64] EXTENDE, "TraiNDE RT v1.1 - the virtual and innovative training tool for NDE inspectors," *e-Journal of Nondestructive Testing*, vol. 27, no. 7, 2022.

[65] A. B. Abdessalem, F. Jenson, and P. Calmon, "Quantifying uncertainty in parameter estimates of ultrasonic inspection system using bayesian

computational framework," *Mechanical Systems and Signal Processing*, vol. 109, pp. 89–110, 2018.

[66] S. Sikdar and S. Banerjee, "Guided wave based nondestructive analysis of localized inhomogeneity effects in an advanced sandwich composite structure," *Composites Part B: Engineering*, vol. 176, p. 107195, 2019.

[67] J. Shah, S. El-Hawwat, and H. Wang, "Guided wave ultrasonic testing for crack detection in polyethylene pipes: Laboratory experiments and numerical modeling," *Sensors*, vol. 23, no. 11, p. 5131, 2023.

[68] P. Petcher and S. Dixon, "Mode mixing in shear horizontal ultrasonic guided waves," *Nondestructive testing and Evaluation*, vol. 32, no. 2, pp. 113–132, 2017.

[69] D. A. Ramatlo, C. S. Long, P. W. Loveday, and D. N. Wilke, "A modelling framework for simulation of ultrasonic guided wave-based inspection of welded rail tracks," *Ultrasonics*, vol. 108, p. 106215, 2020.

[70] C. A. Leckey, K. R. Wheeler, V. N. Hafiychuk, H. Hafiychuk, and D. A. Timuçin, "Simulation of guided-wave ultrasound propagation in composite laminates: Benchmark comparisons of numerical codes and experiment," *Ultrasonics*, vol. 84, pp. 187–200, 2018.

[71] W. L. Oberkampf, J. C. Helton, C. A. Joslyn, S. F. Wojtkiewicz, and S. Ferson, "Challenge problems: uncertainty in system response given uncertain parameters," *Reliability Engineering & System Safety*, vol. 85, no. 1-3, pp. 11–19, 2004.

[72] R. J. Pyle, R. R. Hughes, A. A. S. Ali, and P. D. Wilcox, "Uncertainty quantification for deep learning in ultrasonic crack characterization," *IEEE Transactions on Ultrasonics, Ferroelectrics, and Frequency Control*, vol. 69, no. 7, pp. 2339–2351, 2022.

[73] A. R. Diogo, B. Moreira, C. A. Gouveia, and J. M. R. Tavares, "A review of signal processing techniques for ultrasonic guided wave testing," *Metals*, vol. 12, no. 6, p. 936, 2022.

[74] P. D. Wilcox, "A rapid signal processing technique to remove the effect of dispersion from guided wave signals," *IEEE transactions on ultrasonics, ferroelectrics, and frequency control*, vol. 50, no. 4, pp. 419–427, 2003.

[75] A. Douglass, D. O. Adams, C. Deemer, and J. B. Harley, "Singular value-based damage statistics for guided wave structural health monitoring," in *AIP Conference Proceedings*, vol. 2102, AIP Publishing, 2019.

[76] S. Ahmed and F. Kopsaftopoulos, "Uncertainty quantification of guided waves propagation for active sensing structural health monitoring," in *Proceedings of the Vertical Flight Society 75th Annual Forum & Technology Display*, Philadelphia, PA, USA, 2019.

[77] I. N. Giannakeas, Z. S. Khodaei, and M. Aliabadi, "Digital clone testing platform for the assessment of SHM systems under uncertainty," *Mechanical Systems and Signal Processing*, vol. 163, p. 108150, 2022.

[78] Z. Yang, H. Yang, T. Tian, D. Deng, M. Hu, J. Ma, D. Gao, J. Zhang, S. Ma, L. Yang, *et al.*, "A review in guided-ultrasonic-wave-based structural health monitoring: From fundamental theory to machine learning techniques," *Ultrasonics*, p. 107014, 2023.

[79] J. B. Harley and D. Sparkman, "Machine learning and nde: Past, present, and future," in *AIP conference proceedings*, vol. 2102, AIP Publishing, 2019.

[80] J. S. Hall and J. E. Michaels, "Adaptive dispersion compensation

for guided wave imaging," in *AIP Conference Proceedings*, vol. 1430, pp. 623–630, American Institute of Physics, 2012.

[81] C. Liu, J. B. Harley, M. Bergés, D. W. Greve, and I. J. Oppenheim, "Robust ultrasonic damage detection under complex environmental conditions using singular value decomposition," *Ultrasonics*, vol. 58, pp. 75–86, 2015.

[82] A. Amer and F. P. Kopsaftopoulos, "Statistical guided-waves-based structural health monitoring via stochastic non-parametric time series models," *Structural Health Monitoring*, vol. 21, no. 3, pp. 1139–1166, 2022.

[83] K. S. Alguri, J. E. Michaels, and J. B. Harley, "Robust baseline subtraction for ultrasonic full wavefield analysis," in *AIP Conference Proceedings*, vol. 1806, AIP Publishing, 2017.

[84] K. Yang, S. Kim, R. Yue, H. Yue, and J. B. Harley, "Long-term guided wave structural health monitoring in an uncontrolled environment through long short-term principal component analysis," *Structural Health Monitoring*, vol. 21, no. 4, pp. 1501–1517, 2022.

[85] I. D. Khurjekar and J. B. Harley, "Closing the sim-to-real gap in guided wave damage detection with adversarial training of variational auto-encoders," in *ICASSP 2022-2022 IEEE International Conference on Acoustics, Speech and Signal Processing (ICASSP)*, pp. 3823–3827, IEEE, 2022.

[86] D. A. Ramatlo, D. N. Wilke, and P. W. Loveday, "Digital twin hybrid modeling for enhancing guided wave ultrasound inspection signals in welded rails," *Mathematical and Computational Applications*, vol. 28, no. 2, p. 58, 2023.

[87] D. A. Ramatlo, D. N. Wilke, and P. W. Loveday, "A data-driven hybrid approach to generate synthetic data for unavailable damage scenarios in welded rails for ultrasonic guided wave monitoring," *Structural Health Monitoring*, vol. 23, pp. 1890–1913, May 2024.

[88] L. Peng, S. Li, H. Sun, and S. Huang, "A pipe ultrasonic guided wave signal generation network suitable for data enhancement in deep learning: US-WGAN," *Energies*, vol. 15, no. 18, p. 6695, 2022.

[89] F. Luleci, F. N. Catbas, and O. Avci, "Generative adversarial networks for data generation in structural health monitoring," *Frontiers in Built Environment*, vol. 8, p. 816644, February 2022.

[90] M. Heesch, M. Dziendzikowski, K. Mendrok, and Z. Dworakowski, "Diagnostic-quality guided wave signals synthesized using generative adversarial neural networks," *Sensors*, vol. 22, no. 10, p. 3848, 2022.

[91] H. Chen, "Challenges and corresponding solutions of generative adversarial networks (GANs): a survey study," in *Journal of Physics: Conference Series*, vol. 1827, p. 012066, IOP Publishing, 2021.

[92] H. A. Bloxham, A. Velichko, and P. D. Wilcox, "Combining simulated and experimental data to simulate ultrasonic array data from defects in materials with high structural noise," *IEEE transactions on ultrasonics, ferroelectrics, and frequency control*, vol. 63, no. 12, pp. 2198–2206, 2016.

[93] B. Herdovics and F. Cegla, "Compensation of phase response changes in ultrasonic transducers caused by temperature variations," *Structural Health Monitoring*, vol. 18, no. 2, pp. 508–523, 2019.

[94] L. Schmerr, A. Lopez-Sanchez, and R. Huang, "Complete ultrasonic transducer characterization and its use for models and measurements,"

Ultrasonics, vol. 44, pp. e753–e757, 2006.

[95] A. L. L. Sánchez and L. W. S. Jr., "Characterization of an ultrasonic nondestructive measurement system," in *Simposio de Metrología*, (Querétaro, Mexico), Centro Nacional de Metrología (CENAM), October 2006.

[96] A. L. L. Sánchez, *Ultrasonic System Models and Measurements.* Phd thesis, Iowa State University, Ames, IA, January 2005.

[97] N. Wiener, "The wiener RMS (Root Mean Square) error criterion in filter design and prediction," in *Extrapolation, Interpolation, and Smoothing of Stationary Time Series: With Engineering Applications*, pp. 129–148, MIT Press, 1964.

[98] T. Cicero, P. Cawley, F. Simonetti, and S. Rokhlin, "Potential and limitations of a deconvolution approach for guided wave structural health monitoring," *Structural Health Monitoring*, vol. 8, no. 5, pp. 381–395, 2009.

[99] M. B. Drozdz, *Efficient finite element modelling of ultrasound waves in elastic media.* PhD thesis, Imperial College London, 2008.

[100] F. Kara, J. Navarro, and R. L. Allwood, "Effect of thickness variation on collapse pressure of seamless pipes," *Ocean Engineering*, vol. 37, no. 11, pp. 998–1006, 2010.

[101] I. Pyshmintsev, I. Veselov, A. Yakovleva, M. Lobanov, and S. Danilov, "Evolution of the texture of low-carbon microalloyed pipe steel in the seamless pipe manufacturing process," in *AIP Conference Proceedings*, vol. 1785, AIP Publishing, 2016.

[102] J. Malachowski, V. Hutsaylyuk, P. Yukhumets, R. Dmitryenko, G. Beliaiev, and I. Prudkii, "Investigation of the stress-strain state of seamless

pipe in the initial state," *Archive of mechanical engineering*, vol. 61, no. 4, pp. 595–607, 2014.

[103] L. Gandossi and C. Annis, "Probability of detection curves: Statistical best-practices," *ENIQ report*, vol. 41, 2010.

[104] E. Leinov, M. J. Lowe, and P. Cawley, "Investigation of guided wave propagation and attenuation in pipe buried in sand," *Journal of Sound and Vibration*, vol. 347, pp. 96–114, 2015.

[105] "Standard practice for guided wave testing of above ground steel pipework using piezoelectric effect transduction," 2016. ASTM E2775-16.

[106] T. Vogt, B. Pavlakovic, and P. Cawley, "A multiple-echo calibration technique for guided wave testing," *Materials Evaluation*, vol. 80, no. 6, pp. 32–43, 2022.

[107] A. B. Bayoumi, I. Mueller, T. Vogt, and P. Kraemer, "Approaches combining multiple paths to establish the probability of detection of a guided wave-based structural health monitoring system," *Prague, Czech Republic, European NDT CM*, 2021.

[108] M. Rébillat, O. Hmad, F. Kadri, and N. Mechbal, "Peaks over threshold–based detector design for structural health monitoring: Application to aerospace structures," *Structural Health Monitoring*, vol. 17, no. 1, pp. 91–107, 2018.

[109] A. Demma, P. Cawley, M. Lowe, and A. Roosenbrand, "The reflection of the fundamental torsional mode from cracks and notches in pipes," *The Journal of the Acoustical Society of America*, vol. 114, no. 2, pp. 611–625, 2003.

[110] J. D. Achenbach, *Reciprocity in elastodynamics.* Cambridge University Press, 2003.

[111] F. Ling, H. Chen, Y. Lang, Z. Yang, K. Xu, and D. Ta, "Lamb wave tomography for defect localization using wideband dispersion reversal method," *Measurement*, vol. 216, p. 112965, 2023.

[112] F. Boßmann, G. Plonka, T. Peter, O. Nemitz, and T. Schmitte, "Sparse deconvolution methods for ultrasonic NDT: Application on TOFD and wall thickness measurements," *Journal of Nondestructive Evaluation*, vol. 31, pp. 225–244, 2012.

[113] P. Cawley, "Structural health monitoring: Closing the gap between research and industrial deployment," *Structural health monitoring*, vol. 17, no. 5, pp. 1225–1244, 2018.

[114] P. Lloyd, "Structural health monitoring systems–benefits and airworthiness issues," *The Aeronautical Journal*, vol. 112, no. 1131, pp. 285–289, 2008.

[115] V. Nerlikar, O. Mesnil, R. Miorelli, and O. D'Almeida, "Damage detection with ultrasonic guided waves using machine learning and aggregated baselines," *Structural Health Monitoring*, vol. 23, no. 1, pp. 443–462, 2024.

[116] X. L. Tu, R. J. Pyle, A. J. Croxford, and P. D. Wilcox, "Potential and limitations of NARX for defect detection in guided wave signals," *Structural Health Monitoring*, vol. 22, no. 3, pp. 1863–1875, 2023.

[117] S. Hassani and U. Dackermann, "A systematic review of optimization algorithms for structural health monitoring and optimal sensor placement," *Sensors*, vol. 23, no. 6, p. 3293, 2023.

[118] A. Güemes, A. Fernandez-Lopez, A. R. Pozo, and J. Sierra-Pérez, “Structural health monitoring for advanced composite structures: A review,” *Journal of Composites Science*, vol. 4, no. 1, p. 13, 2020.

[119] T. Vogt and M. Evans, “Reliability of guided wave testing,” in *4th European-American Workshop on Reliability of NDE - We.4.A.3*, DGZIP, 2009.

[120] S. S. Kessler, “Certifying a structural health monitoring system: Characterizing durability, reliability and longevity,” in *Proceedings of the 1st International Forum on Integrated Systems Health Engineering and Management in Aerospace*, (Napa, CA, USA), pp. 7–10, NASA Ames Research Center, Nov 2005.

[121] E. A. Lindgren, “SHM reliability and implementation–a personal military aviation perspective,” in *AIP Conference Proceedings*, vol. 1706, AIP Publishing, 2016.

[122] C. R. Farrar and K. Worden, “An introduction to structural health monitoring,” *Philosophical Transactions of the Royal Society A: Mathematical, Physical and Engineering Sciences*, vol. 365, no. 1851, pp. 303–315, 2007.

[123] S. Mishra, S. K. Yadav, and F.-K. Chang, “Reliability of probability of detection (POD) of fatigue cracks for built-in acousto-ultrasound technique as in-situ NDE,” in *Proceedings of the Structural Health Monitoring 2019 Conference*, DPI Proceedings, 2019.

[124] A. C. Cobb, J. E. Michaels, and T. E. Michaels, “Ultrasonic structural health monitoring: a probability of detection case study,” in *AIP Conference Proceedings*, vol. 1096, pp. 1800–1807, American Institute of Physics, 2009.

[125] V. Janapati, F. Kopsaftopoulos, F. Li, S. J. Lee, and F.-K. Chang, “Damage detection sensitivity characterization of acousto-ultrasound-based structural health monitoring techniques,” *Structural Health Monitoring*, vol. 15, no. 2, pp. 143–161, 2016.

[126] W. Q. Meeker, D. Roach, and S. S. Kessler, “Statistical methods for probability of detection in structural health monitoring,” in *Proceedings of the Structural Health Monitoring 2019 Conference*, DPI Proceedings, 2019.

[127] C. M. Schubert Kabban, B. M. Greenwell, M. P. DeSimio, and M. M. Derriso, “The probability of detection for structural health monitoring systems: Repeated measures data,” *Structural Health Monitoring*, vol. 14, no. 3, pp. 252–264, 2015.

[128] B. Shook, H. Millwater, M. Enright, S. Hudak Jr, and W. Francis, “Simulation of recurring automated inspections on probability-of-fracture estimates,” *Structural Health Monitoring*, vol. 7, no. 4, pp. 293–307, 2008.

[129] D. S. Forsyth, “Structural health monitoring and probability of detection estimation,” in *AIP Conference Proceedings*, vol. 1706, AIP Publishing, 2016.

[130] C. Mandache, M. Genest, M. Khan, and N. Mrad, “Considerations on structural health monitoring reliability,” in *Proceedings of the International Workshop Smart Materials, Structures & NDT in Aerospace, Montreal, QC, Canada*, vol. 24, 2011.

[131] A. Donner, “Linear regression analysis with repeated measurements,” *Journal of Chronic Diseases*, vol. 37, no. 6, pp. 441–448, 1984.

[132] E. O’Connor, “Quantifying method differences in predicting the prob-

ability of detection for structural health monitoring applications," *Engineering, Materials Science*, 2019.

[133] F. Falcetelli, N. Yue, R. Di Sante, and D. Zarouchas, "Probability of detection, localization, and sizing: The evolution of reliability metrics in structural health monitoring," *Structural Health Monitoring*, vol. 21, no. 6, pp. 2990–3017, 2022.

[134] I. Mueller, V. Memmolo, K. Tschöke, M. Moix-Bonet, K. Möllenhoff, M. Golub, R. S. Venkat, Y. Lugovtsova, A. Eremin, and J. Moll, "Performance assessment for a guided wave-based SHM system applied to a stiffened composite structure," *Sensors*, vol. 22, no. 19, p. 7529, 2022.

[135] W. Wu, S. Cantero-Chinchilla, D. Prescott, R. Remenyte-Prescott, and M. Chiachío, "A general approach to assessing SHM reliability considering sensor failures based on information theory," *Reliability Engineering & System Safety*, vol. 250, p. 110267, October 2024.

[136] J. C. Aldrin, E. A. Medina, E. A. Lindgren, C. Buynak, G. Steffes, and M. Derriso, "Model-assisted probabilistic reliability assessment for structural health monitoring systems," in *AIP Conference Proceedings*, vol. 1211, pp. 1965–1972, American Institute of Physics, 2010.

[137] V. Memmolo, F. Ricci, L. Maio, N. D. Boffa, and E. Monaco, "Model assisted probability of detection for a guided waves based SHM technique," in *Health Monitoring of Structural and Biological Systems 2016*, vol. 9805, pp. 38–49, SPIE, 2016.

[138] X. Du, J. Yan, S. Laflamme, L. Leifsson, Y. Tesfahunegn, and S. Koziel, "Model-assisted probability of detection for structural health monitoring of flat plates," in *Computational Science–ICCS 2018: 18th International Conference, Wuxi, China, June 11-13, 2018, Proceedings, Part*

II 18, pp. 618–628, Springer, 2018.

[139] P. Ochôa, R. M. Groves, and R. Benedictus, "Reliability analysis of an ultrasonic guided wave based structural health monitoring system for a carbon fibre reinforced thermoplastic torsion-box," *Proc. 11 th IWSHM, September*, pp. 12–14, 2017.

[140] F. Jenson, N. Dominguez, P. Willaume, and T. Yalamas, "A Bayesian approach for the determination of POD curves from empirical data merged with simulation results," in *AIP Conference Proceedings*, vol. 1511, pp. 1741–1748, American Institute of Physics, 2013.

[141] J. C. Aldrin, J. S. Knopp, and H. A. Sabbagh, "Bayesian methods in probability of detection estimation and model-assisted probability of detection evaluation," in *AIP Conference Proceedings*, vol. 1511, pp. 1733–1740, American Institute of Physics, 2013.

[142] S. Heinlein, P. Cawley, and T. Vogt, "Validation of a procedure for the evaluation of the performance of an installed structural health monitoring system," *Structural Health Monitoring*, vol. 18, no. 5-6, pp. 1557–1568, 2019.

[143] T. Clarke, F. Simonetti, and P. Cawley, "Guided wave health monitoring of complex structures by sparse array systems: Influence of temperature changes on performance," *Journal of Sound and Vibration*, vol. 329, no. 12, pp. 2306–2322, 2010.

[144] C. Liu, J. Harley, N. O'Donoughue, Y. Ying, M. H. Altschul, M. Bergés, J. H. Garrett, D. W. Greve, J. M. Moura, I. J. Oppenheim, *et al.*, "Robust change detection in highly dynamic guided wave signals with singular value decomposition," in *2012 IEEE International Ultrasonics Symposium*, pp. 483–486, IEEE, 2012.

[145] V. T. Pham, T. T. N. Pham, T. M. T. Luong, and H. N. Nguyen, "Effect of temperature on ultrasonic velocities, attenuations, reflection and transmission coefficients between motor oil and carbon steel estimated by pulse-echo technique of ultrasonic testing method," *VNU Journal of Science: Mathematics-Physics*, vol. 31, no. 4, 2015.

[146] S. F. Biagiotti, "Effect of temperature on ultrasonic velocity in steel," in *Proceedings of the Corrosion97 Conference*, (New Orleans, Louisiana), NACE International, March 1997.

[147] Y. Lu and J. E. Michaels, "A methodology for structural health monitoring with diffuse ultrasonic waves in the presence of temperature variations," *Ultrasonics*, vol. 43, no. 9, pp. 717–731, 2005.

[148] R. Gorgin, Y. Luo, and Z. Wu, "Environmental and operational conditions effects on lamb wave based structural health monitoring systems: A review," *Ultrasonics*, vol. 105, p. 106114, 2020.

[149] B. Droney and R. Klinman, "Ultrasonic techniques for determining the mechanical properties of steels," in *AIP Conference Proceedings*, vol. 84, pp. 210–228, American Institute of Physics, 1982.

[150] N. Rigas, O. Lypchanskyi, U. Prahl, and M. Merklein, "Ultrasound-assisted material characterization: An innovative method for the non-destructive in-situ detection of microstructural changes of high-strength aluminum alloys," *Journal of Materials Processing Technology*, vol. 325, p. 118282, 2024.

[151] S. Z. Khan, T. M. Khan, Y. F. Joya, M. A. Khan, S. Ahmed, and A. Shah, "Assessment of material properties of aisi 316l stainless steel using non-destructive testing," *Nondestructive testing and evaluation*, vol. 31, no. 4, pp. 360–370, 2016.

[152] A. Vary, “Ultrasonic characterization of material properties,” in *NDT Handbook, third edition: Vol. 7, Ultrasonic Testing*, ch. 8, North Olmsted, Ohio: NASA Lewis Research Center, 1980.

[153] I. N. Giannakeas, Z. Sharif-Khodaei, and M. Aliabadi, “On the estimation of material properties using guided wave measurements for the calibration of finite element models,” in *AIP Conference Proceedings*, vol. 2309, AIP Publishing, 2020.

[154] P. Pedregal, *Introduction to optimization*, vol. 46. Springer, 2004.

[155] M. R. Chernick, *Bootstrap Methods: A Guide for Practitioners and Researchers.* Wiley Series in Probability and Statistics, John Wiley & Sons, Inc., 2nd ed., April 2007.

[156] Matlab, “Visualize summary statistics with box plot.” `https://uk.mathworks.com/help/stats/boxplot.html`, 2024. Accessed: 24/04/2024.

[157] S. Heinlein, *Structural health monitoring of pipes using permanently installed guided wave sensors.* PhD thesis, Imperial College London, 2019.

[158] C. Fu, C. Gao, and W. Zhang, “A digital-twin framework for predicting the remaining useful life of piezoelectric vibration sensors with sensitivity degradation modeling,” *Sensors*, vol. 23, no. 19, p. 8173, 2023.

[159] O. Mesnil, R. Miorelli, X. Artusi, P. Calmon, B. Chapuis, and O. D’Almeida, “Model assisted probability of detection applied to guided wave imaging for structural health monitoring,” in *Proceedings of the 46th Annual Review of Progress in Quantitative Nondestructive Evaluation (QNDE2019)*, (Portland, OR, USA), pp. QNDE2019–1234, NDE Department CEA LIST and SAFRAN Tech, July 14-19 2019.

[160] K. Masamura and Y. Nagahama, "Manufacturing processes and products of steel pipes and tubes in JFE steel," Tech. Rep. 7, JFE Steel, Japan, January 2006.

[161] Y. Gulyayev, I. Mamuzić, Y. Shyfrin, M. Buršak, and D. Garmashev, "Perfection of processes of seamless steel tubes production," *Metalurgija*, vol. 50, no. 4, pp. 285–288, 2011.

[162] A. Yamane, K. Yamane, and H. Shitamoto, "Development of numerical analysis on seamless tube and pipe process," Tech. Rep. 107, Nippon Steel & Sumitomo Metal, Japan, February 2015. UDC 669.14-462.3:681.3.

[163] M. S. Randhawa and C. Shah, "Comparison of hot extrusion and hot piercing processes for manufacturing stainless steel hot finished pipes/tubes," *Advanced Materials Research*, vol. 794, pp. 174–185, 2013.

[164] Y. Yoshimura, S. Sasaki, T. Katsumura, and M. Miyake, "Development of dimensional control technology for seamless steel pipe rolling by controlling circumference length in sizing mill," in *International Conference on the Technology of Plasticity*, pp. 173–183, Springer, 2023.

[165] A. Yamane, T. Egoshi, and K. Sasaki, "Wall thickness deviation control of Mannesmann mandrel mill," Technical Report 111, Nippon Steel & Sumitomo Metal, March 2016. UDC 621.774.3.

[166] W. Guo, R. Chen, and J. Jin, "Online eccentricity monitoring of seamless tubes in cross-roll piercing mill," *Journal of Manufacturing Science and Engineering*, vol. 137, no. 2, p. 021007, 2015.

[167] Z. Li, R. Zhang, D. Chen, Q. Xie, J. Kang, G. Yuan, and G. Wang, "Quenching stress of hot-rolled seamless steel tubes under different cool-

ing intensities based on simulation," *Metals*, vol. 12, no. 8, p. 1363, 2022.

[168] B. Harrison, L. Yuan, and S. Kyriakides, "Measurement of lined pipe liner imperfections and the effect on wrinkling and collapse under bending," in *Proceedings of the ASME 2016 35th International Conference on Ocean, Offshore and Arctic Engineering (OMAE2016)*, no. OMAE2016-54539 in OMAE2016, (Busan, South Korea), ASME, American Society of Mechanical Engineers (ASME), June 2016.

[169] D. Lévesque, S. Kruger, G. Lamouche, R. Kolarik Ii, G. Jeskey, M. Choquet, and J.-P. Monchalin, "Thickness and grain size monitoring in seamless tube-making process using laser ultrasonics," *NDT & E International*, vol. 39, no. 8, pp. 622–626, 2006.

[170] A. Volker, "Guided wave tomography in anisotropic media using recursive extrapolation operators," in *AIP Conference Proceedings*, vol. 1949, AIP Publishing, 2018.

[171] M. Klein, "Measuring wall thickness in seamless tube, cast-iron pipe." `https://www.thefabricator.com/tubepipejournal/article/tubepipeproduction/measuring-wall-thickness-in-seamless-tube-cast-iron-pipe`, March 2005. Accessed: 26/05/2024.

[172] J. A. Ogilvy, "Computer simulation of acoustic wave scattering from rough surfaces," *Journal of Physics D: Applied Physics*, vol. 21, no. 2, p. 260, 1988.

[173] F. Shi, W. Choi, M. J. Lowe, E. Skelton, and R. V. Craster, "The validity of kirchhoff theory for scattering of elastic waves from rough surfaces," *Proceedings of the Royal Society A: Mathematical, Physical and Engineering Sciences*, vol. 471, no. 2178, p. 20140977, 2015.

[174] ASTM International, "A106/A106M standard specification for seamless carbon steel pipe for high-temperature service," Tech. Rep. ASTM A106/A106M-19a, ASTM International, West Conshohocken, PA, 2019.

[175] American Petroleum Institute, "API specification 5l, 46th edition: Line pipe," tech. rep., American Petroleum Institute, Washington, D.C., 2018.

[176] J. Dobson and P. Cawley, "The scattering of torsional guided waves from gaussian rough surfaces in pipework," *The Journal of the Acoustical Society of America*, vol. 141, no. 3, pp. 1852–1861, 2017.

[177] J. Parra-Raad, P. Khalili, and F. Cegla, "Shear waves with orthogonal polarisations for thickness measurement and crack detection using emats," *NDT & E International*, vol. 111, p. 102212, 2020.

[178] R. Jarvis, *Current deflection NDE for pipe inspection and monitoring.* PhD thesis, Imperial College London, 2018.

[179] G. Sarris, S. G. Haslinger, P. Huthwaite, P. B. Nagy, and M. J. Lowe, "Attenuation of rayleigh waves due to three-dimensional surface roughness: A comprehensive numerical evaluation," *The Journal of the Acoustical Society of America*, vol. 154, no. 2, pp. 808–818, 2023.

[180] L. Sun, Y. Li, and S. Jin, "Study on guided ultrasonic waves propagating along pipes with fluid loading," in *2006 6th World Congress on Intelligent Control and Automation*, vol. 1, pp. 5037–5041, IEEE, 2006.

[181] W.-B. Na and T. Kundu, "Underwater pipeline inspection using guided waves," *J. Pressure Vessel Technol.*, vol. 124, no. 2, pp. 196–200, 2002.

[182] Y. Simillides, P. Huthwaite, M. K. Kalkowski, and M. J. Lowe, "A displacement-based finite element formulation for solving elastic wave

problems in coupled fluid-solid media on a gpu," *Computers & Structures*, vol. 299, p. 107369, 2024.

[183] H. Sato and H. Ogiso, "Analytical method for guided waves propagating in a fluid-filled pipe with attenuation," *Japanese Journal of Applied Physics*, vol. 52, no. 7S, p. 07HC07, 2013.

[184] F. Shi, M. Lowe, E. Skelton, and R. Craster, "A time-domain finite element boundary integral approach for elastic wave scattering," *Computational Mechanics*, vol. 61, pp. 471–483, 2018.

[185] L. W. Schmerr, *Fundamentals of ultrasonic nondestructive evaluation*, vol. 122. Springer, 2016.

[186] J. Dobson and P. Cawley, "Independent component analysis for improved defect detection in guided wave monitoring," *Proceedings of the IEEE*, vol. 104, no. 8, pp. 1620–1631, 2015.